

Programmable Quantum Simulations of Spin Systems with Trapped Ions

C. Monroe^{*1}, W. C. Campbell², L.-M. Duan³, Z.-X. Gong⁴, A. V. Gorshkov¹, P. Hess⁵, R. Islam⁶, K. Kim³, G. Pagano⁷, P. Richerme⁸, C. Senko⁶, and N. Y. Yao⁹

¹*Joint Quantum Institute and Joint Center on Quantum Information and Computer Science, University of Maryland Department of Physics and National Institute of Standards and Technology, College Park, MD 20742*

²*Department of Physics and Astronomy, University of California, Los Angeles, CA 90095*

³*Center for Quantum Information, Institute for Interdisciplinary Information Sciences, Tsinghua University, Beijing 100084 China*

⁴*Department of Physics, Colorado School of Mines, Golden, CO 80401*

⁵*Department of Physics, Middlebury College, Middlebury, VT 05753*

⁶*Institute for Quantum Computing and Department of Physics and Astronomy, University of Waterloo, Waterloo, Ontario N2L 3G1 Canada*

⁷*Department of Physics and Astronomy, Rice University, Houston, TX 77005*

⁸*Department of Physics, Indiana University, Bloomington, IN 47405 and*

⁹*Department of Physics, University of California, Berkeley CA 94720*

Laser-cooled and trapped atomic ions form an ideal standard for the simulation of interacting quantum spin models. Effective spins are represented by appropriate internal energy levels within each ion, and the spins can be measured with near-perfect efficiency using state-dependent fluorescence techniques. By applying optical fields that exert optical dipole forces on the ions, their Coulomb interaction can be modulated in ways that give rise to long-range and tunable spin-spin interactions that can be reconfigured by shaping the spectrum and pattern of the laser fields. Here we review the theoretical mapping of atomic ions to interacting spin systems, the experimental preparation of complex equilibrium states, and the study of dynamical processes of this many-body interacting quantum system. The use of such quantum simulators for studying spin models may inform our understanding of exotic quantum materials and shed light on interacting quantum systems that cannot be modeled with conventional computers.

* to whom correspondence should be addressed: monroe@umd.edu

PACS numbers: 81.05.Uw,68.37.-d,73.20-r

CONTENTS

I. Introduction	2
A. Atomic Ion Spins	2
B. Coulomb-Collective Motion of Trapped Ion Crystals	3
C. Programmable Magnetic Fields and Interactions between Trapped Ion Spins	5
1. Effective magnetic field	6
2. Effective Ising interactions	6
II. Spin Hamiltonian Benchmarking and Many-Body Spectroscopy	8
A. Sources of Error	9
B. Benchmarking Ising couplings	10
III. Equilibrium studies	11
A. Adiabatic Ground State Preparation	12
B. Experimental Progress in Adiabatic Quantum Simulation	15
1. Transverse Ising model with a small number of spins	15
2. Onset of quantum many-body effects with increasing system size	17
3. Optimizing adiabatic ramps	17
4. Classical Ising model	20
5. Spin-1 simulations	23
IV. Nonequilibrium Phases of Matter and Dynamics	25
A. Information Propagation	25
B. Many-body Localization	27
C. Prethermalization	30
D. Stroboscopic Dynamics and Floquet Phases of Matter	32
E. Dynamical Phase Transitions	35
V. Outlook	37
VI. Acknowledgments	37
References	37

I. INTRODUCTION

Interacting quantum systems cannot generally be efficiently simulated using classical computational techniques, due to the exponential scaling of the information encoded in a quantum state with the size of the system. Accurate modeling of quantum phenomena such as the magnetism of interacting spins, material superconductivity, electronic structure and molecules and their chemistry, Fermi-Hubbard models of electron transport in solids, and interactions within atomic nuclei, are all beyond the reach of classical computation even for just small numbers of interacting degrees of freedom. A quantum simulator exploits the controlled manipulation of a standard quantum system in order to mimic the properties or evolution of a different—perhaps intractable—quantum system [1, 2]. A quantum simulator is a restricted quantum computer [3, 4], with operations that may not be universal but instead be tailored to a particular quantum physical model under study. While useful general purpose and universal quantum computers are still a future prospect, special purpose quantum simulations have already been demonstrated and may in fact become the first useful application of quantum computers.

The equivalence of quantum bits (qubits) and their quantum gates to effective spin-1/2 systems and their interactions has guided one of the most important classes of quantum simulations: interacting spin systems and quantum magnetism. The most advanced physical system for quantum bits or effective spins is a collection of trapped atomic ions [5–7]. This is evidenced by the number of controlled and interacting qubits, the quality of quantum gates and interactions, and the fidelity of initialization/measurement fidelities. Trapped atomic ions, held in a vacuum chamber and confined away from surfaces or solids by electromagnetic fields, laser cooled to be nearly at rest and “wired” together with external laser or microwave fields, offer a very clean quantum system to perform quantum simulations [8–11].

This review assesses recent progress in the quantum simulation of magnetism using trapped atomic ion crystals. Following an introduction of the mapping of spins to atomic ions, we first cover experimental results on the simulation of magnetic ordering, equilibrium states, and phase transitions in quantum magnetic systems. Then we move to dynamical studies of quantum magnetism, touching on general issues of information and entanglement, quantum thermalization, inhibitors to thermalization such as many-body localization and prethermalization, “time crystals” and dynamical phase transitions. We conclude with speculations on how these types of systems may scale in the future and perhaps guide the development of real magnetic material function or more general quantum simulations as special cases of quantum computations.

We note that there are many examples of quantum simulators that translate quantum physics models to effective magnetic spin models and have been implemented in trapped atomic ion systems. This include simulations of interacting Fermionic systems [12–14], variational quantum eigensolvers for molecular and material structure [15–17], quantum approximate optimization algorithms (QAOA) [18], and lattice gauge theories [19–21] such as quantum chromodynamics [22, 23]. Such higher-level simulations transform the operators of interest to spin operators through transformations such as Jordan-Wigner [24] or Bravyi-Kitaev [12], and in these cases the spin system is considered the “back end” of the simulation. This review will not cover recent progress in these higher-level cases, as our aim is to exclusively cover the field of spin simulations. However, the progress and techniques reviewed here are expected to be of great interest to the implementation of the above higher-level simulations.

A. Atomic Ion Spins

We represent a collection of spins by a crystal of electromagnetically trapped atomic ions, with two electronic energy levels within each ion behaving as an effective spin-1/2 particle. The particular choice of electronic levels depends on the atomic element and also the desired type of control fields used to manipulate and measure the spin state. The most important features of these spin states for executing quantum simulations are (a) the spin levels are long-lived and exhibit excellent coherence properties, (b) the spin states have appropriate strong optical transitions to auxiliary excited states, allowing for qubit initialization through optical pumping and qubit detection through fluorescence detection, and (c) the spins interact through a coherent coupling that can be externally controlled and gated. This restricts the atomic species to a handful elements and spin states that are either $S_{1/2}$ hyperfine or Zeeman ground states of single outer-electron atoms (e.g., Be^+ , Mg^+ , Ca^+ , Sr^+ , Ba^+ , Cd^+ , Zn^+ , Hg^+ , Yb^+) with radiofrequency/microwave frequency splittings or metastable electronic excited states of single or dual outer-electron atoms (e.g., Ca^+ , Sr^+ , Ba^+ , Yb^+ , B^+ , Al^+ , Ga^+ , In^+ , Tl^+ , Lu^+) with optical frequency splittings.

In any of these systems, we label the two relevant spin states as $|\downarrow\rangle \equiv |\downarrow_z\rangle$ and $|\uparrow\rangle \equiv |\uparrow_z\rangle$, eigenstates of the Pauli operator σ_z separated by energy $\hbar\omega_0$. In the transverse bases of the Bloch sphere, we define by convention the eigenstates of σ_x as $|\downarrow_x\rangle \equiv |\downarrow\rangle + |\uparrow\rangle$ and $|\uparrow_x\rangle \equiv |\downarrow\rangle - |\uparrow\rangle$, and the eigenstates of σ_y as $|\downarrow_y\rangle \equiv |\downarrow\rangle + i|\uparrow\rangle$ and $|\uparrow_y\rangle \equiv |\downarrow\rangle - i|\uparrow\rangle$.

A typical quantum simulation in the ion trap system is comprised of three sequential steps: initialization, interaction, and measurement, as depicted in Fig. 1. The spins are initialized through an optical pumping process that prepares each spin in a nearly pure quantum state [25]. By applying resonant laser radiation that couples the spin states to appropriate short-lived excited states, each spin can be initialized with $> 99.9\%$ state purity in a few microseconds. This relies on appropriate selection rules for the excited states and also the frequency splitting of the spin states themselves (Fig. 1a). Laser cooling can prepare the

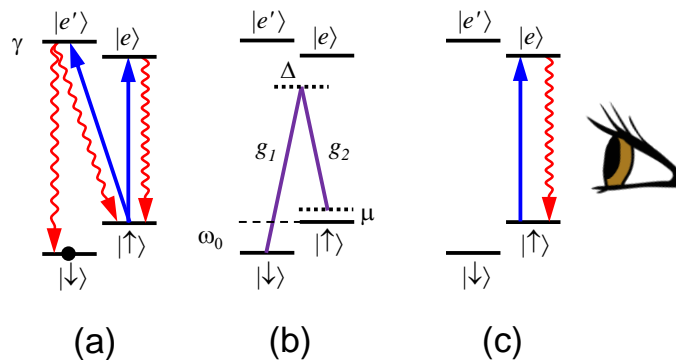


FIG. 1. Reduced energy level diagram of a single atomic ion. Effective spin-1/2 systems are encoded within each atomic ion as appropriate stable electronic energy levels $|\downarrow\rangle$ and $|\uparrow\rangle$. A typical quantum simulation is comprised of three steps: **(a)** Resonant radiation (blue lines) connects one of the two spin states to a pair of excited state levels (linewidth γ) and optically pumps each spin to the $|\downarrow\rangle$ state through spontaneous emission (wavy dotted lines). Here we assume that the excited state $|e\rangle$ couples only to $|\uparrow\rangle$ while the other excited state $|e'\rangle$ couples to both spin states. (There are other sets of selection rules are also possible.) **(b)** In the case of ground-state (e.g., Zeeman or hyperfine) defined spins separated by frequency ω_0 , two tones of off-resonant radiation (purple lines) can drive stimulated Raman transitions between the spin states. The two beams have resonant Rabi frequencies $g_{1,2}$ connecting respective spin states to excited states and are detuned by $\Delta \gg \gamma$, and have a difference frequency (beatnote) detuned from the spin resonance by μ . This coherently couples the spin states to create superpositions ($\mu = 0$) and for non-copropagating beams also couples to the motion of the ion crystal ($\mu \neq 0$). These processes can also be driven directly by radiofrequency or microwave signals, or for optical spin states, a single laser tone. **(c)** Resonant radiation drives the $|\uparrow\rangle \leftrightarrow |e\rangle$ cycling transition, causes the $|\uparrow\rangle$ state to fluoresce strongly (wavy dotted lines), while the $|\downarrow\rangle$ state is far from resonance and therefore dark. This allows the near-perfect detection of the spin state by the collection of this state-dependent fluorescence.

motional states of the ions to near the ground state of harmonic motion [26], which is important for the control of the spin-spin interactions as detailed below.

Each spin can be coherently manipulated by driving the atomic ions with external fields that couple the spin states. This can be accomplished by resonantly driving the spin levels with appropriate radiation at frequency ω_0 , or in Fig. 1b, this is depicted as a two-field Raman process, with a beatnote of two optical fields at ω_0 driving the spin (this will be assumed throughout unless otherwise indicated). This coherent coupling can also drive motional sideband transitions [26] that couple the spin to the motion of the ion. For multiple ions, this can be used to generate spin-spin couplings mediated by the Coulomb interaction, described in more detail below [5]. These external fields provide exquisite control over the effective spin-spin interaction, with the ability to gate the interaction, program different forms of the interaction strength and range, and even reconfigure the interaction graph topology.

At the end of the quantum simulation, the spins are measured by applying resonant laser radiation that couples one of the two spin states to a short-lived excited state through a cycling transition and detecting the resulting fluorescence [27–29]. This is depicted in Fig. 1c, where we take the $|\uparrow\rangle$ or “bright” state as fluorescing and the $|\downarrow\rangle$ or “dark” state as not fluorescing. Even though the photon collection efficiency may be small (typically less than 1%), the effective spin detection efficiency can be well above 99% owing to the low probability of leaving the fluorescence cycle or having the other (dark) state entering the cycle [30–34]. In order to detect the spins in other bases in the Bloch sphere (σ_x or σ_y), previous to fluorescence measurement the spins are coherently rotated by polar angle $\pi/2$ along the y or x axis of the Bloch sphere, respectively.

B. Coulomb-Collective Motion of Trapped Ion Crystals

Atomic ions can be confined in free space with electromagnetic fields supplied by nearby electrodes. Two types of ion traps are used for quantum simulation experiments: the linear radiofrequency (rf) trap and the Penning trap. The linear rf trap (Fig 2a) [35] juxtaposes a static axial confining potential with a two-dimensional rf quadrupole potential that provides a time-averaged or ponderomotive transverse confinement potential [36, 37]. The trap anisotropy is typically adjusted so that the static axial confinement is much weaker than the transverse confinement so that laser-cooled ions reside on the axis of the trap where the rf fields are null, resulting in a one-dimensional chain of trapped ion spins. A harmonic axial confinement potential results in an anisotropic linear ion spacing [38], but they can be made nearly equidistant by applying an appropriate quartic axial confining potential [39]. The Penning trap (Fig 2b) juxtaposes a uniform axial magnetic field with a static axial confining potential, and the transverse confinement is provided by the $\mathbf{E} \times \mathbf{B}$ drift toward the axis [40, 41]. Here, the trap anisotropy is typically adjusted so

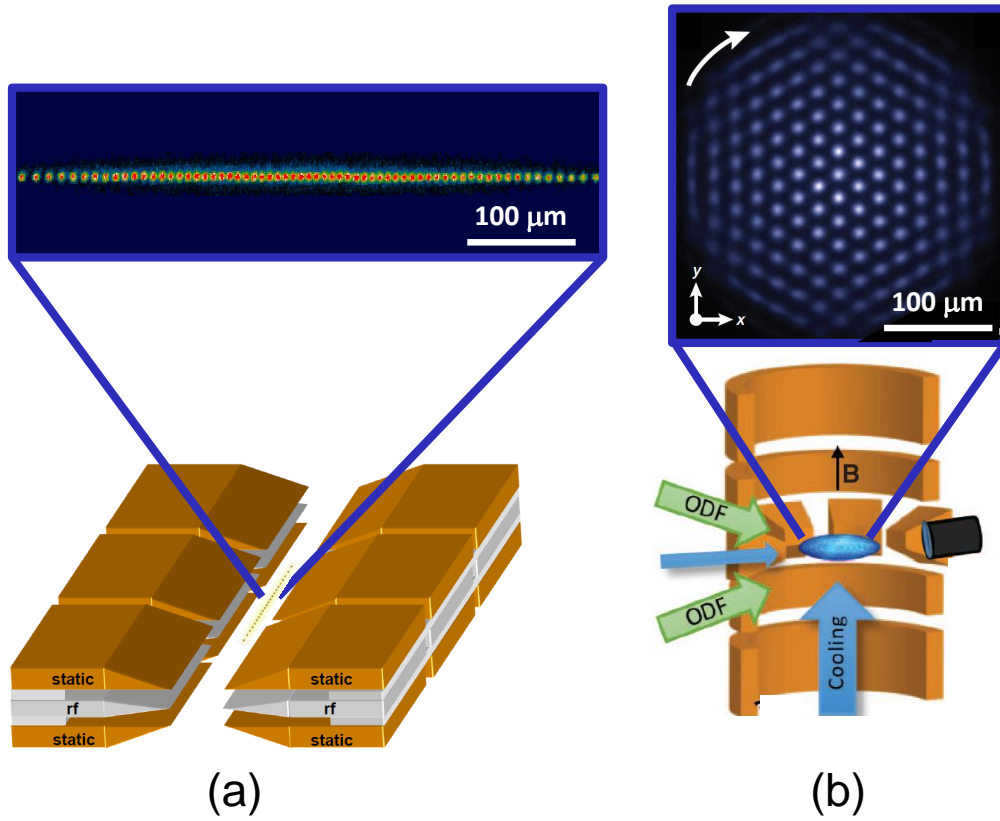


FIG. 2. (a) Radiofrequency (rf) linear trap used to prepare a 1D crystal of atomic ions. The geometry in this trap has three layers of electrodes, with the central layer (gray) carrying rf potentials to generate a 2D quadrupole along the axis of the trap. Static electrodes (gold) confine the ions along the axis of the trap. For sufficiently strong transverse confinement, the ions form a linear crystal along, with an image of 64 ions shown above with characteristic spacing $5 \mu\text{m}$ for $^{171}\text{Yb}^+$ ions. From 42. (b) Penning trap used to prepare a 2D crystal of atomic ions. The gold electrodes provide a static quadrupole field that confines the ions vertically, and the vertical magnetic field stabilizes their orbits in the transverse plane. For sufficiently strong axial confinement, the lowest energy configuration of the ions is a single plane triangular lattice that undergoes rigid body rotation, with an image of ~ 200 $^9\text{Be}^+$ ions shown above with a characteristic spacing of $20 \mu\text{m}$. From 41.

that the ions form a two-dimensional crystal perpendicular to and rotating about the axis. Both traps can be modified to support other types of crystals in any number of spatial dimensions, but the quantum simulations reviewed here are either 1-D chains in rf traps or 2-D crystals in Penning traps. (It should be noted that the dimensionality of the spin-spin interaction graph does not necessarily follow that of the spatial arrangement of spins, as described below.)

Ions are typically loaded into traps by generating neutral atoms of the desired element and ionizing the atoms once in the trapping volume via electron bombardment or photoionization. Ion trap depths are usually much larger than room temperature, so rare collisions with background gas do not necessarily eject the ion from the trap, but they can temporarily break up the crystal and scramble the atomic ions in space. Under typical ultra-high-vacuum conditions, these collisional interruptions occur roughly once per hour per ion [43], but cryogenic vacuum chambers can reduce the collision rate by orders of magnitude, where the trapped ions can be undisturbed for weeks or longer between collisions.

When atomic ions are laser-cooled to near the bottom of the trapping potential, they form a stable crystal, with the Coulomb repulsion balancing the external confinement force. Typical spacings between adjacent ions in trapped ion crystals are $\sim 3 - 20 \mu\text{m}$, depending on the ion mass, number of ions in the crystal, the characteristic dimensions of the electrodes, and the applied potential values. The equilibrium positions of ions in the crystal can be calculated numerically [38, 44]. The motion of the ions away from their equilibrium positions is well-described by harmonic normal modes of oscillation (phonon modes), with frequencies in the range $\omega_m/2\pi \sim 0.1 - 10$ MHz. The thermal motion of laser-cooled ions and also the driven motion by external forces is at the $10 - 100$ nm scale, justifying the harmonic approximation to the phonon modes.

For the systems described here, we consider only the transverse motion along a single dimension labeled X . We write the X -component of position of the i th ion as $\hat{X}_i = \bar{X}_i + \hat{x}_i$, separating the mean (stationary) position \bar{X}_i of the i th ion from the small harmonic oscillations described by the quantum position operator \hat{x}_i . The motion of ions in the crystal is tightly coupled by the Coulomb interaction, so it is natural to express the position operator in terms of the $m = 1 \dots N$ normal (phonon) modes,

$\hat{x}_i = \sum_{m=1}^N b_{i,m} \xi_m$, where $b_{i,m}$ is the normal mode transformation matrix, normalized to $\sum_i |b_{i,m}|^2 = \sum_m |b_{i,m}|^2 = 1$. Each phonon mode ξ_m oscillates at frequency ω_m , and can be described as a quantum harmonic oscillator with the usual raising and lowering operators a_m^\dagger and a_m , having zero-point spatial spread $\xi_m^{(0)} = \sqrt{\hbar/2M\omega_m}$, where M is the mass of a single ion. In the interaction frame for each phonon mode, the position of the i th ion is thus written as

$$\hat{X}_i = \bar{X}_i + \sum_{m=1}^N b_{i,m} \xi_m^{(0)} (a_m^\dagger e^{i\omega_m t} + a_m e^{-i\omega_m t}). \quad (1)$$

Calculations of the phonon mode frequencies and transformation matrix rely on numerical calculations of the ion equilibrium positions and then solutions to the normal mode eigenvalue problem [38, 44, 45]. In general, the structure of transverse phonon modes of the ion crystal has the center-of-mass mode as its highest frequency, with the lowest frequency corresponding to zig-zag motion where adjacent ions move in opposite directions, as shown in Fig. 3 for a linear chain of 32 ions and a 2D crystal of about 345 ions. The bandwidth of the modes can be controlled by tuning the spatial anisotropy of the trap.

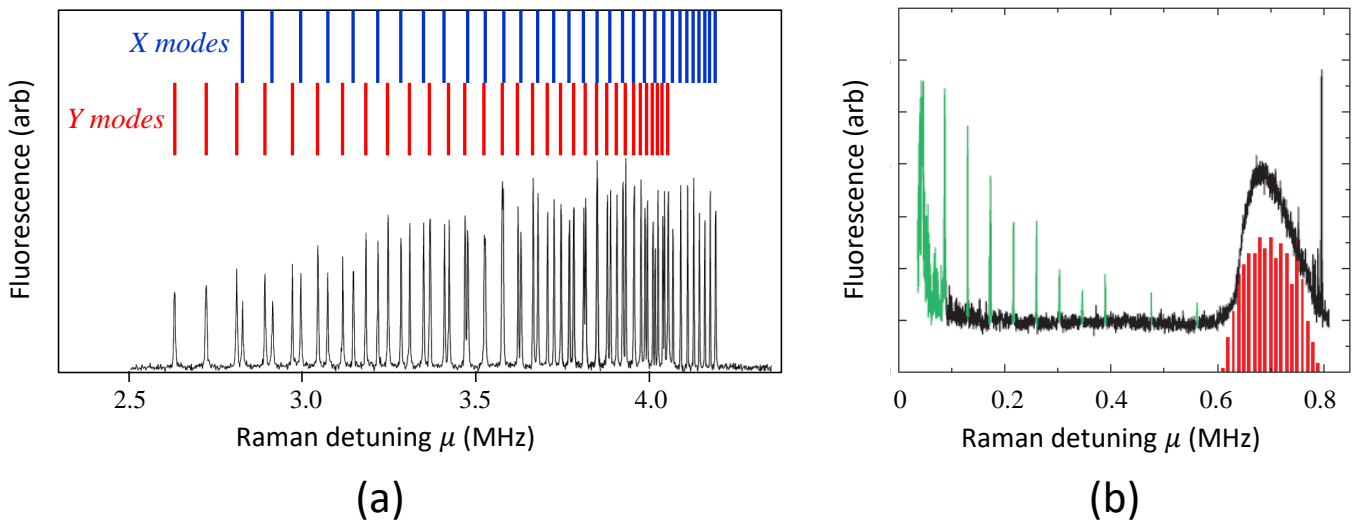


FIG. 3. Raman upper sideband spectrum of the transverse motion of trapped atomic ion crystals. The spectrum is measured by preparing all of the ions in state $|\downarrow\rangle$ and driving them with global Raman laser beams with beatnote detuning μ from the spin-flip resonance and measuring the total fluorescence of the chain, which responds when the beatnote matches a sideband resonance. (a) 32 trapped $^{171}\text{Yb}^+$ atomic ions in a linear chain (see Fig. 2a). Here, the Raman excitation is sensitive to both X and Y principal axes of transverse motion, and the theoretical position of both sets of 32 modes are indicated at top in blue and red. The highest frequency sidebands correspond to center-of-mass modes at 4.19 MHz for the X direction and 4.05 MHz for the Y direction. (Unpublished data from the University of Maryland.) (b) Measured (black) and calculated (red) sideband spectrum for 2D crystal of 345 ± 25 $^9\text{Be}^+$ ions in a Penning trap (see Fig. 2b) with rotation frequency 43.2 kHz. As in the linear chain, the highest frequency sideband corresponds to center-of-mass motion. Features at the rotation frequency and its harmonics (green) are due to residual couplings to in-plane degrees of freedom from imperfect beam alignment. Adapted from 44.

C. Programmable Magnetic Fields and Interactions between Trapped Ion Spins

Effective magnetic fields and spin-spin interactions can be realized by applying external microwave or optical fields to the ions. We consider the case of optical fields, since they can be used to not only provide effective site-dependent magnetic fields for the spins through tight focusing, but the strong dipole forces from laser beams can also drive effective Ising interactions between the spins [46–49]. Such forces can be applied to pairs of ions in order to execute entangling quantum gates that are applicable to quantum computing [5]. When such forces are instead applied more globally, the resulting interaction network allows the quantum simulation of a wide variety of spin models such as the Ising and Heisenberg spin chains [8–10].

Following Fig. 1b and assuming the spins are encoded in stable (e.g., Zeeman or hyperfine) levels, the ion crystal is addressed with two laser beams detuned from the excited states by much more than the excited state radiative linewidth ($\Delta \gg \gamma$). By adiabatically eliminating the excited states, this drives coherent Raman transitions between the spin states. Alternatively, optically-defined spin levels can be coupled with a single laser beam [32], but this is much more difficult technically, as the spins can acquire an optical phase that requires extreme positional stability of the optical setup. With Raman beams, the relevant

phase is that of the optical beat note between the beams, which is typically in the microwave domain and hence easy to control and stabilize.

The two Raman beams are generally non-copropagating with their wavevector difference δk pointing along the X-axis of motion and a beatnote detuned by frequency μ from spin resonance with beatnote phase ϕ_L . In this case, the atom-light interaction Hamiltonian takes the form ($\hbar = 1$)

$$H = \frac{1}{2} \sum_i \left[\Omega_i \left(\sigma_+^i e^{i(\delta k \hat{X}_i - \mu t - \phi_L)} + \sigma_-^i e^{-i(\delta k \hat{X}_i - \mu t - \phi_L)} \right) + \delta_i \sigma_z^i \right], \quad (2)$$

where the resonant Raman Rabi frequency on the i th ion is $\Omega_i = g_1^i g_2^i / 2\Delta$. Here $g_{1,2}^i$ are the direct (single field) Rabi frequencies of the associated transitions through the excited states (see Fig. 1b), proportional to the respective applied optical electric fields. Below, we will assume that the ions are confined to the ‘‘Lamb-Dicke limit’’ [26, 43] where the excursion of ion motion is much less than the associated wavelength of radiation driving transitions: $\delta k \langle \hat{x}_i^2 \rangle^{1/2} \ll 1$. This is typically a good assumption for trapped ions laser-cooled to near their ground state. The last term in Eq. (2) is a Stark shift of the i th spin by amount δ_i and arises when the Raman laser beat note is tuned away from any resonance. The magnitude of this shift depends greatly on the atomic energy level structure [50, 51].

1. Effective magnetic field

For a resonant ‘‘carrier’’ interaction ($\mu = \delta = \delta k = 0$) and under the rotating wave approximation ($\omega_m \gg \Omega_i$), the time dependence of \hat{X} averages to zero and the Hamiltonian of Eq. (2) is just

$$H_{B_\phi} = \frac{1}{2} \sum_i \Omega_i \sigma_\phi^i, \quad (3)$$

where the transverse field spin operator is

$$\sigma_\phi^i = \sigma_+^i e^{i\phi} + \sigma_-^i e^{-i\phi} = \sigma_x^i \cos \phi - \sigma_y^i \sin \phi. \quad (4)$$

This operation describes the precession of the spin about an effective magnetic field in the xy plane of the Bloch sphere with Rabi frequency Ω_i , at an angle $\phi = \delta k \bar{X}_i - \phi_L$ that can be precisely controlled through the phase ϕ_L . In cases where $\delta k \neq 0$, the Rabi frequency acquires a dependence on the motion of the ions through Debye-Waller factors [43], but these are very small in the Lamb-Dicke limit [26].

Tuning the Raman laser beat note away from the carrier ($\mu \neq 0$) generally results in an AC Stark shift of the spin levels, given by the last term in Eq. (2) [50, 51]. When each spin is exposed to a unique intensity of light and/or detuning, parametrized by δ_i , this gives rise to a site-dependent effective axial magnetic field.

2. Effective Ising interactions

When the frequency μ tuned to the neighborhood of the phonon modes ω_m , the spins are coupled to the ion motion through the spatial variation of the phase factor in Eq. (2). This will generate an effective spin-spin interaction between the ions mediated by the collective transverse vibrations of the chain. For most simulation experiments, the transverse modes of motion are used to mediate the spin-spin interaction because their frequencies are tightly packed and all contribute to the effective spin Hamiltonian, allowing control over the form and range of the interaction, described further below. Transverse modes also oscillate at higher frequencies, leading to better cooling and less sensitivity to external heating and noise [52].

In general, when noncopropagating laser beams have bichromatic beatnotes at frequencies $\omega_0 \pm \mu$ symmetrically detuned from the carrier with respective beat note phases ϕ_{L+} and ϕ_{L-} , both upper and lower motion-induced sidebands [26] of the normal modes of motion are driven in the ion crystal, giving rise to a spin-dependent force at frequency μ [8, 47]. When the bichromatic beat notes are asymmetrically detuned from the carrier by $\omega_0 + \mu_+$ and $\omega_0 - \mu_-$, the effective spin-dependent force occurs at frequency $\mu = (\mu_+ + \mu_-)/2$ and the asymmetry provides an effective uniform axial magnetic field in Eq. (2) with $\delta_i = \mu_+ - \mu_-$.

Under the rotating wave approximation with symmetric detuning ($\omega_0 \gg \mu = \mu_+ = \mu_- \gg \Omega_i$) and within the Lamb-Dicke limit, the resulting interaction Hamiltonian is [52]

$$H(t) = \frac{1}{2} \sum_{i,m} \eta_{i,m} \Omega_i \sigma_\theta^i \left[a_m^\dagger e^{i(\mu - \omega_m)t + i\beta} + a_m e^{-i(\mu - \omega_m)t - i\beta} \right]. \quad (5)$$

Here, the transverse spin operator coupled to motion is [53]

$$\sigma_\theta^i = i\sigma_+^i e^{i\theta} - i\sigma_-^i e^{-i\theta} = \sigma_x^i \sin \theta + \sigma_y^i \cos \theta, \quad (6)$$

with spin phase $\theta = \delta k \bar{X}_i - (\phi_{L+} + \phi_{L-})/2$, motional phase $\beta = (\phi_{L+} - \phi_{L-})/2$, and $\eta_{i,m} = b_{i,m} \delta k \xi_m^{(0)}$ is the Lamb-Dicke parameter matrix.

The evolution operator under this Hamiltonian can be written from the Magnus expansion, which terminates after the second term owing to the commutation relation $[a_m, a_n^\dagger] = \delta_{m,n}$, and we find the exact relation [52]

$$U(\tau) = \exp \left[-i \int_0^\tau H(t) dt - \frac{i}{2} \int_0^\tau dt_1 \int_0^{t_1} dt_2 [H(t_1), H(t_2)] \right] \quad (7)$$

$$= \exp \left[\sum_i \hat{D}_i(\tau) \sigma_\theta^i + i \sum_{i,j} \chi_{i,j}(\tau) \sigma_\theta^i \sigma_\theta^j \right]. \quad (8)$$

The first term of Eq. (8) is a spin-phonon coupling with operator $\hat{D}_i(\tau) = \sum_m [\alpha_{i,m}(\tau) a_m^\dagger - \alpha_{i,m}^*(\tau) a_m]$, representing spin-dependent displacements [26] of the m th motional mode through phase space by an amount

$$\alpha_{i,m}(\tau) = \frac{-i\eta_{i,m}\Omega_i}{\mu^2 - \omega_m^2} [\mu - e^{i\omega_m\tau} (\mu \cos \mu\tau - i\omega_m \sin \mu\tau)]. \quad (9)$$

The second term of Eq. (8) is the key result: a spin-spin interaction between ions i and j with coupling strength

$$\chi_{i,j}(\tau) = \Omega_i \Omega_j \sum_m \frac{\eta_{i,m} \eta_{j,m}}{\mu^2 - \omega_m^2} \left[\frac{\mu \sin(\mu - \omega_m)\tau}{\mu - \omega_m} - \frac{\mu \sin(\mu + \omega_m)\tau}{\mu + \omega_m} + \frac{\omega_m \sin 2\mu\tau}{2\mu} - \omega_m \tau \right]. \quad (10)$$

There are two regimes where the collective modes of motion contribute to the spin-spin coupling, taking evolution time τ to be much longer than the ion normal mode oscillation periods ($\omega_m \tau \gg 1$). In the “resonant” regime [48, 49, 54], the optical beatnote detuning μ is close to one or more normal modes and the spins become entangled with the motion through the spin-dependent displacements. However, at certain times of the evolution $\alpha_{i,m}(\tau) \approx 0$ for all modes m and the motion nearly decouples from the spin states, which is useful for applying synchronous entangling quantum logic gates between the spins.

In the “dispersive” regime [8, 47], the optical beatnote frequency is far from each normal mode compared to that mode’s sideband Rabi frequency ($|\mu - \omega_m| \gg \eta_{i,m} \Omega_i$). In this case, the phonons are only virtually excited as the displacements become negligible ($|\alpha_{i,m}| \ll 1$), and the result is a fully-connected Ising Hamiltonian from the last (secular) term of Eq. (10):

$$H_{J_\theta} = \sum_{i,j} J_{i,j} \sigma_\theta^i \sigma_\theta^j, \quad (11)$$

where the Ising matrix is given by

$$J_{i,j} = \Omega_i \Omega_j \omega_R \sum_m \frac{b_{i,m} b_{j,m}}{\mu^2 - \omega_m^2}, \quad (12)$$

and $\omega_R = \hbar \delta k^2 / 2M$ is the recoil frequency associated with the transfer of momentum $\hbar \delta k$ to a single ion.

Substituting the exact values for the normal mode matrix $b_{i,m}$ and assuming that the optical force is detuned at frequencies higher than all phonon modes ($\mu > \omega_m$), we find that for a uniform Rabi frequency over the ions $\Omega_i = \Omega$, the Ising matrix is well approximated by a long-range antiferromagnetic (AFM) coupling that fall off as an inverse power law with distance

$$J_{i,j} = \frac{J_0}{|i-j|^\alpha}, \quad (13)$$

with nearest-neighbor Ising coupling J_0 . The exponent α that determines the range of the Ising interaction can be set to $0 < \alpha < 3$ by simply adjusting the laser detuning μ [8, 42]. The true asymptotic long-chain behavior of a trapped ion chain is more subtle [55], but the power law approximation is very good, as shown in Fig. 4, comparing numerically exact couplings with best-fit power laws for various detunings μ in both a linear and 2D crystal.

When the detuning μ is tuned between the modes of motion, many other patterns of the Ising graph can be realized [56, 57]. The spin-spin interaction profile $J_{i,j}$ can in principle be tuned arbitrarily, by manipulating individual spin-phonon couplings.

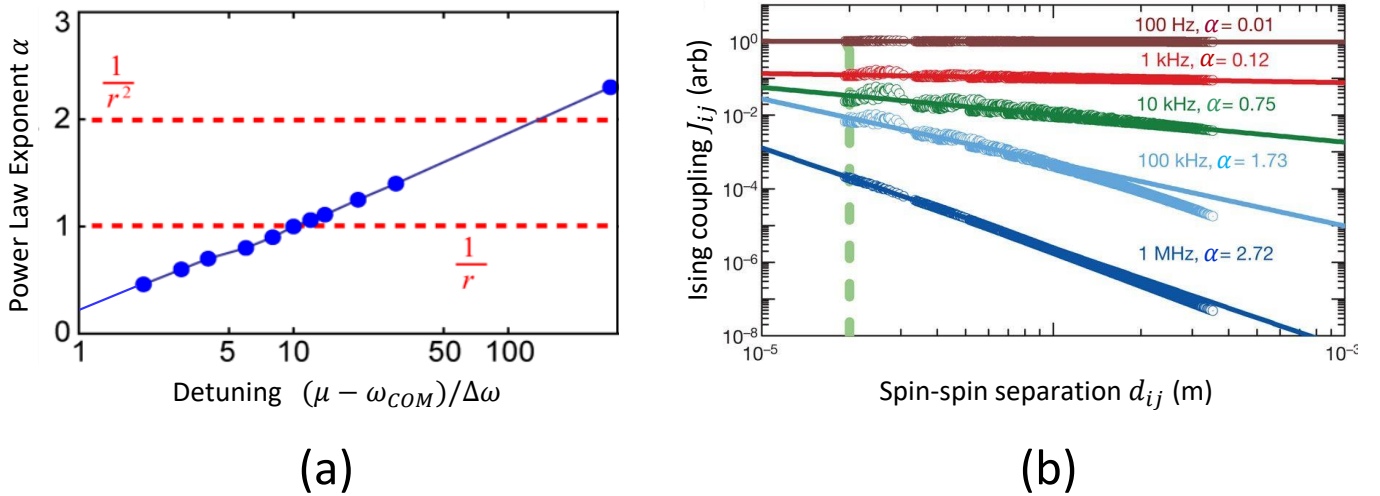


FIG. 4. Inverse power law approximation to Ising couplings. (a) Best fit power law exponent as a function of Raman detuning $\mu - \omega_{COM}$ from center-of-mass mode, scaled to the bandwidth $\Delta\omega$ of transverse modes in a linear chain of 25 ions with harmonic axial confinement. (b) Calculated Ising couplings from Eq. (12) in a 2D crystal of 217 ions versus a sampling of the distance d_{ij} between ion pairs (circles), the lines are best-fit power law exponents α (lines) for various detunings from the center-of-mass mode of 795 kHz. Adapted from 44.

For example, N bichromatic Raman beatnotes at $\omega_0 \pm \mu_n$, with $\mu_n \approx \omega_n$ ($n = 1, 2, \dots, N$) can be used with local intensity control over each ion to create an arbitrary interaction graph:

$$J_{i,j} = \sum_n \Omega_{i,n} \Omega_{j,n} \omega_R \sum_m \frac{b_{i,m} b_{j,m}}{\mu_n^2 - \omega_m^2}. \quad (14)$$

Here, $\Omega_{i,n}$ is the Rabi frequency corresponding to the n^{th} beatnote at i^{th} ion. Note that $J_{i,j}$ is nonlinear in the $\mathcal{O}(N^2)$ experimental control parameters $\Omega_{i,n}$ and μ_n , and hence tuning the quantum simulator requires non-linear optimization methods [56]. Alternative approaches to realize a target interaction graph without tuning the full Rabi frequency matrix, $\Omega_{i,n}$ include modifying a global Mølmer-Sørensen coupling profile (such as Eq.(13)) by local spatial control of spins in hybrid analog-digital ways [58, 59].

Similar to the case for the effective magnetic field of Eq. (3), we find that the Bloch sphere axis of the Ising interaction, given by the angle θ in Eq. (6), can be precisely controlled through the applied phases $\phi_{L\pm}$ of the two optical beatnotes. As a practical consideration, we note that the spin phases ϕ and θ in Eqs. (3) and (11) are sensitive to the applied optical beatnote phases ϕ_L and $\phi_{L\pm}$, thus requiring phase stability of all processes during a single simulation run. For extended simulations in time, alternative “phase insensitive” configurations can be implemented to remove optical phase sensitivity [53].

This review will mainly consider Ising interactions in the slow dispersive regime in order to engineer pure spin Hamiltonians given by Eqs. (3) and (11) that do not directly involve the bosonic phonon operators. An important class of models in quantum magnetism that will appear throughout this review is the transverse field Ising model, which is one of the simplest physical models that admits a quantum phase transition [60], owing to its noncommuting terms:

$$H_{TI} = \sum_{i,j} J_{i,j} \sigma_x^i \sigma_x^j + B_y \sum_i \sigma_y^i. \quad (15)$$

In ion trap systems, this model can be generated with a combination of the effective magnetic field in Eq. 3 and the Ising interactions in Eq. (12).

II. SPIN HAMILTONIAN BENCHMARKING AND MANY-BODY SPECTROSCOPY

A compelling Hamiltonian quantum simulation usually results in some type of nontrivial ground state or dynamics that may elude classical computation. It is therefore important to verify that the desired Hamiltonian is indeed being faithfully run by the quantum simulator [61, 62]. For systems that are small enough and tractable for a direct comparison between the simulator’s results and a theoretical calculation, this will provide some confidence that the proper simulation has been run. But then scaling up the system can introduce additional imperfections that may call into question the accuracy of the applied Hamiltonian.

Two approaches for verifying quantum simulators beyond classically computability are the use of fault-tolerant techniques in the expression of the simulation in terms of discrete error-corrected gates [63, 64], and the comparison of the results of multiple quantum simulators built upon different platforms [65]. Though this list is not comprehensive (see, e.g. [62]), we examine these two approaches briefly below.

Universal Hamiltonian digital quantum simulators (DQS) break up the simulation evolution into a series of time steps, and the error ϵ introduced by this “Trotterization” is bounded and inversely proportional to the number of steps M [66]. This approach was notably employed for the implementation of various Hamiltonians, including many-body magnetic couplings, in a system of trapped ions [67]. Because DQS relies on discrete quantum gate sets, its verification can in principle be accomplished through fault-tolerant error correction on the gates [68]. This increases the number of operations required by a factor of $(1/\epsilon)^{r-1}$ where $r \geq 2$, and the number of operations therefore scales exponentially with rM , bringing the resource cost for DQS to be similar to that of universal quantum computing [69, 70]. Further, simulations with systems that lack universal gate sets or the digital simulation of open systems may render fault-tolerance unavailable in a DQS [71]. Since the cost of introducing currently known methods for fault-tolerance is too high for precision DQS [72], other methods for verifying non-fault-tolerant-DQS are needed.

Another way one might test quantum simulators is to compare the results of two simulations. This could involve comparing the results of simulations performed on different platforms [65], or even comparing the results obtained by using different simulation methods on the same machine. A variant on this second theme is to run a simulation forward and then backward in time [61], which may reveal flaws that are not undone by the time reversal, such as dissipation. An initial experiment demonstrated this time-reversal technique for a trapped ion quantum simulation by adiabatically ramping from an initial state of high magnetization along y , through a phase transition, and then back again [73]. Measurements of the magnetization at all three extrema in this time sequence revealed a revival in the magnetization, achieving an average of $\langle S_y \rangle = 68(4)\%$ of the initial value, in agreement with closed-system numerical integration.

Recently, a variational eigensolver approach has been combined with an ion trap quantum simulator to perform variational quantum simulation (VQS) of the lattice Schwinger model that combines some ways to verify some features of the result [22]. The VQS uses feedback with a classical computer that translates measurement results from the AQS into expectation values of a software Hamiltonian to find energy eigenstates of the underlying Hamiltonian. Since the conversion between the measurement and its interpretation happens in classical software, it provides a way to perform some verification of the resulting states because both the eigenvalues and their variances are accessible. For instance, the VQS demonstrated in [22] measured the expectation value of the simulated Hamiltonian $E = \langle H \rangle$, as well as the expectation value of $(H - E)^2$, which should be zero if the state is an energy eigenstate of H with eigenvalue E . While this does not guarantee that the state found by the VQS is the ground state, this verification can be used to assess the confidence in the state being an eigenstate.

A. Sources of Error

Quantum simulations with trapped ions can be susceptible to unwanted interactions that lead to inaccuracies in the simulation. Many such error sources are common to both simulations and trapped ion quantum computing gates, such as spontaneous emission from the lasers driving spin transitions, and have been examined in detail elsewhere [43, 74]. Further, the simulation protocol itself may have known approximations (such as the Trotterization errors and non-adiabatic evolution) that may be rigorously bounded, though their effects may not be fully understood.

The inclusion of a transverse effective magnetic field to the spin-dependent force of Eq. (5) includes higher order terms beyond the simple transverse Ising model of Eq. (15) [75]. These additional terms can create substantial spin-motion entanglement that can affect measurements in bases other than the Ising direction. For transverse field strengths that exceed the Ising coupling, the system begins to attain the character of an XY model with both $\sigma_x^i \sigma_x^j$ and $\sigma_y^i \sigma_y^j$ couplings, and the strong-field Ising model can break down. The spins in this case do not strictly decouple from the phonons at any point in time, but it has been shown that it can typically be made small for experimentally accessible timescales [76].

Protocols that rely on adiabatically ramping through a small gap can be susceptible to the breakdown of the adiabatic approximation in the region where the gap is small. As we discuss below, for a linear ramp of $B(t)$ through a system energy gap of size Δ , the adiabaticity criterion is approximately $|\dot{B}_y/\Delta^2| \ll 1$. For cases where the gaps are known, the ramp rate can be adaptively matched to the gap to maximize adiabaticity, a technique known as local adiabatic evolution [77]. However, since repeated experiments can be used to gather statistics about the final state, it has been shown that significant non-adiabaticity can be present and still allow the ground state spin configuration to be found due to its statistical prevalence [78].

State preparation and measurement (SPAM) errors, which are to some degree common to simulators and gate-based quantum computers, are another source of error in lattice spin simulators. Given an uncorrelated, single-shot, single ion SPAM fidelity \mathcal{F} , the probability of a single SPAM error is $1 - \mathcal{F}^N$. Here, in cases where it is possible, repeated experiments can again be used to mitigate this error through statistical methods [79]. Cross-talk between neighboring ions can also lead to measurement errors, and the ion positions must be calibrated to define a region of interest on the camera for each ion’s fluorescence detection.

Cross-talk is typically no more than a few percent error.

Decoherence during the simulation can also arise from various sources, such as stray magnetic and electric fields, mode frequency drifts, and spontaneous emission. While these errors have been analyzed in the context of quantum computing (see, e.g. [43], in practice, decoherence can set a time limit for the simulation that may then feed back into, for instance, adiabaticity errors. Since many of these error sources increase with system size, it may be necessary to employ methods of mitigation (for instance, magnetic field shielding [80]).

B. Benchmarking Ising couplings

For the Ising spin models considered in this review, it is crucial to validate the strength of the Ising coupling matrix J_{ij} of Eqs. (11) and (12) and effective magnetic fields in Eq. (3). For small numbers of spins, it is possible to directly extract the Ising couplings and fields by preparing the spins in a σ_z eigenstate and subjecting them to the σ_θ Ising interactions or field terms. The resulting oscillations in population are given by the energies of the occupied states, so performing a Fourier transform on these oscillations to extract their characteristic frequencies gives direct information on the energy differences.

An example of directly-measured Ising oscillations and their resultant Fourier transform are shown in Figs 5a-b for $N = 3$ spins. The extracted interaction strengths are shown in Fig. 5c. This technique is effective in contexts of both continuous [81] and digital [67] simulations of Ising models. A similar method has been used to extract the strengths of a magnetically induced spin-spin couplings [82, 83]. Neither technique scales well to more than a few spins, because of the difficulty of extracting many closely-spaced frequencies in the spin oscillations.

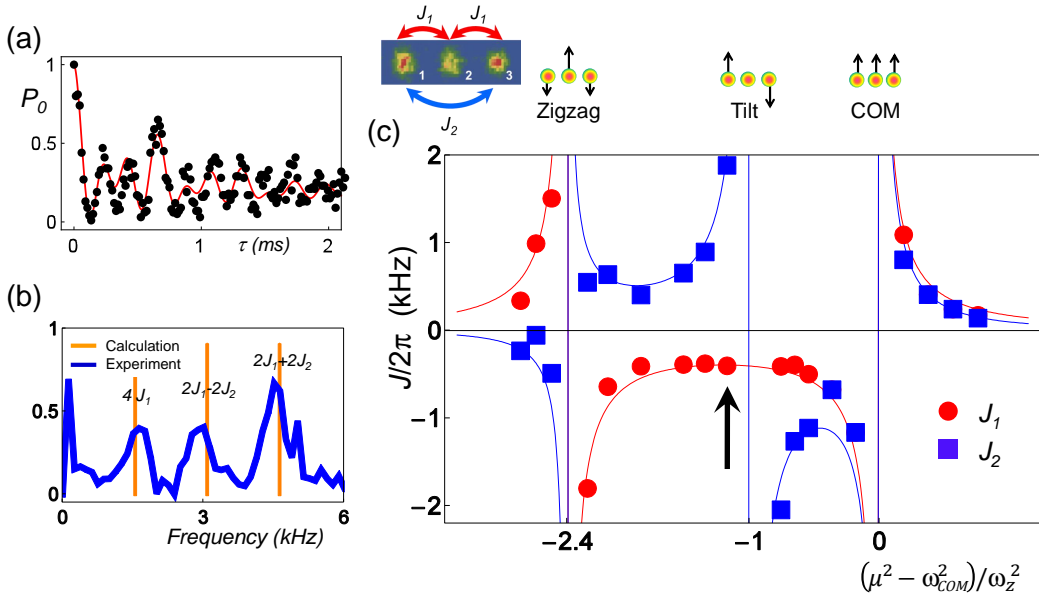


FIG. 5. Direct measurement of Ising nearest-neighbor (NN) J_1 and next-nearest-neighbor (NNN) J_2 interactions for $N = 3$ trapped ion spins. (a) Time evolution of the probability P_0 of state $|\downarrow\downarrow\downarrow\rangle$ with the solid line fit to theory with an empirical exponential decay. (b) The Fourier spectrum of the oscillations in (a) exposing the frequency splittings of the Hamiltonian. (c) Solid curves are expected form of the Ising interactions J_1 and J_2 from Eq. (12) as a function of the beat-note detuning μ scaled so that the center-of-mass (COM), tilt, and zigzag modes of transverse motion occur at $(\mu^2 - \omega_{COM}^2)/\omega_z^2 = 0, -1, \text{ and } -2.4$, respectively. The red circles and blue squares are experimentally measured couplings. The particular measurements in (a) and (b) correspond to the laser beat note detuning μ indicated by the arrow in (c). From 84

Individual Ising couplings within a given spin chain can be measured using an auxiliary state of the ions, even for large numbers of spins. Because the Ising couplings depend on the vibrational mode spectrum, all ions must be physically present in the trap to obtain a meaningful result, but the spectrum of the population oscillations illustrated in Fig. 5 would be difficult to obtain if all spins participate in the many-body dynamics. An alternative approach is to perform a separate measurement for each individual Ising coupling, by “hiding” all ions except the pair of interest into an auxiliary internal state that does not experience the spin-dependent force giving rise to Ising couplings. In this manner, the frequency with which the ions i and j of interest oscillate between $|00\rangle_z$ and $|11\rangle_z$ can be measured to directly obtain the Ising matrix J_{ij} [85].

Other spectroscopic techniques for probing the energy spectrum of the bare Ising Hamiltonian are also possible [86]. For instance, in the transverse Ising model of Eq. (15), modulating the effective field $B_y(t)$ at a frequency commensurate with an energy difference in the full spin Hamiltonian will drive transitions between the two differing states. Specifically, taking $B_y(t) = B_0 + B_p \sin(\omega_{mod}t)$ with $B_p \ll J$, the frequency ω_{mod} at which such transitions occur are directly related to the Ising couplings $J_{i,j}$ [86]. Figure 6 illustrates examples where the Ising matrix is directly measured using this technique to confirm the validity of power-law approximation described in Eq. (13) for a handful of spins. The technique of applying a small oscillating term can be generalized to other cases, for example, measuring the critical gap of the transverse field Ising model, as shown in Figure 6.

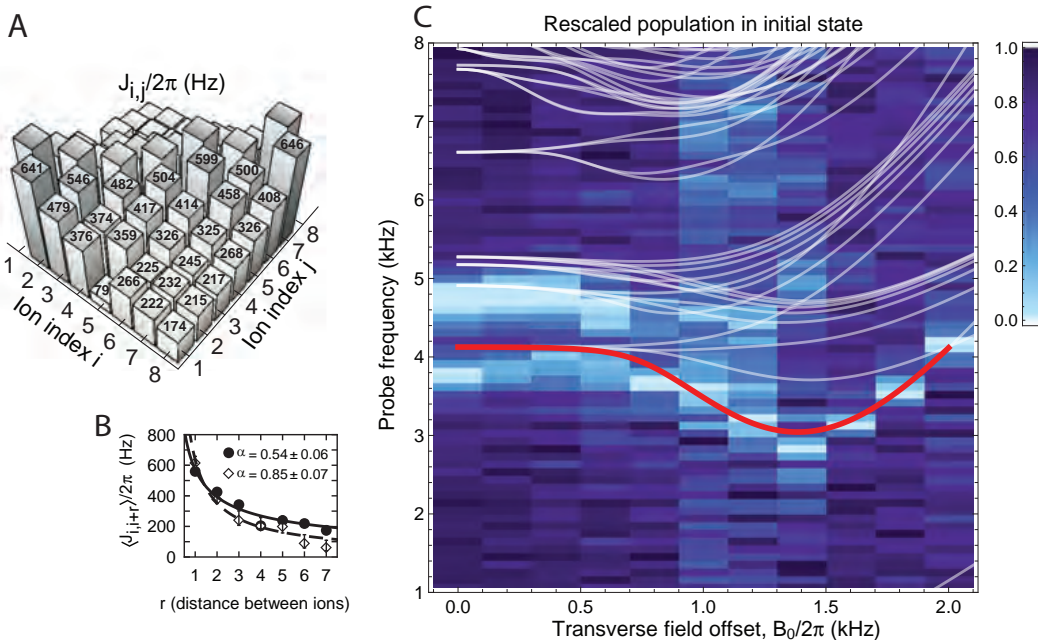


FIG. 6. (a) All elements of a Ising coupling matrix measured with a spectroscopic probe in the form of a modulated transverse field. (b) Measurements of two sets of Ising coupling matrices, demonstrating two different effective interaction ranges across the chain, with the solid lines best fits to inverse power law form expected in Eq. (13). (c) Rescaled populations in the approximate ground state versus a static transverse field offset B_0 and the modulation frequency of a small additional transverse field. Calculated energy levels, based on measurements of trap and laser parameters, are overlaid as thin white lines, and the lowest coupled excited state as a thick red line, showing the critical gap near $B_0/2\pi = 1.4$ kHz. The energy of the ground state is always taken to be zero.

III. EQUILIBRIUM STUDIES

Finding ground states of a complicated Hamiltonian has tremendous importance in various disciplines across condensed matter physics, quantum chemistry and computer science. In condensed matter physics, the rich phenomena of complex quantum systems can be understood by finding the ground states of the corresponding many-body Hamiltonian [87–89]. In quantum chemistry and molecular physics, the central problems is to determine the electronic structure and the ground-state energy of atoms and molecules [90]. In computer science, the ground state of the complex quantum Hamiltonian can be encoded to computational problems including optimization [91–93].

The computational tasks of finding the ground state of complex Hamiltonian are classically demanding because of the exponentially increasing Hilbert space of the Hamiltonian. A quantum simulator is expected to provide a solution beyond the limitations of classical computation. Recently various theoretical schemes for the ground-state problem have been proposed and proof-of principle experimental demonstrations have been performed, including adiabatic preparation [42, 73, 78, 81, 94–98], direct cooling by bath-engineering [99, 100], and algorithmic cooling schemes [101, 102]. For the case of adiabatic method, it has been shown to be closely related to adiabatic quantum computation, which is proved to be equivalent to a universal quantum computer [93].

We focus on the adiabatic preparation of the ground state of quantum spin models with trapped atomic ion spins, with a

description of the general scheme of the experimental procedure and various adiabatic ramping protocols. Following a discussion of the adiabatic protocol applied to varying numbers of trapped ion spins, we consider how this protocol can be optimized and applied to broader classes of spin models, and briefly discuss the case of a spin-1 system. These quantum spin models clearly show the essences of the adiabatic quantum simulation with wide applications. Moreover, these quantum spin models can describe a large class of many-body quantum physics in condensed matter such as quantum magnetism [103], spin glasses [104], and spin liquids [105]. The solutions of certain spin Hamiltonians are also connected to many other computational problems including optimization problems when the system is extended to 2 dimensions [93].

A. Adiabatic Ground State Preparation

The protocol of the adiabatic ground state preparation is analogous to that of adiabatic quantum computation. The process of quantum adiabatic computation works as follows [93, 106]: a quantum system is initialized to the ground state of a trivial Hamiltonian H_{triv} . Next, the Hamiltonian is adiabatically deformed into the Hamiltonian of interest H_{prob} , whose ground state encodes the solution of a problem that has been mapped to the final Hamiltonian. The adiabatic evolution is generated by

$$H(s) = (1 - s)H_{\text{triv}} + sH_{\text{prob}}, \quad (16)$$

where s is a time dependent parameter $s(t)$ changing from 0 to 1 during the time interval of $t = 0$ and $t = t_f$.

For instance, the trivial spin Hamiltonian can be an effective magnetic field as described by Eq. (3) and the Hamiltonian of interest can be a fully-connected transverse Ising model of Eq. (15). This approach allows the determination of ground states of the long range transverse field Ising model, whose Hamiltonian can easily be written, yet the spin ground state cannot always be predicted, even with just a few dozen spins [107].

In the experimental realization of trapped ions, the adiabatic protocol can be modified by the following steps without losing much generality as shown in in Fig. 7. First, the initialization of the spin and the motional modes is realized by standard optical pumping techniques and ground state cooling, respectively. Then, the ground state of Hamiltonian of the transverse field $B_\phi(t) \sum_i \sigma_\phi^i$, where σ_ϕ is orthogonal with σ_θ , is prepared, which is the polarized state along the ϕ -axis, $|\downarrow\downarrow \dots \downarrow\rangle_\phi$. The ratio between the strength of the transverse field B_ϕ and those of spin-spin interactions $J_{i,j}$ is adiabatically changed by either reducing B_ϕ or increasing $J_{i,j}$. At the end of the adiabatic evolution, where $J_{i,j}$ dominates, the final spin states are measured by the standard state-dependent fluorescence technique. The measurement in any direction on the Bloch sphere is straightforward by applying simple single qubit operation for the basis change. In principle, quantum state tomography can be also performed.

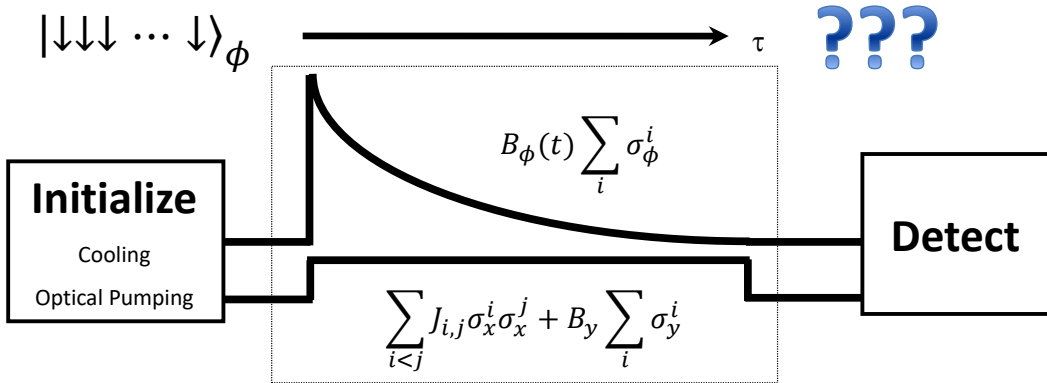


FIG. 7. After preparing the spins in the ground state of $B_\phi \sum_j \sigma_\phi^{(j)}$, a fully-connected transverse Ising model described by $\sum_{i,j} J_{i,j} \sigma_x^i \sigma_x^j + B_y \sum_i \sigma_y^i$ is applied with the condition of $B_\phi(t=0) \gg J_{i,j}$. Then the strength of transverse field $B_\phi(t)$ is adiabatically reduced to zero, where only the transverse Ising Hamiltonian remains. At various times along the path, the experiment is halted and the spin states are measured along any axis of the Bloch sphere.

Adiabatically preparing the ground state of a complicated many-body Hamiltonian generically begins by preparing the ground state of a simple Hamiltonian, then slowly transitioning to the Hamiltonian of interest, as in Eq. (16). Although the fidelity of this process can always be improved by transitioning more slowly, a practical upper limit on the transition time is enforced by the finite coherence time of the chosen experimental platform. Given a fixed transition time, it is possible to further optimize the preparation fidelity by adjusting the transition rate based on the local energy gap to the nearest excited state [78].

Such “local adiabatic evolution” can be used for improved preparation and determination of many-body ground states in a trapped-ion quantum simulator. Compared with other adiabatic methods, local adiabatic evolution [77] yields the highest probability of maintaining the ground state in a system that is made to evolve from an initial Hamiltonian to the Hamiltonian of interest. Compared with optimal control methods [108, 109], local adiabatic evolution may require knowledge of only the lowest $\sim N$ eigenstates of the Hamiltonian rather than all 2^N . These methods have been used in both linear Paul traps [78] and Penning traps [110] to demonstrate optimized ground state preparation as well as a method to find the ground state spin ordering, even when the evolution is non-adiabatic.

For example, to find the ground state of a fully-connected Ising Hamiltonian in Eq. (15) via an adiabatic protocol, the spins can be initialized to point along the transverse magnetic field direction with $B_y \gg \text{Max}(J_{i,j})$. This initial state is, to good approximation, the instantaneous ground state of the full Eq. (15). After initialization, the (time-dependent) transverse field $B_y(t)$ can then be ramped adiabatically from $B_y(t = 0) = B_0$ to $B_y(t = t_f) = 0$, ensuring that the system remains in its instantaneous ground state during its evolution. At the conclusion of the ramp, the ground state spin ordering of the Ising Hamiltonian [first term in Eq. (15)] may be either directly read out or used as a starting point for further experiments.

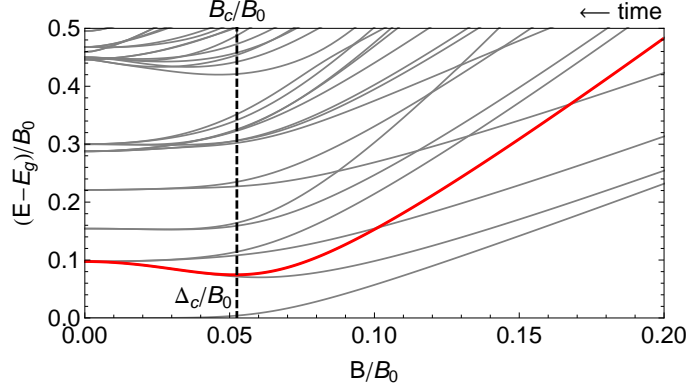


FIG. 8. Low-lying energy eigenvalues of Eq. (15) for $N = 6$, with the ground state energy E_g set to 0, $B_0 = 5J_{\text{max}}$, and the long-range $J_{i,j}$ couplings determined from experimental conditions (see text). Indicated in bold red is the first coupled excited state, the minimum of which determines the critical field B_c and the critical gap Δ_c . From 78.

Fig. 8 shows the energy level spectrum for the Hamiltonian in Eq. (15) for $N = 6$ spins. Since the Hamiltonian obeys Z_2 symmetry (as well as parity symmetry in the experiments), the ground state $|g\rangle$ is coupled to only a subset of the excited energy eigenstates. The first coupled excited state, shown in red in Fig. 8, is the lowest energy excited state $|e\rangle$ for which $\langle e | \sigma_y | g \rangle \neq 0$. This state displays a general property seen in most adiabatic quantum simulations – namely, the existence of a critical gap Δ_c that is central to parameterizing the adiabaticity of a given ramp. Many different ramp profiles allow one to transform from the initial Hamiltonian to the Ising Hamiltonian, each with different implications for adiabaticity and ground state preparation. Three possibilities are discussed below.

Linear Ramps – For a linear ramp, the time-dependent transverse field B_y in Eq. (15) takes the form $B_y^{\text{lin}}(t) = B_0(1 - t/t_f)$, with a ramp profile shown in Fig. 9(a). To determine whether such a ramp is adiabatic or not, it can be compared to the adiabatic criterion [111]

$$\left| \frac{\dot{B}_y(t)\epsilon}{\Delta_c^2} \right| \ll 1 \quad (17)$$

where $\dot{B}_y(t)$ is the rate at which the transverse field is changed and $\epsilon = \text{Max}[\langle e | dH/dB_y | g \rangle]$ is a number of order unity that parametrizes the coupling strength between the ground state $|g\rangle$ and the first coupled excited state $|e\rangle$. Eq. (17) highlights that fast ramps and small critical gaps can greatly decrease adiabaticity.

To satisfy the adiabatic criterion, a linear ramp must proceed slowly enough so that the total time $t_f \gg B_0/\Delta_c^2$. For the $N = 6$ Ising Hamiltonian shown in Fig. 8, $B_0 = 3.9$ kHz and $\Delta_c = 0.29$ kHz, giving the adiabaticity requirement $t_f \gg 46$ ms. This time is long compared with the typical coherence time of ion trap quantum simulation experiments. It is therefore desirable to seek alternative ways to decrease $B(t)$ more quickly while maintaining adiabaticity.

Exponential Ramps – Decreasing the transverse field exponentially according to $B_y^{\text{exp}}(t) = B_0 \exp(-t/\tau)$, with $t_f = 6\tau$, can yield a significantly more adiabatic evolution than linear ramps for the same t_f . Fig. 8 shows that the instantaneous gap Δ between the ground and first coupled excited state is large at the beginning of the ramp and small only when B approaches 0. Exponential ramps exploit this gap structure by quickly changing the field at first, then gradually slowing the rate of change as

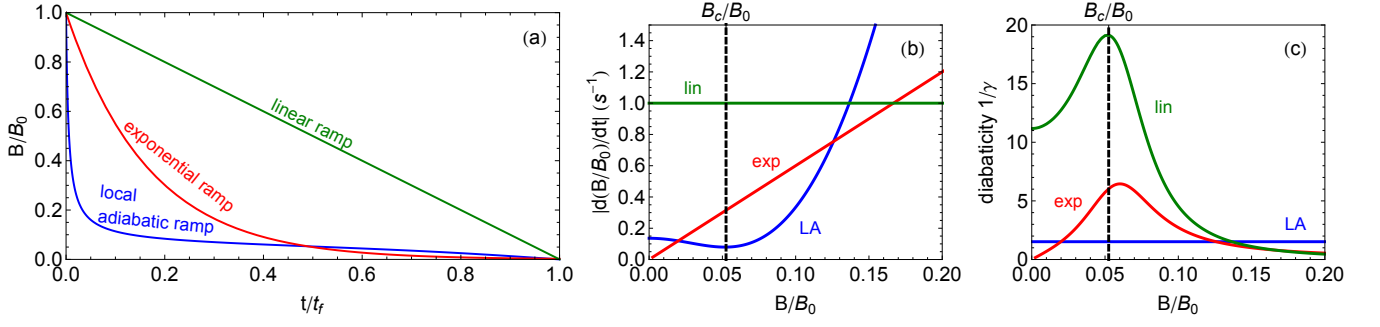


FIG. 9. (a) Local adiabatic ramp profile calculated for the energy levels in Fig. 8, along with a linear ramp and an exponential ramp with decay constant $\tau = t_f/6$. (b) The slope of the local adiabatic (LA) ramp is minimized at the critical field value B_c , and is smaller than the slopes of the exponential and linear ramps at the critical point. (c) The inverse of the adiabaticity parameter γ (see text) is peaked near the critical point for exponential and linear ramps but constant for the local adiabatic profile. Adapted from 78.

$t \rightarrow t_f$. Such ramps have been used to produce ground states in several of the previously discussed experiments, such as [95],[42] and [73].

At the critical point of the Hamiltonian shown in Fig. 8, $|\dot{B}_{exp}(t)| = 0.3B_0/t_f$. The adiabaticity criterion of Eq. (17) then requires $t_f \gg 14.5$ ms, a factor of 3 less time than the requirement found for linear evolution. Note that the adiabaticity gains of exponential ramps can be realized whenever the critical gap occurs towards the end of the ramp ($B_c/B_0 < \tau/t_f$), which is generally the case for the transverse Ising Hamiltonian of Eq. (15).

Local Adiabatic Ramps – Local adiabatic ramps seek to keep the adiabaticity fixed at all points along the evolution by adjusting $\dot{B}_y(t)$ based on the instantaneous gap $\Delta(B_y(t))$ that varies with the field profile $B_y(t)$ [77, 112]. If the adiabaticity parameter is defined as

$$\gamma = \left| \frac{\Delta(B_y(t))^2}{\dot{B}_y(t)} \right| \quad (18)$$

then a local adiabatic ramp would follow the profile $B_y(t)$ that solves the differential equation 18 with γ fixed. Adiabaticity then requires $\gamma \gg 1$.

To solve Eq. (18), it is necessary to know $\Delta(t)$ everywhere along the evolution. This requires knowledge of the first *coupled* excited state of the N -spin Hamiltonian of Eq. (15), which is always the 2nd excited state at small B_y and the $(N + 1)$ st excited state at large B_y . Determining the local adiabatic evolution profile therefore relies on calculation of only the lowest $\sim N$ eigenvalues, which is much more computationally approachable than direct diagonalization of a $2^N \times 2^N$ matrix [113].

For a local adiabatic ramp, the critical time t_c may be calculated by integrating Eq. (18). Since $\dot{B}_y(t)$ is negative throughout the evolution,

$$t_c = \gamma \int_{B_c}^{B_0} \frac{dB}{\Delta^2(B)} \quad (19)$$

Similarly, the total evolution time is given by

$$t_f = \gamma \int_0^{B_0} \frac{dB}{\Delta^2(B)} \quad (20)$$

which shows a linear relationship between the total time t_f and the adiabaticity parameter γ . Satisfying the adiabaticity condition $\gamma \gg 1$ for the Hamiltonian in Fig. 8 implies $t_f \gg 3.6$ ms, a factor of 4 and 12 less time than exponential and linear ramps, respectively. The fact that local adiabatic evolution can lead to faster ramps while satisfying adiabaticity has been well-explored in [77], where it was shown that local adiabatic ramps could recover the quadratic speedup of Grover's quantum search algorithm. In contrast, it was found that linear ramps offer no improvement over classical search [106].

Fig. 9(a) compares a linear, exponential, and local adiabatic ramp profile for the Hamiltonian shown in Fig. 8. The local adiabatic ramp spends much of its time evolution in the vicinity of the critical point, since the transverse field changes slowly on account of the small instantaneous gap. This is further illustrated in Fig. 9(b), which shows that at the critical point, the slope of the local adiabatic ramp is minimized and smaller than slopes of the exponential or linear ramps. As a result, the inverse adiabaticity $1/\gamma$ is peaked near the critical point for exponential and linear ramps, greatly increasing the probability of

non-adiabatic transitions away from the ground state (see Fig. 9(c)). By design, the local adiabatic ramp maintains constant adiabaticity for all values of B and does not suffer from large non-adiabaticities near B_c .

Beyond Adiabatic ramps - While adiabatic simulation protocol allows for the preparation of the ground state of non-trivial spin models, maintaining the adiabatic condition (Eq.(17)) for a large system within the constraint of an experimentally realistic coherence time will be challenging. Alternate protocols have been explored to bypass the strict requirements of adiabaticity, while achieving high ground state probability. For example, a ‘Bang-bang’ control of the Hamiltonian has been suggested [114, 115], where the initial trivial Hamiltonian can be quenched to an intermediate Hamiltonian, followed by a final quench to the problem Hamiltonian. In another approach, a classical-quantum hybrid protocol (the Quantum Approximate Adiabatic Algorithm, or QAOA [18]) theoretically enables ultra-fast creation of ground states [116]. Here, we restrict our discussions to adiabatic simulation protocols.

B. Experimental Progress in Adiabatic Quantum Simulation

1. Transverse Ising model with a small number of spins

The adiabatic preparation of the ground state for the transverse Ising model was first demonstrated with two trapped ion spins [94, 97], followed by experiments with three spins [81, 84, 95, 96, 117]. These entry experiments demonstrated the adiabatic evolution from para-magnetic initial state to magnetically ordered ground states and allowed tests of adiabaticity [96] and direct measures of entanglement in the ground state [81, 95]. The three-spin system moreover supports spin frustration, or a competition between the nearest and next-nearest couplings in the case of antiferromagnetic ground states. By tuning the system to have either ferromagnetic and anti-ferromagnetic ground states, two different types of magnetic order were indeed measured, paralleling the two different classes of entanglement known to exist with exactly three spins [118].

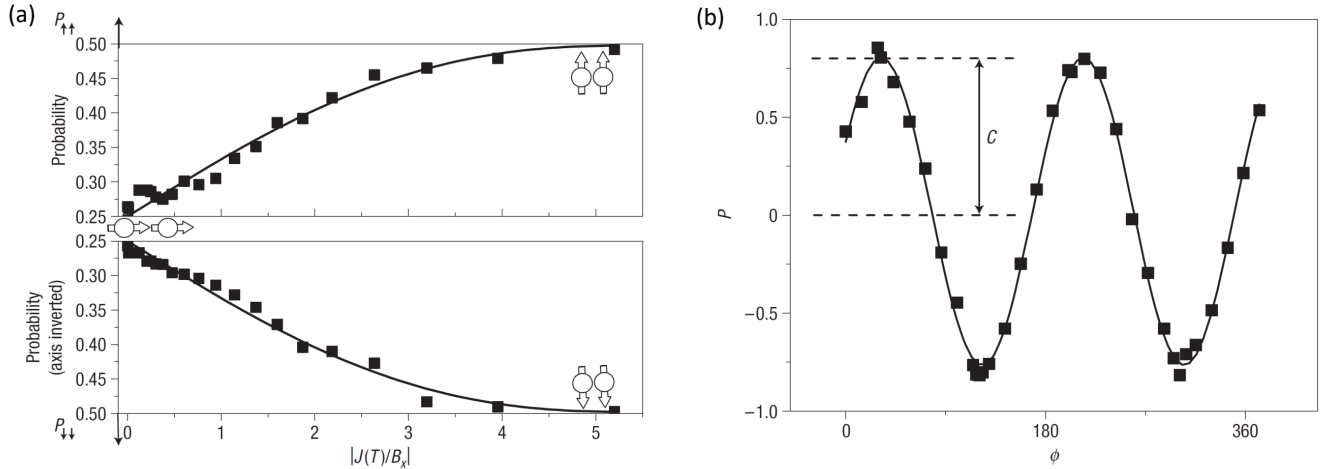


FIG. 10. (a) Adiabatic evolution of two trapped ion spins from a paramagnetic state to ferromagnetic state. (b) Entanglement of the prepared ground state in the ferromagnetic Hamiltonian. From 94.

For the case of three Ising spins, the transverse Ising Hamiltonian (15) is reduced to

$$H_3 = J_1(\sigma_x^{(1)}\sigma_x^{(2)} + \sigma_x^{(2)}\sigma_x^{(3)}) + J_2\sigma_x^{(3)}\sigma_x^{(1)} + B_y(t)(\sigma_y^{(1)} + \sigma_y^{(2)} + \sigma_y^{(3)}), \quad (21)$$

where the transverse field and the Ising interaction are chosen to act along the y -axis and x -axis, respectively. This is the simplest Hamiltonian that can exhibit frustration in the ground state due to a compromise between the various Ising couplings.

As seen in Eq. (12), the sign and the strength of the Ising couplings $J_{i,j}$ can be controlled by the proper choice of the driving field detuning from spin resonance μ . For three spins, the expected and measured nearest-neighbor (NN) interactions, $J_1 \equiv J_{1,2} = J_{2,3}$ and the next-nearest-neighbor (NNN) interaction $J_2 \equiv J_{1,3}$ are shown in Fig. 5. For certain ranges of the drive field detuning, both NN and NNN couplings have anti-ferromagnetic (AFM) interactions ($J_1, J_2 > 0$), and for other domains both show ferromagnetic (FM) interactions ($J_1, J_2 < 0$).

Figure 11(a) shows the time evolution for the Hamiltonian frustrated with nearly uniform AFM couplings and gives almost equal probabilities for the six AFM states ($|\downarrow\downarrow\uparrow\rangle, |\uparrow\downarrow\downarrow\rangle, |\downarrow\uparrow\uparrow\rangle, |\uparrow\uparrow\downarrow\rangle, |\downarrow\uparrow\downarrow\rangle$, and $|\uparrow\downarrow\uparrow\rangle$) (three-quarters of all possible spin states)

at $B_y \approx 0$. Because $J_2 < 0.8J_1$ for this data, a population imbalance also develops between symmetric ($|\downarrow\downarrow\downarrow\rangle$ and $|\uparrow\uparrow\uparrow\rangle$) and asymmetric ($|\downarrow\downarrow\uparrow\rangle$, $|\uparrow\downarrow\downarrow\rangle$, $|\downarrow\uparrow\uparrow\rangle$, and $|\uparrow\uparrow\downarrow\rangle$) AFM states. Figure 11(b) shows the evolution to the two ferromagnetic states ($|\downarrow\downarrow\downarrow\rangle$ and $|\uparrow\uparrow\uparrow\rangle$) as $B_y \rightarrow 0$, where all interactions are FM.

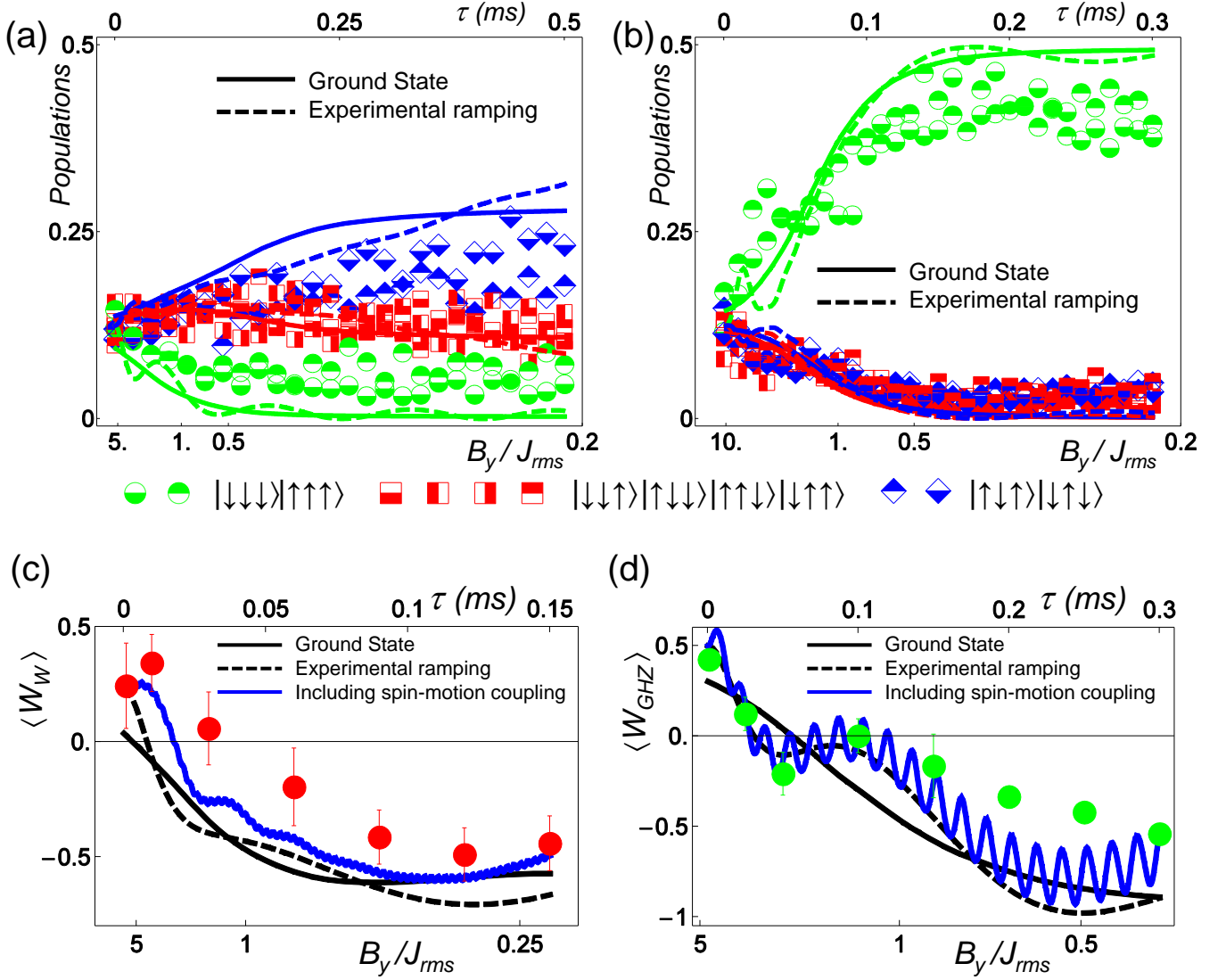


FIG. 11. Evolution of each of the eight spin states, measured with a CCD camera, plotted as B_y/J_{rms} is ramped down in time. The dotted lines correspond to the populations in the exact ground state and the solid lines represent the theoretical evolution expected from the actual ramp. (a) All interactions are AFM. The FM-ordered states vanish and the six AFM states are all populated as $B_y \rightarrow 0$. Because $J_2 \approx 0.8J_1$, a population imbalance also develops between symmetric and asymmetric AFM. (b) All interactions are FM, with evolution to the two ferromagnetic states as $B_y \rightarrow 0$. (c) Entanglement generation for the case of all AFM interaction, where symmetric W-state witness W_W is used. The entanglement emerges for $B_y/J_{rms} < 1.1$. (d) Entanglement generation for the all FM interactions, where the GHZ witness W_{GHZ} is used. The entanglement occurs when $|B_y/J_{rms}| < 1$. In both (c) and (d) the error bars represent the spread of the measured expectation values for the witness, likely originating from the fluctuations of experimental conditions. The black solid lines are theoretical witness values for the exact expected ground states, and the black dashed lines describe theoretically expected values at the actual ramps of the transverse field B_y . The blue lines reveal the oscillation and suppression of the entanglement due to the remaining spin-motion couplings, showing better agreement to the experimental results. Adapted from 81.

The adiabatic evolution of the ground state of Hamiltonian (21) from $B_y \gg J_{rms}$ to $B_y \ll J_{rms}$ should result in an equal superposition of all ground states and therefore be entangled. For instance, for the isotropic AFM case, the ground state is expected to be $|\downarrow\downarrow\uparrow\rangle + |\uparrow\downarrow\downarrow\rangle + |\downarrow\uparrow\uparrow\rangle - |\uparrow\uparrow\downarrow\rangle - |\downarrow\downarrow\downarrow\rangle - |\uparrow\uparrow\uparrow\rangle$. For the FM case, the ground state is a GHZ as $|\downarrow\downarrow\downarrow\rangle - |\uparrow\uparrow\uparrow\rangle$. The entanglement in the system at each point in the adiabatic evolution can be characterized by measuring particular entanglement

witness operators [119]. When the expectation value of such an operator is negative, this indicates entanglement of a particular type defined by the witness operator. For the AFM (frustrated) case as shown in Fig. 11(c), the expectation of the symmetric W state witness, $W_W = (4 + \sqrt{5})\hat{I} - 2(\hat{J}_x^2 + \hat{J}_y^2)$ is measured [119]. For the FM case as shown in Fig. 11(d), the expectation of the symmetric GHZ witness operator $W_{\text{GHZ}} = 9\hat{I}/4 - \hat{J}_x^2 - \sigma_y^{(1)}\sigma_y^{(2)}\sigma_y^{(3)}$ [119, 120] is measured, where \hat{I} is the identity operator and $\hat{J}_i \equiv \frac{1}{2}(\sigma_i^{(1)} + \sigma_i^{(2)} + \sigma_i^{(3)})$ is proportional to the l th projection of the total effective angular momentum of the three spins. In both cases, as shown in Figs. 11(c) and (d), entanglement of the corresponding form is clearly observed during the adiabatic evolution.

2. Onset of quantum many-body effects with increasing system size

The ground state in the transverse field Ising model, Eq. (15) undergoes a crossover between polarized/paramagnetic and magnetically ordered spin states, as the relative strengths of the transverse field B_y and the Ising interactions $J_{i,j}$ are varied. For $|B_y/J_{i,j}| \gg 1$, the ground state has the spins independently polarized (paramagnetic phase). For $|B_y/J_{i,j}| \ll 1$, the ground state is magnetically ordered for $|B_y/J_{i,j}| \ll 1$, with ferromagnetic order for $J_{i,j} < 0$ in Eq. (15). A second order quantum phase transition is predicted for this model in the thermodynamic limit [60] when the magnitude of the transverse field is comparable to the interaction strength. A finite system does not support a phase transition, but shows a smooth crossover from the paramagnetic to the spin-ordered phases. The crossover becomes sharper as the system size is increased, as measured in [42] by increasing the system size ion by ion, from $N = 2$ to $N = 9$. The sharpening of the crossover from paramagnetic to ferromagnetic spin-order with system size (Fig. 12) is consistent with an onset of the quantum phase transition. The presence or absence of a spin-order can be quantified by adopting a suitable ‘order parameter’. For example, the average absolute magnetization per site along the Ising direction, $m_x = \frac{1}{N} \sum_{s=0}^N |N - 2s|P(s)$ assumes a value of $m_x = 1$ for the ideal ferromagnet state while $m_x \approx 0$ in the paramagnetic state. Here, $P(s)$ is the probability of finding s spins in the $|\uparrow\rangle$ state ($s = 0, 1, 2, \dots, N$). Higher order moments of the distribution of measured spins may be more suitable to extract the phase transition point from experiments performed on final system sizes. Figure 12a compares the theoretically expected values of the average absolute magnetization to the fourth moment known as the Binder cumulant, $g = \sum_{s=0}^N (N - 2s)^4 P(s) / (\sum_{s=0}^N (N - 2s)^4 P(s))^2$ for up to $N = 100$ spins in an all-to-all coupled ferromagnetic transverse Ising model. In the figure, both the magnetization and Binder cumulant have been scaled to take into account ‘trivial’ finite size effects [42]. It is to be noted that the Binder cumulant shows greater sensitivity to the change of spin-order when the transverse field and Ising couplings are comparable in strength, and thus can be more reliably used to estimate the phase transition point from experiments with finite systems.

Although the ferromagnetic spin order was observed in adiabatic quantum simulation experiments with up to $N = 16$ ions [73], adiabatic preparation of the ground state in transverse field Ising model becomes harder if the interactions are long-ranged and antiferromagnetic ($J_{i,j} > 0$). This is because long-ranged AFM interactions lead to competing pairwise spin order, or frustration, as explained with $N = 3$ spins [95] in the previous subsection. Intuitively, the longer the range of AFM interaction is, the easier it is to create spin-flip excitations. Thus the critical field required to destroy the AFM spin order is less than that with a relatively shorter range interaction. The ‘critical gap’ in the many-body energy spectra also decreases with increasing range of the AFM couplings (Fig. 13). The reduction of the critical gap with increased range of interaction was experimentally probed in a quantum simulation of the transverse field Ising model, Eq.15 with the interaction profile following an approximate power law, Eq.13 ($J_0 > 0$) for $N = 10$ [73]. The ratio of the transverse field to the Ising couplings was varied quasi-adiabatically from a high transverse field to a final value of $B/J_0 = 0.01$. As the critical gap reduced with increased range of interactions, more excitations were created, which resulted in a reduction in the ground state order, as measured by a reduction in the structure function, $S(k) = \frac{1}{N-1} \left| \sum_{r=1}^{N-1} C(r) \exp(ikr) \right|$ at $k = \pi$. Here, $C(r) = \frac{1}{N-r} \sum_{m=1}^{N-r} \left(\langle \sigma_x^{(m)} \sigma_x^{(m+r)} \rangle - \langle \sigma_x^{(m)} \rangle \langle \sigma_x^{(m+r)} \rangle \right)$ is the average correlation of spins separated by r sites along the Ising direction x , and $S(\pi)$ quantifies the nearest-neighbor antiferromagnetic spin order.

3. Optimizing adiabatic ramps

To determine the effects of a chosen adiabatic ramp protocol, the probability of creating the ground state can be measured following linear, exponential, and locally adiabatic ramps of identical times. [78] used $N = 6$ ions and chose the trap voltages and the laser detuning μ to give AFM spin-spin interactions of the form $J_{i,j} \approx (0.77 \text{ kHz})/|i - j|$. These long-range AFM interactions lead to a fully-connected, frustrated system as all couplings cannot be simultaneously satisfied. Nevertheless, the ground state of this system reduces to an equal superposition of the two Néel-ordered AFM states, $(|010101\rangle + |101010\rangle)/\sqrt{2}$.

The data in Fig. 14 show how the AFM ground state probability grows during a single 2.4 ms linear, exponential, or local adiabatic ramp. Each data point is the result of 4000 repetitions of the same experiment, with error bars that account for statistical

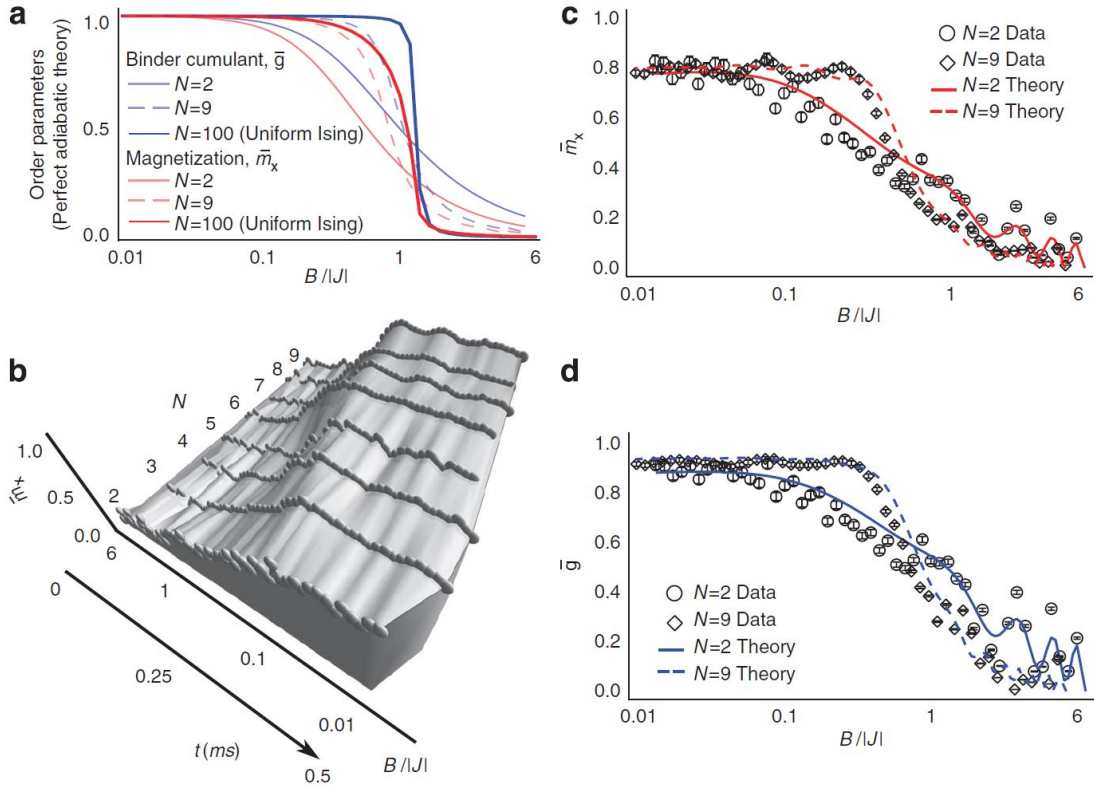


FIG. 12. Paramagnetic-to-Ferromagnetic crossover in a small collection of trapped ion spins (a) Theoretical values of order parameters versus vs $B/|J|$ for $N = 2$ and $N = 9$ spins with non-uniform Ising couplings following the experiment in Ref. [42] and assuming perfect adiabatic time evolution. Here, J is the average Ising coupling. The order parameters, the Binder Cumulant and the magnetization are calculated by directly diagonalizing the relevant Hamiltonian 1. Order parameters are also calculated for a moderately large system ($N=100$) with uniform Ising couplings, to show the difference between these order parameters. (b) Measured magnetization vs $B/|J|$ (and simulation time) plotted for $N=2$ to $N=9$ spins, and scaled to the number of spins. As $B/|J|$ is lowered, the spins undergo a crossover from a paramagnetic to ferromagnetic phase. The crossover curves sharpen as the system size is increased from $N = 2$ to $N = 9$, prefacing a phase transition in the limit of infinite system size. The oscillations in the data arise from the imperfect initial state preparation and non-adiabaticity due to finite ramping time. Measured magnetization (c) and Binder cumulant (d) vs. $B/|J|$ for for $N = 2$ (circles) and $N = 9$ spins (diamonds) with representative detection error bars. The data deviate from unity at $B/|J| = 0$ owing to decoherence driven by the Raman transitions creating the Ising couplings. The theoretical curves (solid line $N = 2$ and dashed line for $N = 9$ spins) are calculated by averaging over 10,000 quantum trajectories. [from [42]].

uncertainty as well as estimated drifts in the Ising coupling strengths. In agreement with the arguments above, the data show that local adiabatic ramps prepare the ground state with higher fidelity than exponential or linear ramps. The ground state population grows quickly under local adiabatic evolution since the transverse field $B(t)$ is reduced quickly at first. In contrast, the linear ramp does not approach the paramagnetic to AFM phase transition until ~ 2 ms, and the AFM probability is suppressed until this time.

The solid lines in Fig. 14 plot the theoretical prediction of the ground state probability with no free parameters. In each case, the Schrödinger equation is numerically integrated using Hamiltonian (15), the desired $B(t)$, and the initial state $|\psi(0)\rangle = |000\dots\rangle_y$. At the end of the ramp, the overlap between the final state $|\psi(t_f)\rangle$ and the AFM ground state $(|010\dots\rangle + |101\dots\rangle)/\sqrt{2}$ is calculated to extract the probability of the ground state spin configuration. Effects of decoherence-induced decay in the ground state probability are included by multiplying the calculated probability at time t by $\exp[-t/t_d]$, where t_d is the measured $1/e$ coherence time of the spin-spin interactions.

Ground state identification – Interestingly, the ground state spin ordering may be determined in an experiment even when the ramp is non-adiabatic. The key to ground state identification is to examine the probability distribution of all spin configurations at the conclusion of the ramp and select the most prevalent state in the final eigenbasis. Consider an experiment where the spins are initialized into $|000\dots\rangle_y$ (as usual) and the transverse field $B(t)$ is instantly switched from $B = B_0$ to $B = 0$. Measurement along the x -direction would yield an equal superposition of all spin states; in this instance, the ground state is just as probable

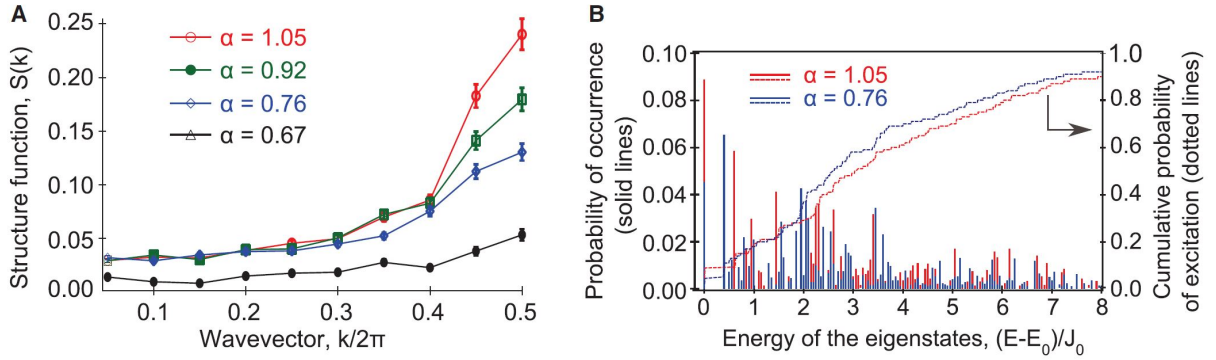


FIG. 13. (A) Structure function $S(k)$ for various ranges of AFM interactions, for $B/J_0 = 0.01$ in a system of $N = 10$ spins. The increased level of frustration for the longer-range interactions reduces the observed antiferromagnetic spin order. The detection errors may be larger than shown here for the longest range of interactions, owing to spatial crosstalk from their closer spacing. (B) Distribution of observed states in the spin system, sorted according to their energy E_i (with E_0 denoting the ground state energy) calculated exactly from Eq. (15) with $B = 0$. Data are presented for two ranges (red for $\alpha = 1.05$ and blue for $\alpha = 0.76$). The dashed lines indicate the cumulative energy distribution functions for these two ranges. Adapted from [73].

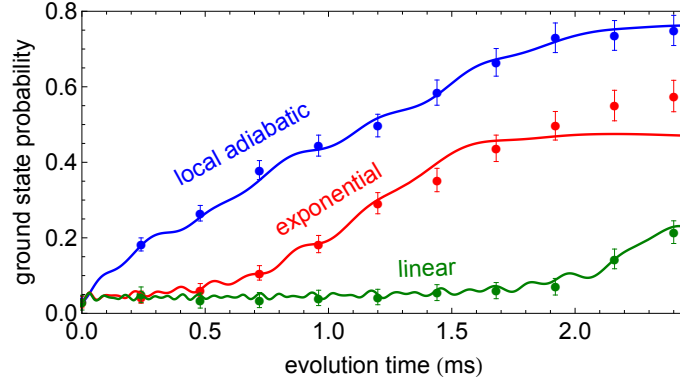


FIG. 14. Probability of preparing the AFM ground state for various times during $t_f = 2.4$ ms simulations with three different ramp profiles. The linear ramp takes ~ 2.3 ms to reach the critical point, while the local adiabatic and exponential ramps need only 1.2 ms. Locally adiabatic ramps yield the highest preparation fidelity at all times. Adapted from [78].

as any other state. If the transverse field $B(t)$ is instead ramped at a fast but finite rate, the quantum simulation is slightly more adiabatic than the instantaneous case, and the ground state becomes slightly more prevalent than any other state. When $B(t)$ is ramped slowly enough, the ground state population is nearly 100% and dominates over that of any other state.

A close analogy may be drawn with a Landau-Zener process [121] in a two-level system comprised of the ground and first coupled excited states. Adiabatic ramps correspond to half of a Landau-Zener process, in which $B(t)$ starts with $B \gg J$ and ends at $B = 0$. One can write an analytic expression to calculate the transition probability for this half-Landau-Zener evolution [122], which has a maximum value of 0.5 for an instantaneous ramp. Any fast but finite ramp will give a transition probability < 0.5 , and the ground state will always be more prevalent than the excited state.

The technique of identifying the most prevalent state as the ground state is subject to some limitations. First, the initial state (before the ramp) should be a uniform superposition of all spin states in the measurement basis – a condition satisfied by preparing the state $|000 \dots\rangle_y$ and measuring along \hat{x} . If some spin states are more prevalent than the ground state initially, then some non-zero ramp time will be necessary before the ground state probabilities “catch up” and surpass these initially prevalent states. Second, the ramp must not cross any first-order transitions between ordered phases, as non-adiabatic ramps may not allow sufficient evolution time towards the new ground state order. In addition, the initial and final states must share the same symmetry properties.

Finally, a good determination of the ground state requires that the difference between the measured ground state probability P_g and next excited state probability P_e be large compared with the experimental uncertainty, which is fundamentally limited by quantum projection noise $\sim 1/\sqrt{n}$ after n repetitions of the experiment [123]. This implies that the most prevalent ground

state can be determined reliably after repeating the measurement $n > (P_g^2 + P_e^2)/(P_g - P_e)^2$ times. Assuming an exponential distribution of populated states during the ramp (as may be expected from Landau-Zener-like transitions), the number of required runs should then scale as $n \sim (\bar{E}/\Delta)^2$ in the limit $\bar{E} \gg \Delta$, where \bar{E} is the mean energy imparted to the spins during the ramp, and Δ is the energy splitting between the ground and first coupled excited state.

If the gap shrinks exponentially with the number of spins N (i.e. $\Delta \sim e^{-N}$), ground state identification requires an exponential number of measurements n in the simulation. However, in cases where the gap shrinks like a power law ($\Delta \sim N^{-\alpha}$), the most prevalent state can be ascertained in a time that scales polynomially with the number of spins. Regardless of the scaling, techniques that improve the ground state probability (such as local adiabatic evolution) can greatly increase the contrast of the most prevalent state and reduce the number of necessary repetitions.

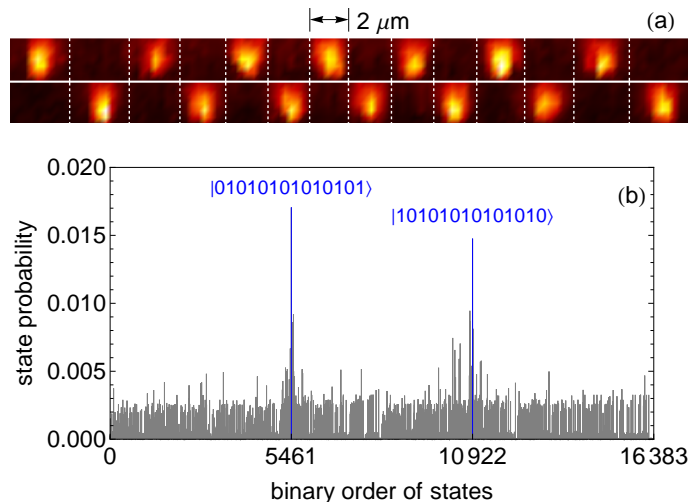


FIG. 15. (a) Camera images of experimentally prepared AFM ground states for $N = 14$. (b) State probabilities of all $2^{14} = 16384$ spin configurations for a 14-ion system following a local adiabatic ramp. The Néel-ordered ground states are unambiguously the most prevalent, despite a total probability of only 3%. From [78].

Fig. 15 demonstrates the resiliency of most-prevalent state selection to ramps that are far from adiabatic. Identification of the ground state proceeds easily, even though the total ground state probability is only $\sim 3\%$. The requirement of satisfying the adiabatic criterion is replaced only by the requirement that the most prevalent state probabilities are accurately resolvable compared with those of any other states. While the method should remain robust for even larger N , more adiabatic ramps (generated by longer ramp times or stronger spin-spin couplings) will decrease the number of experimental repetitions needed to clearly resolve the state probabilities.

4. Classical Ising model

Adiabatic protocols can also be used to create the ground states of a classical spin model, catalyzed by quantum fluctuations. Consider a system described by the transverse Ising model accompanied by a longitudinal field:

$$H = \sum_{i,j} J_{i,j} \sigma_x^i \sigma_x^j + B_x \sum_i \sigma_x^i + B_y(t) \sum_i \sigma_y^i \quad (22)$$

When the transverse field B_y is set equal to 0, and the longitudinal field B_x is varied, this Hamiltonian exhibits many distinct ground state phases separated by first-order classical phase transitions. Yet even for just a few spins, the various ground states at different B_x are classically inaccessible in a physical system at or near zero temperature due to the absence of thermal fluctuations to drive the phase transitions [60].

Nevertheless, these classically inaccessible ground states can be created by applying a transverse field (which does not commute with the longitudinal-field Ising Hamiltonian) to introduce quantum fluctuations. Using $N = 6$ or $N = 10$ spins, this technique has been used to experimentally identify the locations of the multiple classical phase transitions and to preferentially populate each of the classical ground states that arise for varying strengths of the longitudinal field [98]. The ground state spin ordering reveals a Wigner-crystal spin structure [124], maps on to a number of energy minimization problems [125], and shows the first steps of the complete devil's staircase [126] which would emerge in the $N \rightarrow \infty$ limit.

Fig. 16(a) shows the energy eigenvalues of the Hamiltonian given in Eq. (22) with $B_y = 0$ for a system of 6 spins. The ground state passes through three level crossings as B_x is increased from 0, indicating three classical first-order phase transitions separating four distinct spin phases. For each B_x , there is a quantum critical point at some finite B_y characterized by a critical gap Δ_c (inset of Fig. 16(b)). When B_x is near a classical phase transition, the near energy-degeneracy of spin orderings shrinks the quantum critical gap, as shown in Fig. 16(b).

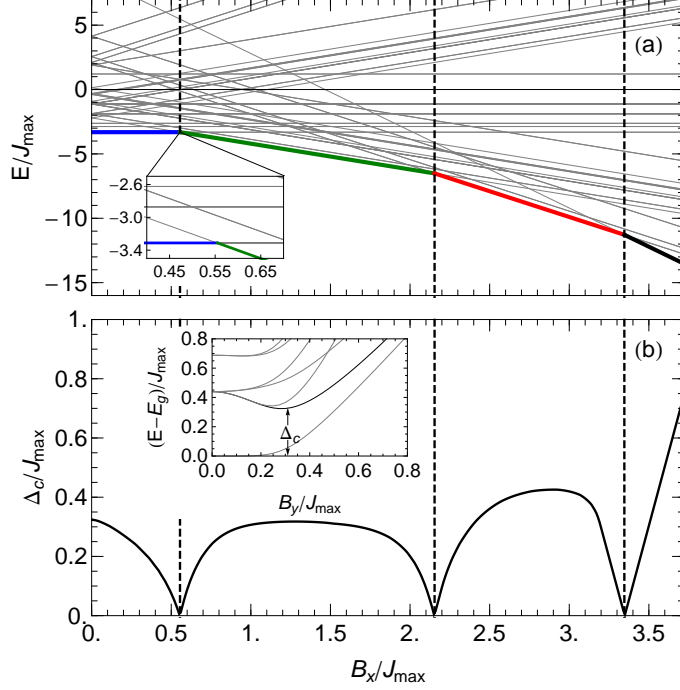


FIG. 16. (a) Low-lying energy eigenvalues of Eq. (22) for $B_y = 0$ and $N = 6$, with the long-range $J_{i,j}$ couplings determined from experimental conditions (see text). Level crossings (inset) indicate the presence of first-order phase transitions in the ground state. (b) The critical gap Δ_c shrinks to zero at the three phase transitions (vertical dashed lines). Inset: low-lying energy levels of Eq. (22) with $B_x = 0$. From [98].

Long-range interactions give rise to many more ground state spin phases than does a nearest-neighbor-only Ising model. Consider a nearest-neighbor AFM model with N total spins and a ground-state ordering $|\dots\downarrow\uparrow\downarrow\uparrow\downarrow\uparrow\dots\rangle$. An excited state at $B_x = 0$ may have an additional spin polarized along $|\downarrow\rangle$, either by making a kink of type $|\dots\downarrow\uparrow\downarrow\uparrow\downarrow\uparrow\dots\rangle$ or a spin defect of type $|\dots\downarrow\uparrow\downarrow\uparrow\downarrow\uparrow\dots\rangle$. The interaction energy gain of making n kinks is $2nJ$, while the field energy loss is $2nB_x$. At $B_x/J = 1$, multiple energy levels intersect to give a first-order phase transition. Similarly, the energy gain of making n spin defects is $4nJ$ and the loss is $2nB_x$, so a second phase transition occurs at $B_x/J = 2$. Only three different ground state spin phases are observable as B_x is varied from $0 \rightarrow \infty$, independent of N , and there is a large degeneracy of spin eigenstates at the phase transitions. The presence of long-range interactions lifts this degeneracy and admits $[N/2] + 1$ distinct spin phases with $\{0, 1, \dots, [N/2]\}$ spins in state $|\uparrow\rangle$, where $[N/2]$ is the integer part of $N/2$.

To create these various spin phases, each experiment begins by optically pumping the effective spins to the state $|\downarrow\downarrow\downarrow\dots\rangle_z$. The spins are then coherently rotated into the equatorial plane of the Bloch sphere so that they point along $\vec{B} = B_x\hat{x} + B_y(0)\hat{y}$, with B_x varied between different simulations. The Hamiltonian of Eq. (22) is then switched on at $t = 0$ with the chosen value of B_x and $B_y(0) = 5J_{\max}$. The transverse field (which provides the quantum fluctuations) is ramped down to $B_y \approx 0$ exponentially with a time constant of $600 \mu\text{s}$ and a total time of 3 ms, which sacrifices adiabaticity in order to avoid decoherence effects. At $t = 3$ ms, the Hamiltonian is switched off and the x -component of each spin is measured by applying a global $\pi/2$ rotation about the \hat{y} axis, illuminating the ions with resonant light, and imaging the spin-dependent fluorescence using an intensified CCD camera. Experiments are repeated 4000 times to determine the probability of each possible spin configuration. Detection errors ($\epsilon = 7\%$ for a single spin) can be compensated by multiplying a matrix describing the expected multi-spin error by the vector containing the measured probability of each spin configuration [73, 79].

The order parameter of net magnetization along x , $m_x = N_\uparrow - N_\downarrow$, can then be investigated as a function of longitudinal field strength. The magnetization of the ground state spin ordering of Eq. (22) is expected to yield a staircase with sharp steps at the phase transitions (red line in Fig. 17(a)) when $B_y = 0$ [126]. The experimental data (blue points in Fig. 17(a)) show an averaged magnetization with heavily broadened steps due largely to the non-adiabatic exponential ramp of the transverse field.

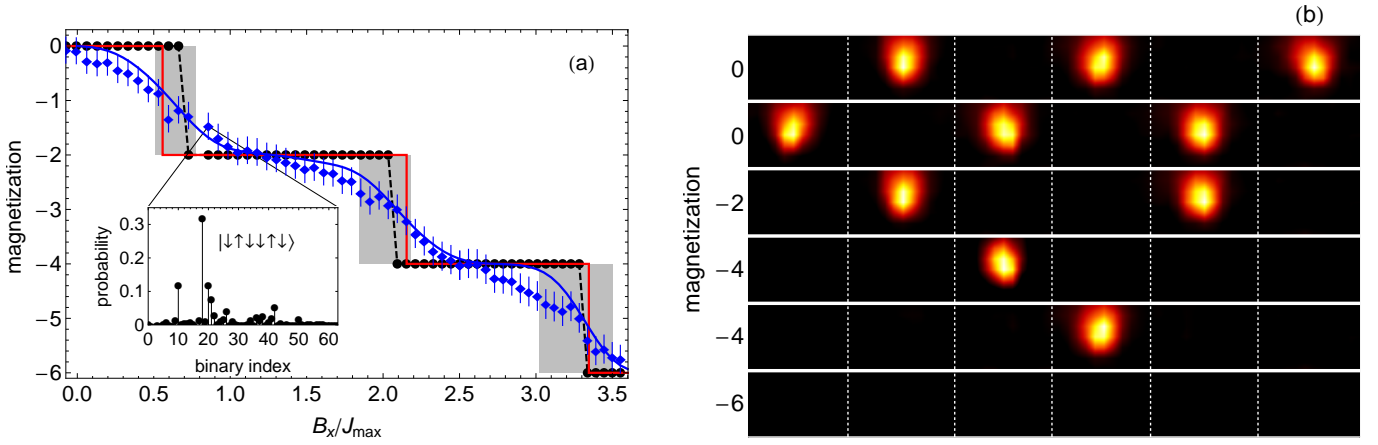


FIG. 17. (a) Magnetization ($m_x = N_\uparrow - N_\downarrow$) of 6 ions for increasing axial field strength. Red, solid: magnetization of the calculated ground state, with the step locations indicating the first-order phase transitions. Blue diamonds: average magnetization of 4000 experiments for various B_x . Blue, solid: magnetization calculated by numerical simulation using experimental parameters. Black, dashed: magnetization of the most probable state (see inset) found at each B_x value. Gray bands indicate the experimental uncertainty in B_x/J_{\max} at each observed phase transition. (b) Linearly interpolated camera images of the ground states found at each step in (a): $|\downarrow\uparrow\downarrow\uparrow\downarrow\uparrow\rangle$ and $|\uparrow\uparrow\downarrow\downarrow\uparrow\uparrow\rangle$ ($m_x = 0$), $|\downarrow\uparrow\downarrow\uparrow\downarrow\uparrow\rangle$ ($m_x = -2$), $|\downarrow\downarrow\uparrow\uparrow\downarrow\downarrow\rangle$ and $|\downarrow\downarrow\downarrow\uparrow\downarrow\downarrow\rangle$ ($m_x = -4$), and $|\downarrow\downarrow\downarrow\downarrow\downarrow\downarrow\rangle$ ($m_x = -6$). Adapted from [98].

The deviation from sharp staircase-like behavior is predicted by numerical simulations (solid blue line in Fig. 17(a)) which account for the implemented experimental parameters and ramp profiles. Differences between theory and experiment are largest near the phase transitions, where excitations are easier to make due to the shrinking quantum critical gap (Fig. 16(b)).

The ground state spin configuration at each value of B_x can be extracted by looking at the probability distribution of all spin states and selecting the most prevalent state (inset of Fig. 17(a)) [78]. The magnetization of the spin states found by this method (black points in Fig. 17(a)) recover the predicted staircase structure. The steps in the experimental curve agree with the calculated phase transition locations to within experimental error (gray bands in Fig. 17(a)), which accounts for statistical uncertainty due to quantum projection noise and estimated drifts in the strengths of $J_{i,j}$, B_x , and B_y .

Fig. 17(b) shows approximately 1000 averaged camera images of the most probable spin configuration observed at each plateau in Fig. 17(a). Each box contains an ion that scatters many photons when in the state $|\uparrow\rangle$ and essentially no photons when in the state $|\downarrow\rangle$. The observed spin orderings in Fig. 17(b) match the calculated ground states at each magnetization, validating the technique of using quantum fluctuations to preferentially create these classically inaccessible ground states. (For magnetizations of 0 and -4 , two ground state orderings are observed due to the left-right symmetry of the spin-spin interactions.)

To further illustrate the necessity of using quantum fluctuations to catalyze the magnetic phase transitions, alternate ramp trajectories can be used to reach a final chosen value of B_x . Fig. 18(a) shows the ground state phase diagram of the Hamiltonian of Eq. (22), with the sharp classical phase transitions visible along the bottom axis ($B_y/J_{\max} = 0$). In addition, it shows two possible trajectories through the phase diagram that start in a paramagnetic ground state (which is easy to prepare experimentally) and end at the same value of B_x with $B_y = 0$.

The first trajectory, in which B_x is fixed and B_y is ramped from $5J_{\max}$ to 0, was the one used in Fig. 17 to experimentally verify the locations of the 3 classical phase transitions and to experimentally create the 4 different ground state phases. Along this trajectory, Fig. 18(b) plots the probability of creating each ground state as a function of B_x and find populations of $\sim 40 - 80\%$. A smooth crossover between the four ground state phases was observed, with the classical phase transitions occurring at the crossing points. This arises since distinct spin eigenstates have degenerate energies at the phase transition, causing the quantum critical gap between them to close and allowing quantum fluctuations to populate both states equally (see Fig. 16).

The second trajectory in Fig. 18(a) is purely classical, with B_y set to 0. The spins are initialized into the state $|\downarrow\downarrow\downarrow\downarrow\downarrow\downarrow\rangle$, and B_x is ramped from $5J_{\max}$ to its final value at a rate of $5J_{\max}/3$ ms. Fig. 18(c) shows that in a classical system without thermal or quantum fluctuations, the phase transitions remain undriven and the initial state $|\downarrow\downarrow\downarrow\downarrow\downarrow\downarrow\rangle$ remains dominant for all values of B_x . The ground state phases with magnetization 0 and -2 (blue and green in Fig. 18(c)) are separated from the initial state by several classical phase transitions and have essentially zero probability of being created.

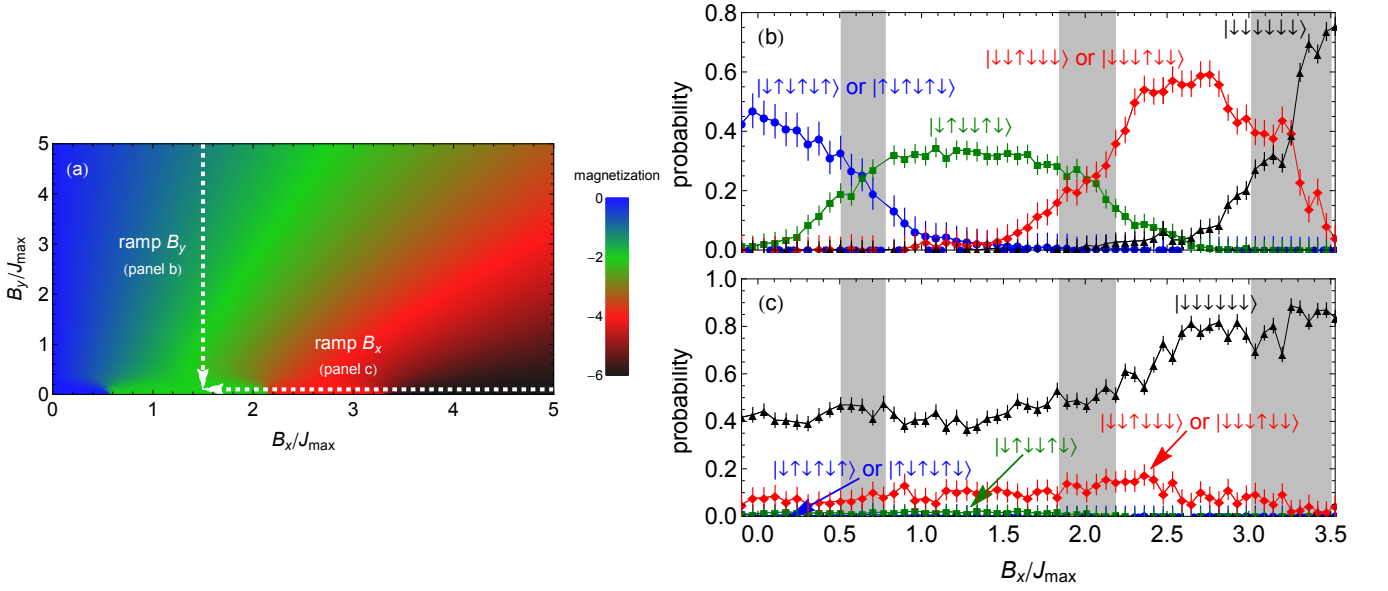


FIG. 18. (a) Ground state phase diagram of the system, along with two different trajectories that end at the same value of B_x . (b) Probabilities of the 4 different ground state spin phases when B_y is ramped in a 6-ion system. Blue dots: $|\uparrow\uparrow\uparrow\uparrow\uparrow\uparrow\rangle$ or $|\uparrow\uparrow\uparrow\downarrow\uparrow\downarrow\rangle$. Green squares: $|\downarrow\uparrow\downarrow\uparrow\downarrow\uparrow\rangle$. Red diamonds: $|\downarrow\downarrow\uparrow\uparrow\downarrow\downarrow\rangle$ or $|\downarrow\downarrow\uparrow\downarrow\uparrow\downarrow\rangle$. Black triangles: $|\downarrow\downarrow\downarrow\downarrow\downarrow\downarrow\rangle$. Gray bands are the experimental uncertainties of the phase transition locations. (c) Probabilities of creating the 4 different ground states when B_x is ramped. Most of the ground states are classically inaccessible in our zero temperature system. Adapted from [98].

5. Spin-1 simulations

As with the spin-1/2 systems described above, spin-1 systems – spanned by the basis kets $|+\rangle$, $|0\rangle$, and $|-\rangle$ – can likewise exhibit a variety of interesting new physics and ground-state phases. As a notable example, Haldane conjectured [127] that integer-spin Heisenberg chains with nearest-neighbor AFM interactions are gapped, in contrast to gapless half-integer spin chains. This energy gap in integer-spin systems corresponds to short-range exponentially decaying correlation functions, as opposed to long-range power-law decaying correlations in half-integer systems. It was later suggested [128] that this Haldane phase of the spin-one chain is governed by a hidden order, which can be characterized by a non-local string order parameter and is consistent with a full breaking of a hidden $Z_2 \times Z_2$ symmetry [129]. The Haldane phase can also be described by a doubly-degenerate entanglement spectrum [130], hinting at a topologically protected phase in one-dimension.

As theoretically proposed in both [131] and [132], a range of spin-1 Haldane physics can be accessed in traditional ion-trap quantum simulators. In [131], for instance, it is shown how to generate the full spin-1 XXZ Hamiltonian

$$H = \sum_{i,j} J_{ij} (S_x^i S_x^j + S_y^i S_y^j + \lambda S_z^i S_z^j) + D \sum_i (S_z^i)^2 \quad (23)$$

where the S_γ^i terms are the spin-1 Pauli operators on site i along the γ direction, λ is the Z -anisotropy, and D is analogous to a magnetic field B term of Eq. (3) for spin-1/2 systems. The interacting terms in Eq. (23) arise from a generalization of the Mølmer-Sørensen gate [133] to spin-1 systems, followed by a transformation to the interaction picture; the on-site D -term can be generated by imposing frequency detunings D on all the previous driving fields.

Generating the ground state of the Haldane phase can be realized by an adiabatic ramp procedure [131]. To begin, the spin-1 system can be initialized into a product state of $|0\rangle$ on each site, which is the trivial ground state when $D \gg J$. Adiabatically reducing D will then drive the system towards the Haldane phase. As the system size increases and the critical gap between the D and Haldane phase closes, a symmetry-breaking perturbation can be implemented to circumvent the phase transition. For example, adding a site-specific term $H_{\text{pert}} = -h \sum_i (-1)^i S_z^i$ will break all symmetries of the Haldane phase, allowing for a finite energy gap along the entire ramp path. The ground state can then be characterized using site-specific measurements to determine the spin correlation functions $\langle S_i^z S_j^z \rangle$ and the string-order correlation $S_{ij}^z \equiv \langle S_i^z S_j^z \prod_{i < k < j} (-1)^{S_k^z} \rangle$.

Since the interactions J_{ij} in Eq. (23) are long-ranged, this can lead to both quantitative and qualitative differences in the phase diagram as compared to the nearest-neighbor XXZ model [132]. For instance, the positions of the phase boundaries shift for long-ranged AFM interactions, whereas long-ranged FM interactions can destroy the Haldane phase and support a new continuous symmetry-broken phase. Each of these possible phases can be distinguished by comparing measured values of the

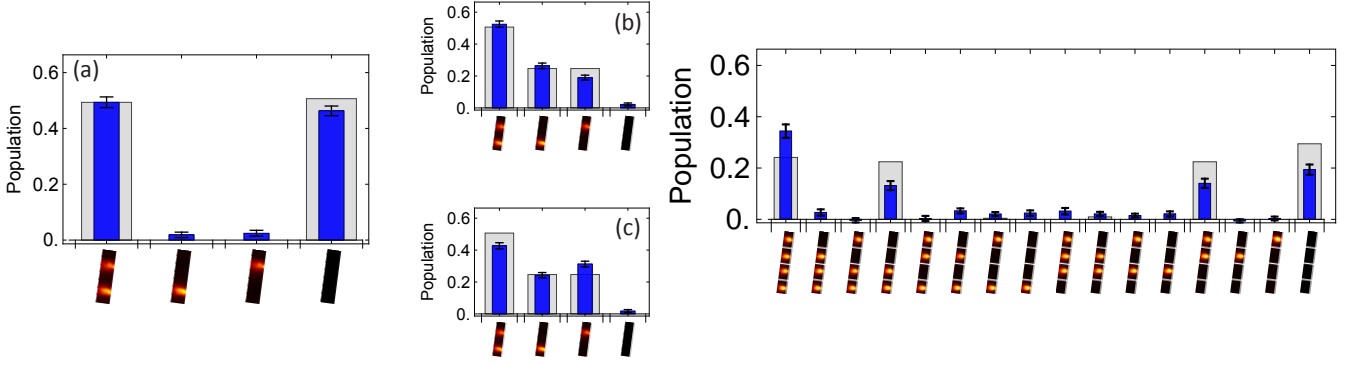


FIG. 19. Measurements of the prepared 2-spin (a-c) and 4-spin (d) states after ramping an S_z^2 field (narrow blue bars) compared to the values expected for the calculated ground state (gray bars). Panels (a), (b), and (c) show the measured populations when the ‘dark’ state is set to be $|0\rangle$, $|-\rangle$, or $|+\rangle$, respectively. The dark state is set to $|0\rangle$ in part (d). Adapted from [134].

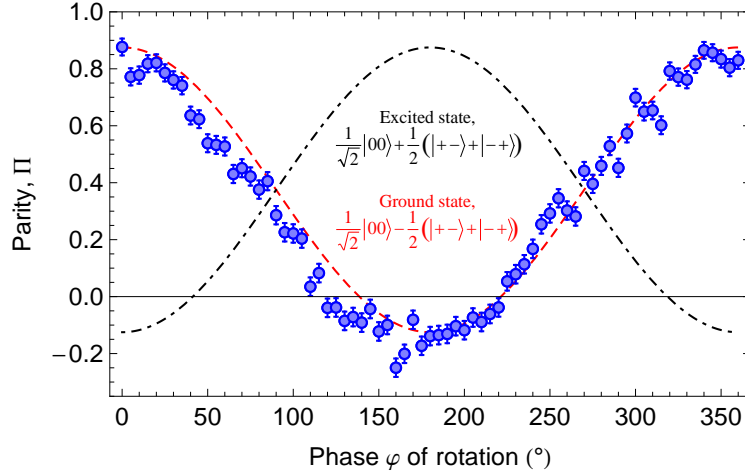


FIG. 20. Following an adiabatic ramp, the parity of the final state is measured as a function of the final rotation phase φ (see text for rotation protocol). Dashed and dot-dashed lines represent the theoretically expected values for the ground state, $|00\rangle/\sqrt{2} - (|-\rangle + |+\rangle)/2$, and highest excited state, $|00\rangle/\sqrt{2} + (|-\rangle + |+\rangle)/2$, respectively. The phase of the oscillation reveals that the relative phases in the prepared state are consistent with the expected ground state. From 134.

spin and string-order correlation functions described above.

The first experimental steps towards Haldane physics in an ion-trap quantum simulator implemented the model in Eq. (23) with $\lambda = 0$ [134]. To generate the ground states of this effective spin-1 XY model, for 2- and 4-ion spin chains, the spins were initially prepared in the state $|00\dots\rangle$. This is the approximate ground state of Eq. (23) in the presence of a large D -field. This field was then ramped down slowly until $D \approx 0$; the resulting state populations, shown in Fig. 19, match reasonably well with the exactly-calculated ground state.

Measurements of populations in the S_z basis necessarily discard phase information about components of the final state. This can be important in many spin models, including the XY model, where such measurements alone cannot discriminate between different eigenstates. For example, the ground state of an XY model with two spin-1 particles is $|00\rangle/\sqrt{2} - (|-\rangle + |+\rangle)/2$, while the highest excited state is $|00\rangle/\sqrt{2} + (|-\rangle + |+\rangle)/2$, differing only by a relative phase. In [134], verification of ground state production was accomplished by applying a pair of rotations, $R_{0-}(\pi/2, \varphi)R_{0+}(\pi/2, 0)$, and measuring the parity $\Pi = \sum_{j=0}^2 (-1)^j P_j$ (with P_j the probability of j atoms in $|0\rangle$). This is expected to result in $\Pi(\varphi) = \frac{3}{8} \pm \frac{1}{2} \cos \varphi$, where the + and - correspond to the ground and highest excited states, respectively. The data shown in Fig. 20 are consistent with having prepared the 2-spin ground state of the spin-1 XY model.

IV. NONEQUILIBRIUM PHASES OF MATTER AND DYNAMICS

In contrast to section III dealing with equilibrium properties of quantum spin models, trapped ion simulators are naturally suited for studying non-equilibrium phenomena. Non-equilibrium dynamics might even be considered more natural, since the study of equilibrium-like properties requires a specific protocol for preparing the corresponding ground or thermal state, unlike conventional condensed matter materials that are directly cooled through phonon interactions. The simplest non-equilibrium studies, on the other hand, can start with an initial product state and then simply evolve the system under a (time-dependent) Hamiltonian of interest.

Trapped ion quantum simulators provide an ideal platform for studying non-equilibrium dynamics over a broad range of both spatial and temporal resolution. The effective long-range spin-spin interactions described in section IC 2 can be modulated in time by turning on or off the laser-ion interactions. This allows non-equilibrium states to be prepared via quenches or stroboscopic application of the Ising Hamiltonian while their subsequent dynamics are observed over timescales both shorter than and longer than the natural time scale of interactions $1/J_{ij}$. These experiments retain single spin resolution even as the system size is scaled to many particles, allowing access to non-trivial observables such as spin-spin correlations and magnetic domain sizes. Since strongly interacting and highly-frustrated Ising spin models are often employed in analytical and numerical studies of non-equilibrium quantum dynamics, the results of trapped ion spin simulations serve as an important benchmark for these theoretical predictions.

Perhaps the most natural non-equilibrium experiments are global and local quenches. In a global quench experiment, a simple initial state evolves under a time-independent Hamiltonian. A global quench originates from situations where the simple initial state can be naturally thought of as the ground state of some simple Hamiltonian, in which case the dynamics ensues when the Hamiltonian is changed (quenched). A local quench allows the comparison of the non-equilibrium dynamics between two initial states that differ by the application of a locally applied unitary. A particular example of a local quench is a situation where one of the two initial states is an eigenstate of the Hamiltonian.

In the case of local and global quenches, short-time or long-time dynamics may be of interest. In the case of short-time dynamics, discussed in Sec. IV A, one is typically interested in time scales over which quantum information can propagate across the system. In the case of long-time dynamics, one is interested in whether the system eventually approaches some effective steady state and, if so, how this steady-state is approached. While one often expects the system to effectively thermalize (where part of the system uses its complement as the bath [135]), we will discuss in Sec. IV B that disorder can often prevent such thermalization leading to so-called many-body localization. Similarly, in Sec. IV C, we will show that, even in cases where the system eventually thermalizes, it is possible that this thermalization takes a very long-time to occur and is preceded by so-called prethermalization.

There are many forms of inducing and probing spin dynamics in trapped ion systems. One example is the periodic modulation of a Hamiltonian, which gives rise to stroboscopic Floquet dynamics. In Sec. IV D, we will discuss such dynamics in trapped ion systems in two complementary contexts. The first will focus on the application of a Hamiltonian and its negative counterpart in order to measure so-called out-of-time-ordered correlation (OTOC) functions. The second will focus on the spontaneous breaking of discrete time translation symmetry, leading to the emergence of time crystalline order.

A. Information Propagation

For intermediate-length ion chains, we assume that the interactions fall off with distance as a power-law $J_0/|i-j|^\alpha$ between ions i and j , with $0 \leq \alpha \leq 3$, as derived in Eq. (13). In this case, the spin Hamiltonian has the general form:

$$H = \sum_{i < j} h_{ij}(t) + \sum_i h_i(t), \quad (24)$$

where $h_i(t)$ is a Hamiltonian acting on spin i and where the two-spin Hamiltonian $h_{ij}(t)$ acting on spins i and j is subject to the bound

$$\|h_{ij}(t)\| \leq \frac{J_0}{|i-j|^\alpha}. \quad (25)$$

Here $\|O\|$ indicates the operator (or spectral) norm of operator O , that is the magnitude of its eigenvalue with largest absolute value.

Consider the following local-quench experiment. Let B be a unitary operator acting on a single site, while A is a single-site observable acting on another site a distance r away. Let $|\psi\rangle$ be an arbitrary initial state, and let $A(t)$ be the Heisenberg evolution

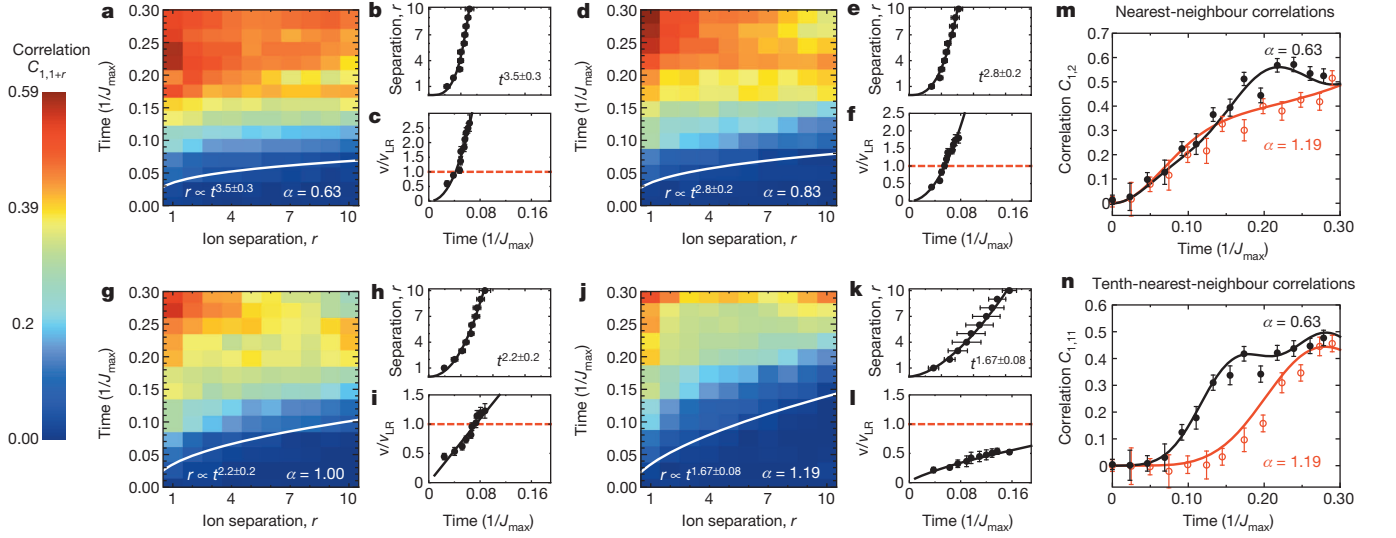


FIG. 21. (a-c) Spatial and time-dependent correlations (a), extracted light-cone boundary (chosen as the contour $C_{i,j} = 0.04$) (b) and correlation propagation velocity (c) following a global quench of a long-range XY model with $\alpha = 0.63$. The curvature of the boundary shows an increasing propagation velocity (b), quickly exceeding the short-range Lieb-Robinson velocity bound, v_{LR} (c). Solid lines give a power-law fit to the data, which slightly depends on the choice of contour $C_{i,j}$. (d-l), Complementary plots for $\alpha = 0.83$ (d-f), $\alpha = 1.00$ (g-i) and $\alpha = 1.19$ (j-l). As the range of the interactions decreases, correlations do not propagate as quickly through the chain. For the shortest-range interaction (j-l), the experiment demonstrates a faster-than-linear growth of the light-cone boundary, despite having $\alpha > 1$. (m,n) Measured nearest-neighbor and tenth-nearest-neighbor correlations closely match the numerical solution found by evolving the Schrödinger equation of an XY model with no free parameters and no decoherence. Error bars, 1 s.d. Adapted from 178.

of A under the Hamiltonian H in Eq. (24). Then the effect on observable A due to the disturbance B can be defined as the difference between the expectation values of $A(t)$ in the original state $|\psi\rangle$ and in the quenched state $B|\psi\rangle$:

$$|\langle \psi | B^\dagger A(t) B | \psi \rangle - \langle \psi | A(t) | \psi \rangle| = |\langle \psi | B^\dagger [A(t), B] | \psi \rangle| \leq \|[A(t), B]\|. \quad (26)$$

We see, therefore, that the signal after time t a distance r away is bounded by the unequal-time commutator $\|[A(t), B]\|$. In turn, upper bounds on $\|[A(t), B]\|$ subject to the Hamiltonian in Eqs. (24,25) are referred to as Lieb-Robinson (or Lieb-Robinson-type) bounds, named after the original work considering nearest-neighbor interactions ($\alpha = \infty$) [136]. The region in the r - t plane outside of which $\|[A(t), B]\|$ must be small is called the causal region, while the boundary of the causal region is called the light cone (or the effective light cone). A growing body of theoretical literature exists placing upper bounds on $\|[A(t), B]\|$ and therefore deriving tighter and tighter light cones for different values of α [137–149]. At the same time, a complementary growing body of theoretical literature considers specific Hamiltonians and protocols demonstrating larger and larger causal regions [139, 141, 145, 150–174]. While these upper and lower bounds on information propagation are starting to approach each other, there is still no provably tight light cone shape other than at large α , where the light cone is strictly linear [148, 149].

The light-cone-like spreading of correlations with nearest-neighbor interactions following a global quench was first measured in neutral atoms confined in an optical lattice [175]. For long-range interacting systems such as trapped ion spins, the spread of correlations is more subtle. To see this, suppose the system starts in an initial product state $|\psi\rangle$ and evolves under the Hamiltonian in Eqs. (24,25). At time $t = 0$, the connected correlation function $C_{i,j}(t) = \langle O_i(t) O_j(t) \rangle - \langle O_i(t) \rangle \langle O_j(t) \rangle$ (where operator O_i acts on site i) vanishes since the first expectation value factorizes. As time goes on, $C_{i,j}(t)$ grows. For the case of short-range interactions, $C_{i,j}(t)$ is bounded in the r - t plane (where $r = |i - j|$) by a linear light cone similar to the corresponding light cone for the unequal time commutator $\|[A(t), B]\|$ [176]. For general α , a bound on $\|[A(t), B]\|$ can also be used to derive a bound on $C_{i,j}(t)$ [177], but the relationship between the two light cones is not as trivial as in the nearest-neighbor ($\alpha = \infty$) case.

The spread of correlations in a long-range interacting system subject to a global quench was measured in a chain of ions subject to long range interactions [178]. This experiment studied the XY model (albeit in a different basis) corresponding to $h_i(t) = 0$ and $h_{ij}(t) \propto (\sigma_i^x \sigma_j^x + \sigma_i^z \sigma_j^z) / |i - j|^\alpha$ in Eq. (24). Fig. 21 shows data on 10 ions following a global quench [178]. Starting with an initial state of all spins pointing down (in the z basis), the experiment measures the time evolution of connected correlations $C_{i,j}(t) = \langle \sigma_i^z(t) \sigma_j^z(t) \rangle - \langle \sigma_i^z(t) \rangle \langle \sigma_j^z(t) \rangle$. The growth of connected correlations following a global quench may also be accompanied by the growth of entanglement, as was observed experimentally in [179].

A local quench experiment on trapped-ion chains studied the XY model of hopping hard-core bosons corresponding to $h_i(t) = 0$ and $h_{ij}(t) \propto (\sigma_i^+ \sigma_j^- + \sigma_i^- \sigma_j^+) / |i - j|^\alpha$ in Eq. (24) [85]. Fig. 22 shows on a local quench on 15 spins from the experiment.

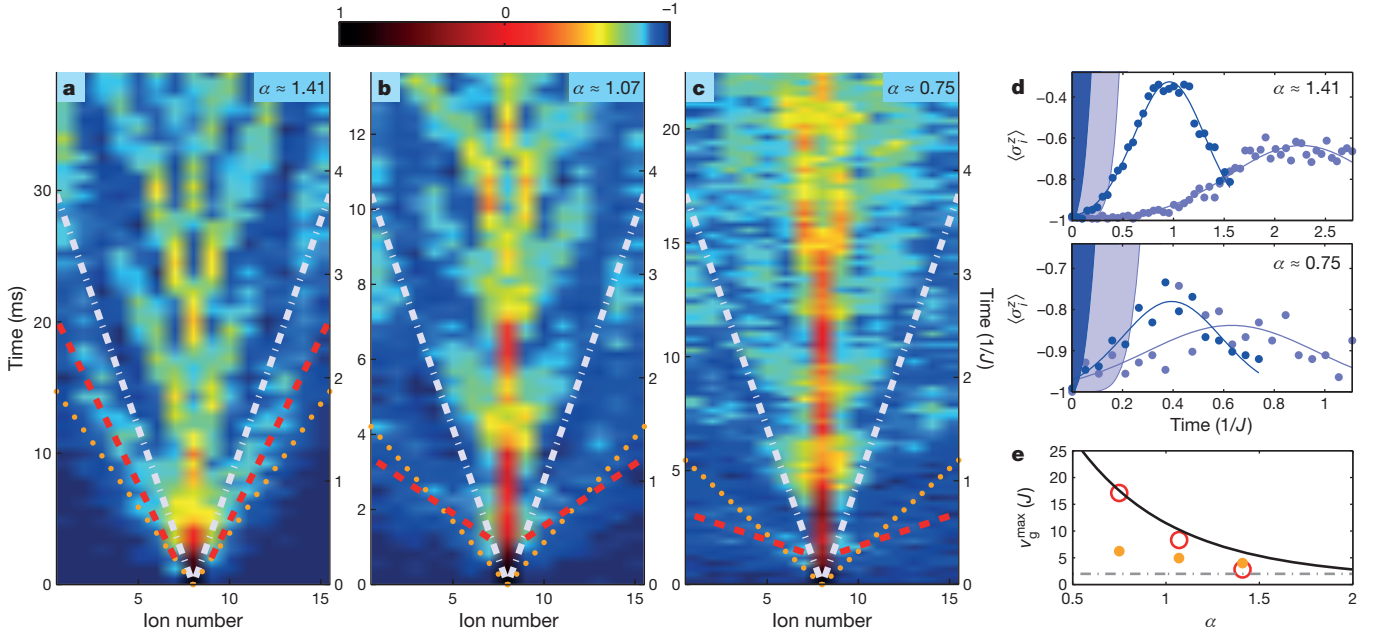


FIG. 22. (a-c) Measured magnetization $\langle \sigma_i^z(t) \rangle$ (color coded) following a local quench. From a to c, the interaction ranges are $\alpha \approx 1.41, 1.07, 0.75$. In a, an effective light cone is evident and the dynamics are approximately described by nearest-neighbor interactions only. Red lines, fits to the observed magnon arrival times [examples in (d)]; white lines, light cone for averaged nearest-neighbor interactions; orange dots, after renormalization by the algebraic tail. As the interaction range is increased (b,c) the light cone disappears and nearest-neighbor models fail to capture the dynamics. d, Magnetization of spins (ions) 6 and 13, from (a) (top) and (c) (bottom). Solid lines, Gaussian fits to measured magnon arrival. Top: for $\alpha = 1.41$, a nearest-neighbor Lieb-Robinson bound captures most of the signal (shaded region). Bottom: for $\alpha = 0.75$, it does not. (e) Maximum group velocity. With increasing α , the measured magnon arrival velocities (red circles) approach the group velocity of the non-renormalized nearest-neighbor model (grey dash-dotted line). If renormalized by the algebraic tail, the nearest-neighbor group velocity increases at small α (orange dots), but much less than the increase of the observed magnon velocity. For small α , the measured arrival times are consistent with the divergent behaviour predicted for full power-law interactions (black line). Adapted from 85.

After flipping up the middle spin (corresponding to $B = \sigma_8^x$) in a chain of down spins, the experiment measures $A = \sigma_i^z$ for various i . Since the number of flipped spins is conserved during the time evolution, the evolution is well-described using the language of single-flip eigenstates called magnons.

Experiments on ultracold polar molecules [180] and defect centers in solid state [181] do not yet have the single-spin resolution necessary for studying the shape of the causal region after local or global quenches in long-range-interacting systems. On the other hand, experiments on ultracold neutral atoms interacting via Rydberg-Rydberg interactions [182–185] should be able to access the particularly interesting parameter regime of $\alpha = 3$ (dipolar interactions) [186] in one, two, and three spatial dimensions.

B. Many-body Localization

Many-body localization (MBL) has become one of the most studied nonequilibrium phases of matter, receiving considerable scrutiny in both experiment and theory in the past decade [187–191]. The localization effect is a generalization of single-particle “Anderson” localization, which is characterized by a cessation of quasiparticle transport in non-interacting systems subject to a random potential landscape [192]. Surprisingly, in the case of MBL similar insulator-like properties are observed even when particles are strongly interacting [187–189]. When prepared with a quench, the quantum states become highly entangled many-body superpositions of excited eigenstates spanning the entire energy spectrum of the disordered system Hamiltonian. MBL can be distinguished from Anderson localization by the logarithmic growth of entanglement entropy at long-times [193]. The distribution of eigenstates occupied in an MBL phase is decidedly non-thermal and a number of observables have been identified to characterize phase transitions between MBL and thermal states when varying the interaction strength or disorder in the Hamiltonian [188, 189, 194, 195].

Signatures of MBL have been observed in a trapped ion quantum simulator in [196, 197] by engineering a locally disordered but programmable potential (H_D), which is applied simultaneously with the effective long range interacting transverse field

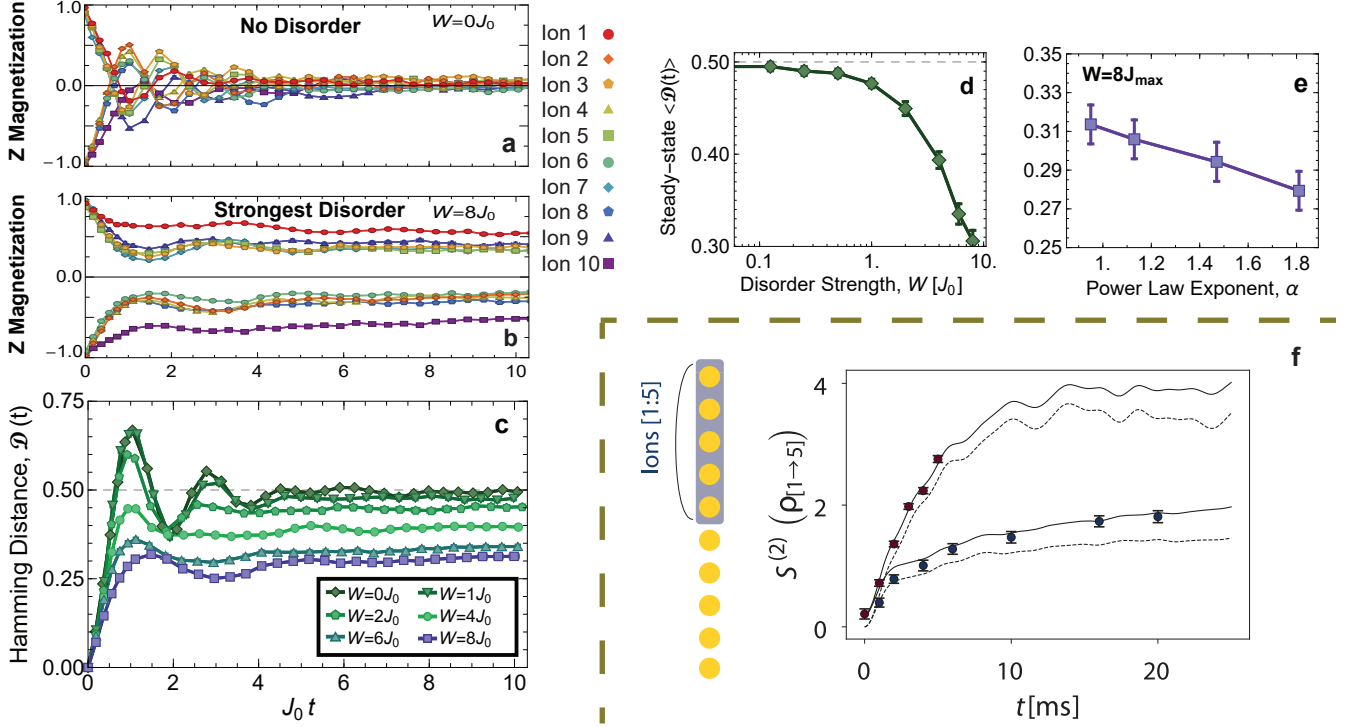


FIG. 23. **Many-Body Localization:** (a, b) Temporal dynamics for each of the 10 ion's Z magnetization $\langle \sigma_i^z(t) \rangle$ in the case of zero disorder and strong disorder for panels (a) and (b) respectively. (c) The normalized Hamming distance $\mathcal{D}(t)$ has plateaued to a steady state value for $J_0 t \geq 5$ at all measured disorder strengths. (d) The time averaged steady state value $\langle \mathcal{D}(t) \rangle$ after the plateau shows the onset of a crossover between a thermalizing regime ($\langle \mathcal{D}(t) \rangle = 0.5$) and localizing regime ($\langle \mathcal{D}(t) \rangle = 0$) as disorder increases. (e) The steady state Hamming distance increases with longer range interactions. (f) The half-chain entropy growth in the absence of disorder (red points) and for a disordered chain with $W = 6J_0$ (blue points), compared with numerical simulations of unitary dynamics (dotted lines) and including known sources of decoherence (solid lines). Panels (a-e) are adapted from [196], and panel (f) is adapted from [197].

Hamiltonian (H_{int}) as described in section IC

$$H_{MBL} = H_{int} + H_D. \quad (27)$$

The disordered potential is implemented with single site resolution across the ion chain such that

$$H_D = \sum_i D_i \sigma_i^z. \quad (28)$$

where D_i is sampled from a uniform distribution, $D_i \in [-W/2, W/2]$, with width W . For finite system sizes, this Hamiltonian exhibits features consistent with many-body localization and demonstrates a disorder-induced, long-lived memory of the system's initial conditions [198, 199]. Understanding the thermodynamic stability of localization with power-law interactions remains an intriguing open question [200–203].

The MBL state is created by initially preparing the 10 spin Néel state with staggered order ($|\psi_0\rangle = |\downarrow\uparrow\downarrow\uparrow\downarrow\uparrow\downarrow\uparrow\downarrow\uparrow\rangle_z$) which is highly excited with respect to the disordered Ising Hamiltonian of Eq. 27. This Hamiltonian is rapidly quenched on and the resulting single spin magnetization dynamics $\langle \sigma_i^z(t) \rangle$ are measured for times up to $t = 10/J_0$. The experiment is repeated under multiple instances of disorder with Stark-shifts (D_i) applied programmatically to each ion using a rastered individual addressing laser [51]. This individual addressing laser is also used create the initial Néel state using a sequence of controlled spin-flips.

In the absence of disorder these initial spin states will thermalize if the uniform transverse field B is sufficiently large [204–206]. In [196], global rotations are used to prepare eigenstates of both σ^x and σ^z and measure the resulting single ion magnetization projected into those directions after evolution under H_{MBL} . In the case of a thermalizing system, memory of the initial spin configuration will be lost in all directions of the Bloch sphere, namely $\langle \sigma_i^x \rangle = \langle \sigma_i^z \rangle = 0$ at long times. Above the threshold transverse field ($B \gtrsim 4J_0$) the system rapidly thermalizes to zero magnetization after relatively short timescales ($t < 5/J_0$) (Figure 23a).

However, with the transverse field held fixed at $B = 4J_0$, the data clearly shows that applied disorder localizes the spin chain, retaining memory of the initial Néel state in measurements of the z magnetization $\langle \sigma_i^z \rangle$ (Figure 23b). Each measurement of magnetization dynamics for disorder width W is repeated with at least 30 different realizations of disorder, which are subsequently averaged together. This is sufficient to reduce the finite depth disorder sampling error to be of the same order as other noise sources. After some initial decay and oscillations, the magnetization of each spin settles to a steady state value for $J_0 t \geq 5$. The degree of localization can be quantified using the normalized Hamming distance (HD)

$$\begin{aligned} \mathcal{D}(t) &= \frac{1}{2} - \frac{1}{2N} \sum_i \langle \sigma_i^z(t) \sigma_i^z(0) \rangle \\ &= \frac{1}{2} - \frac{1}{2N} \sum_i (-1)^i \langle \sigma_i^z(t) \rangle. \end{aligned} \quad (29)$$

This observable counts the number of spin flips from the initial state, normalized to the length of the spin chain. At long times, a randomly oriented thermal state shows $\mathcal{D} = 0.5$ while one that remains fully localized has $\mathcal{D} = 0$ (Figure 23c).

The average steady state value $\langle \mathcal{D}(t) \rangle$ for $J_0 t \geq 5$ can serve as an order parameter to display the crossover between the localizing and thermalizing regimes. The most relevant adjustable experimental control parameters for probing the MBL phase diagram are the amplitude of disorder W and the interaction range α . Increasing W pins each spin closer to its initial state and pushes the entire spin chain towards a localized regime (Figure 23d). Likewise, the localization strengthens as α is increased towards shorter range interactions (Figure 23e), recovering Anderson localization via a Jordan-Wigner transformation in the $\alpha \rightarrow \infty$ limit. Numerical studies have confirmed that full localization occurs within experimentally accessible disorder strengths and interaction ranges [207].

Interestingly, Anderson localization can be realized with the same long-range disordered Hamiltonian by observing the dynamics of a single spin excitation in the ion chain. For example, in [208] the transport efficiency of a spin excitation from initial site $i = 3$ to the target site $i = 8$ is observed as a function of time in a 10-ion spin chain. The transport is reduced with strongly applied disorder which is indicative of localization of the spin excitation. However, adding temporal variations in the form of dephasing noise destroys the localization, a phenomenon known as environment-assisted quantum transport. Section IV D further explores experiments studying trapped ion spin dynamics under the influence of time-varying Hamiltonians.

The slow growth of entanglement entropy (S) has long been understood as a distinguishing feature of localization [193]. A short range interacting MBL state should exhibit a slower entanglement growth rate than interacting quantum states without disorder, where entanglement spreads ballistically. The dynamics of the entanglement entropy are also quite different for non-interacting Anderson localized systems, where the entanglement saturates at short times once the system's dynamics have reached the localization length [189]. In a trapped ion quantum simulator with algebraically decaying interactions the entanglement entropy of an MBL state should also grow algebraically, $S \sim t^q$, but with $q < 1$ the dynamics are still distinct from those of non-localized or Anderson localized systems [209].

It is generally difficult to measure entanglement entropy in quantum simulators due to the exponential system-size scaling of the number of measurements required for full state tomography. In [196] the observed slow growth in quantum-fisher information (QFI) is used as a proxy for half-chain entanglement entropy, motivated by a similar scaling with disorder and interaction strength as observed in numerical simulations. A more direct measurement is made in [197], where they develop a technique to probe the second-order half-chain Rényi entanglement entropy in their 10 ion quantum simulator ($S^{(2)}(\rho_{[1 \rightarrow 5]})$) using randomized measurements. They find the entanglement growth to be significantly suppressed in the presence of strong disorder, in good agreement with numerical predictions (Figure 23f).

Many-body localization is a unique case in which a closed quantum system remains non-ergodic and localized even up to infinite times. The trapped ion quantum simulations of [196, 197] are limited by finite experimental coherence times to only one decade in $J_0 t$. This makes it difficult for these experiments to quantify how long-lived the magnetization or slow the entanglement growth might be. Fortunately, other experiments that have studied MBL using cold neutral atoms can achieve several orders of magnitude longer evolution time relative to their interaction timescale. For example, MBL can be realized using cold fermions in quasi-random 1D optical lattices [190, 210–212], verifying MBL-like behavior in a variety of Hubbard Hamiltonians. This system has also been used to confirm the breakdown of MBL in open quantum systems [213, 214]. Moreover, experiments have started to probe whether MBL can exist in systems with dimensionality > 1 [191, 215, 216], where the stability of MBL is still an open question [217]. Other experimental platforms have used novel metrics to probe many-body localization, including many-body spectroscopy [218], measuring out-of-time order correlators [219], and performing full state tomography to compute entanglement entropy [220].

C. Prethermalization

Hamiltonians that support MBL are believed to be non-ergodic, even after evolution times exponentially long in system size [188]. There are also systems that are non-ergodic for a shorter amount of time (but often still much longer than the coherence time of typical quantum simulation experiments) before eventually thermalizing. Usually, these systems are not disordered and can be described by models of weakly interacting (quasi-)particles, such as 1D Bose gases [221–223]. The generic behavior of such a system is called prethermalization, meaning that the system relaxes to a quasi-stationary state different from thermal state before thermalizing eventually. The prethermal quasi-stationary state is usually believed to be described by a generalized Gibbs ensemble (GGE) [224] that corresponds to the model of quasi-particles without the weak interactions. Such state will have a partial memory of the initial state, because the quasi-particle occupation numbers are conserved if interactions are ignored. At sufficiently long time, the weak interactions are expected to break integrability of system and lead to thermalization in the end. This picture of prethermalization has been well studied both in theory [225–227] and experiment [222, 223].

In a programmable ion-trap quantum simulator, due to long-range spin interactions, new types of prethermalization can occur with prethermal states not described by a standard GGE. An example study was first proposed theoretically [228] and later demonstrated experimentally [229]. The central idea is that with sufficiently long ranged interactions, a non-disordered and homogenous system can have a strong emergent inhomogeneity due to the open boundary condition of an experimental spin chain. This emergent inhomogeneity can lead to trapping of quasi-particles before the system relaxes to GGE. As both kinetic energy and weak interactions can delocalize trapped quasi-particles, the dynamics of the system can reveal a rich interplay between quantum tunneling and interaction effects, leading to new types of relaxation beyond conventional prethermalization.

The model under study in Refs. [228, 229] is the same transverse field Ising model described by Eq. (15). With long-range interactions, H_{TI} is generally nonintegrable (in contrast to the nearest-neighbor case where the 1D model is integrable through a Jordan-Wigner transformation [60]), and thermalization is anticipated in the long-time limit according to the eigenstate thermalization hypothesis [206]. To better understand the dynamics of H , we can map each spin excitation along the z direction into a bosonic particle to turn Eq. (15) into a bosonic model with two parts: An integrable part made from noninteracting spin-wave bosons that can be used to construct a GGE, and an integrability-breaking part consisting of interactions among the spin-wave bosons, which is responsible for the thermalization [229]. When the initial state has a low spin/ bosonic excitation density and the magnetic field is much larger than the average J_{ij} , the bosonic excitation density will remain low during the dynamics and the interactions among the bosons will stay weak.

The experiment in Ref. [229] begins by preparing a single spin excitation on either edge of a 7-ion chain $|\psi_R\rangle = |\downarrow\downarrow\downarrow\downarrow\downarrow\downarrow\uparrow\rangle_z$ or $|\psi_L\rangle = |\uparrow\downarrow\downarrow\downarrow\downarrow\downarrow\rangle_z$. The spins then evolve under Eq. (15) and the time evolution of the spin projection in the z -basis is measured. The magnetic field B is at least an order of magnitude larger than J_0 in the experiment so the number of spin excitations along the z direction is approximately conserved in the short time dynamics where the system can be regarded as a single spin excitation. But in the long time dynamics, multiple spin excitations will be created and interacting with each other.

To characterize the dynamics of the spin excitations, we introduce a single observable that measures the relative location of the spin excitation in the chain

$$C = \sum_{i=1}^N \left(\frac{2i - N - 1}{N - 1} \right) \left(\frac{\sigma_i^z + 1}{2} \right), \quad (30)$$

where N is the number of ions. The expectation value of C varies between -1 and 1 for a spin excitation on the left and right ends, respectively. The choice of initial states ensures that the initial value of $\langle C \rangle$ is either 1 or -1. Due to the spatial inversion symmetry of the underlying Hamiltonian in Eq. (15), both the GGE and thermal values of $\langle C \rangle$ should be zero.

In Fig. 24(c-d) the value of $\langle C \rangle$ along with its cumulative time average $\langle \bar{C} \rangle$ are shown for the two initial states with a single spin flips on either end of the spin chain. In the short-range interacting case ($\alpha = 1.33$), where the system rapidly evolves to a prethermal state predicted by the GGE associated (with $\langle C \rangle = 0$) with the integrals of motion corresponding to the momentum space distribution of the single particle representing the spin excitation. The memory of the initial spin excitation location is thus not preserved. However, in the long-range interacting case ($\alpha = 0.55$), the position of the spin excitation reaches a quasi-stationary value that retains a memory of the initial state out to the longest experimentally achievable time of $25/J_{\max}$. This prethermal state is in obvious disagreement with both a thermal state and the GGE prediction, which both maintain the right-left symmetry of the system.

For evolution time not long enough to generate appreciably more than one spin flips, the dynamics of the Hamiltonian in Eq. (15) for the initial states are similar to those of a free-particle in a potential, with the location of the particle representing that of the single spin excitation. For short-range spin interactions, the shape of the potential is approximately given by a square well, due to the open boundary condition and no explicit spatial inhomogeneity of the interactions. However, as we increase the range of spin-spin interactions, the shape of the potential will get distorted from a square well to a double well shaped potential,

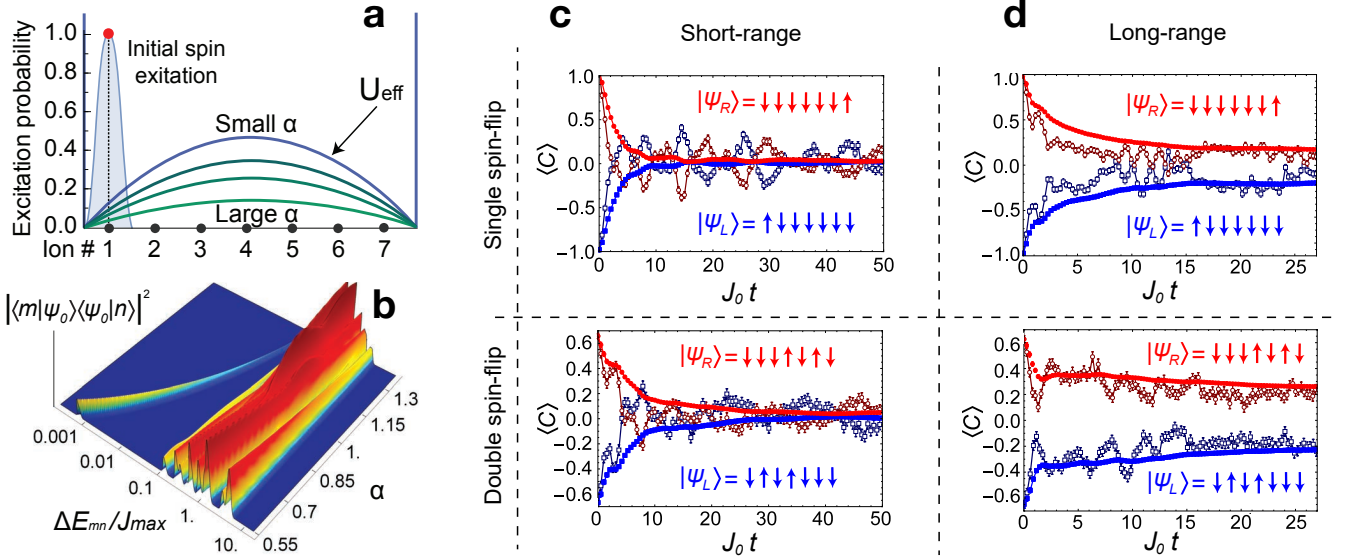


FIG. 24. Prethermalization. (a) An initial spin excitation is prepared on one side of a 7 ion chain subject to open boundary conditions and long-range XY interactions. As the range increases (α decreases) the excitation is subject to an emergent potential barrier. (b) In the case of short range interactions, either one or two spin flips delocalize to $\langle C \rangle \approx 0$, consistent with the GGE. (c) For long-range interactions memory of initial conditions is preserved in a long-lived prethermal state. In both (b) and (c), the open squared/circles plot $\langle C \rangle$ for initial states prepared on the left/right side of the spin chain, while the filled circles/squares plot the cumulative time average $\langle \bar{C} \rangle$ for this data. Adapted from 229.

as shown in Fig. 24(a). For a single particle on a lattice with a double well potential, there will be an extensive number of near-degenerate eigenstates that are symmetric and antisymmetric superpositions of wavefunctions in the left and right potential wells. For seven lattice sites, the energy difference between all pairs of energy eigenstates as a function of α is shown in Fig. 24(b), together with the overlap of eigenstates with the initial state. One sees that with $\alpha = 0.55$ the two lowest energy states are almost degenerate, with an energy difference of approximately one-thousand times smaller than J_{max} , due to the tunneling rate between the two double well, which is exponentially small in the barrier height. As a result the spin excitation will remain in its initial well until it tunnels across the potential barrier at much longer times.

To go beyond the single particle picture above, the experiment in [229] prepares initial states with two spin excitations. In this case, there will be weak interactions between the two particles that represent the spin excitations, similar to the scenario for many-body localization [196]. Despite the presence of weak interactions, similar prethermal states were found, as shown in the bottom panel of Fig. 24(c-d): Relaxation to GGE is found for shorter-range interactions ($\alpha = 1.3$) while for longer-range interactions the system clearly does not relax to GGE. Similar results were also found in a chain of 22 ions, as shown in Fig. 25 [229]. The persistence of the same prethermalization observed with more than a single spin excitation is attributed by the existence of extensive number of nearly degenerate eigenstates for the single particle spectrum in the double well shown in Fig. 25(a). Thus an extensive number of spin excitations near one end of the chain will still be localized by the double well before tunneling happens at a later time.

An interesting interplay of single-particle tunneling in the effective double well with particle-particle interactions always exists for this experiment, as even if one starts with a single spin excitation state, the finite transverse field in Eq. (15) will create more spin excitations over time. The effect of interactions will thermalize the system, while the effect of tunneling will bring the system to the GGE. Thus, depending on the range of spin-spin interactions, it is thus possible to either observe the prethermalization to GGE after the prethermalization caused by the trapping in double well potential, or observe thermalization directly after the observed prethermalization. Finding out which scenario the system falls in would require a much longer coherence time for the experiment. While improving the experimental coherence time is challenging, one should be aware that simulating the long-time dynamics of a non-integrable, long-range interacting spin chain is equally, or even more challenging on a classical computer.

It should be emphasized that the emergence of an effective double-well potential for the spin excitations is a phenomenon unique to an open spin chain with strongly long-range interactions. A spin chain with periodic boundary condition and without spatial inhomogeneity is fully translationally invariant, and translational invariance is not expected to be broken in the long time behavior of the system. It is counter-intuitive, but true, that changing boundary conditions of a long-range interacting system can impact its bulk properties significantly. The observed prethermalization is thus a manifestation of the plethora of new physics

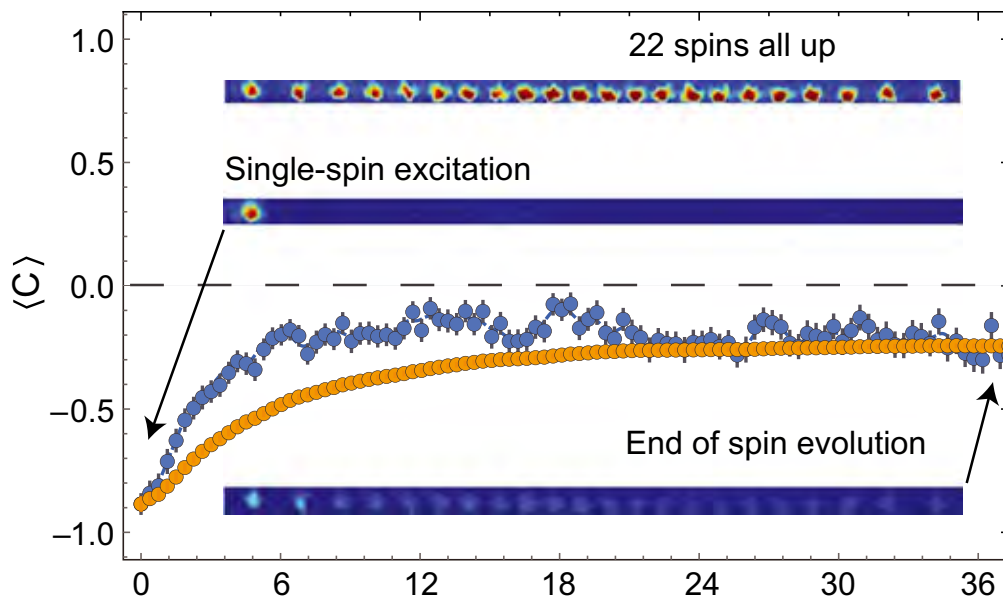


FIG. 25. Time evolution (light blue) and cumulative time average (orange) of the averaged center of excitation $\langle C \rangle$ in a 22-ion chain. The ion spins are initialized with a single spin excitation on the left end (middle image). After evolving in the XY spin Hamiltonian for time $t = 36/J_0$, where J_0 is the nearest-neighbor coupling, the spin excitation is delocalized, but its average position remains stuck on the left half of the chain (bottom image), the signature of prethermalization. Effective range of the interaction is $\alpha \approx 0.9$. Adapted from 229.

programmable quantum simulators can achieve, i.e. going beyond paradigms in models that exist in a standard, condensed matter scenario, as also demonstrated by other experiments mentioned in Sec.IV.

D. Stroboscopic Dynamics and Floquet Phases of Matter

In section IV B, we focused on static (time-independent) Hamiltonians whose non-equilibrium nature arises from the presence of quenched disorder leading to many-body localization; such localization prevents the system's internal dynamics from thermalizing and leads to certain memory of local initial conditions [188, 189]. An alternate setting for exploring non-equilibrium phases is to begin with a time-dependent Hamiltonian whose equations of motion are intrinsically dynamical. Recently, a tremendous amount of theoretical and experimental work has been devoted to exploring the mildest case of such time-dependence, where the system is governed by a periodic Hamiltonian where $H(t + T) = H(t)$; such Floquet systems [231–233] are particularly ideal from the perspective of quantum simulation [234]. In the case of trapped ions, as we have previously discussed in section II, there exists a natural capability to stroboscopically apply different microscopic Hamiltonians, making this platform an ideal Floquet quantum simulator. In this subsection, we will focus on two specific examples where a programmable ion simulator was operated in this modality.

First, we will describe the implementation of a novel class of measurements termed out-of-time-ordered correlation functions (OTOCs) [235, 236]. Such correlators have recently been proposed as powerful diagnostics of quantum chaos and their dynamical behavior remains the subject of intense interest [237, 238]; indeed, the possibility of defining a quantum Lyapunov exponent based on the exponential growth of OTOCs in certain systems has led to a conjectured bound on the rate of thermalization in many-body quantum systems [236]. The functional form of the OTOC is quite different from conventional autocorrelation functions, $F(\tau) = W^\dagger(\tau)V(0)W(\tau)V(0)$, and requires an intermediate step of time-reversal. This represents the major challenge from an experimental implementation perspective [230, 239]. In the case of ions, it is possible to skirt this challenge by leveraging the ability to stroboscopically apply (in certain cases) both the Hamiltonian and its negative counterpart. This was experimentally demonstrated in [230] by using a two-dimensional array of laser-cooled $^9\text{Be}^+$ ions in a Penning trap. The effective spin degree of freedom corresponds to the valence electron spin states of the beryllium ion. Strong Ising interactions between these spins are engineered through a time-dependent optical dipole force, which couples the spins to the axial motional modes of the ion crystal. Integrating out the motional modes leads to an all-to-all coupled spin Hamiltonian, $H = (J/N) \sum_{i < j} \sigma_i^z \sigma_j^z$, where J characterizes the interaction strength and N is the number of ions. While such an all-to-all interacting Ising model

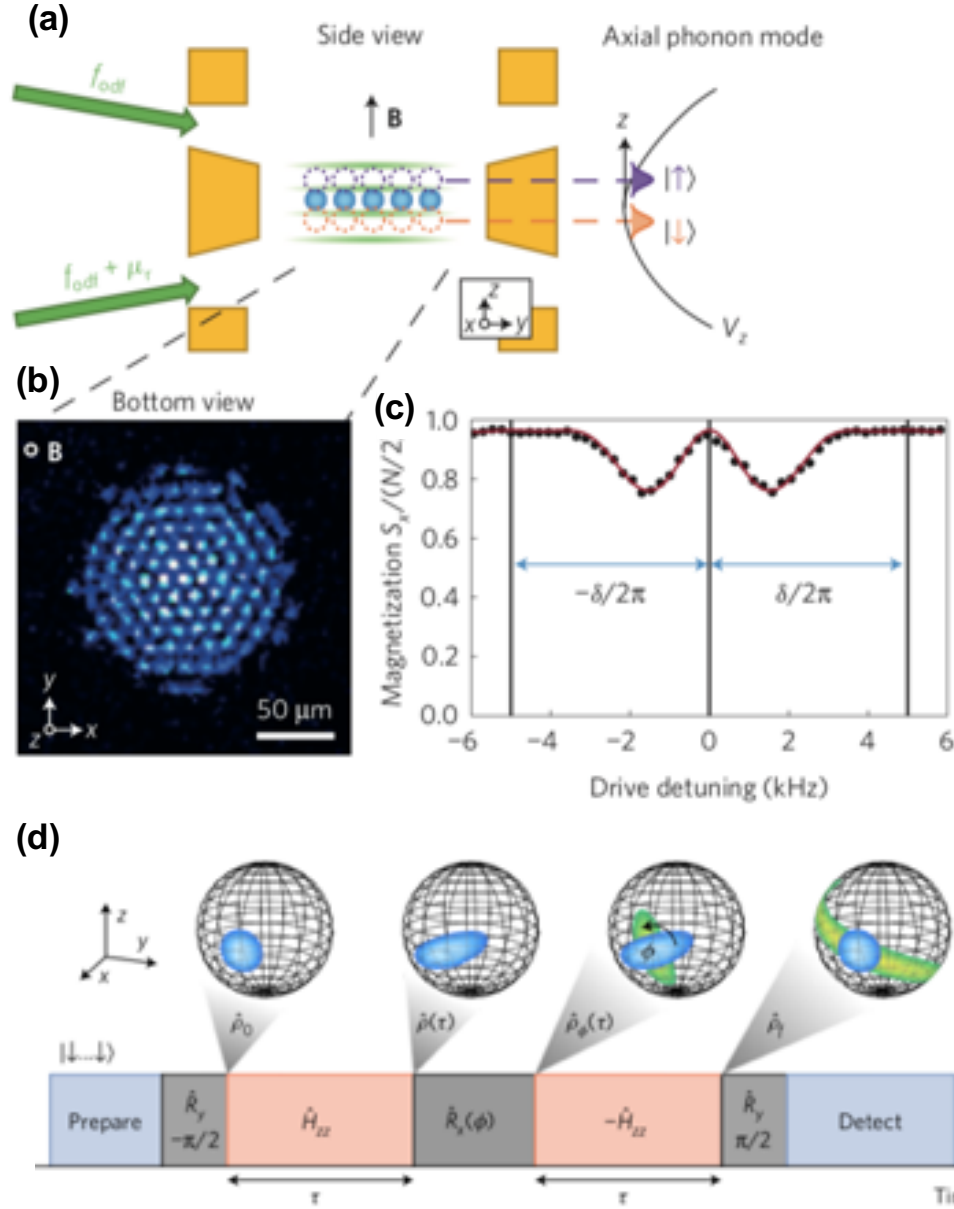


FIG. 26. Out-of-time-order-correlators (OTOC) in a 2D ion simulator. (a) Schematic depicting a Penning trap cross-section. Ions (blue circles) are confined axially to a single 2D plane with static electric fields from potentials on the electrodes (gold). Rotation of the ions in the axial magnetic field B produces radial confinement from the Lorentz force. A pair of detuned optical dipole force beams (green) interfere and form a travelling wave optical lattice, producing spin-dependent center-of-mass mode excitations that couple the spins to the axial phonon mode. (b) Image of 2D array of ${}^9\text{Be}^+$ ions. (c) Demonstration of the ability to tune the interactions by using the detuning of the optical dipole force beam. A $+\delta$ detuning gives rise to an anti-ferromagnetic interaction, while a $-\delta$ detuning gives rise to a ferromagnetic interaction. (d) Shows the experimental sequence used to measure an out-of-time-ordered correlation function. Adapted from 230.

does not represent an ideal candidate from a quantum chaos perspective, it does represent an ideal specimen from an OTOC perspective, because the negative Hamiltonian can be applied by simply changing the sign of the interaction strength J . This is accomplished in the experiment by changing the sign of the detuning, δ , between the optical dipole force and the the collective center-of-mass axial mode. Since the interaction strength scales as $J \sim 1/\delta$ this naturally allows for the precise implementation of $-H$, which mimics time-reversal dynamics. With the ability to stroboscopically apply both H and $-H$, a specific OTOC can then be measured by imaging the average magnetization of the system [230].

In the previous discussion, the stroboscopic application of H and $-H$ allowed the measurement of an out-of-time-ordered correlation function. Repeating this process of stroboscopically applying different Hamiltonian evolutions naturally leads to the

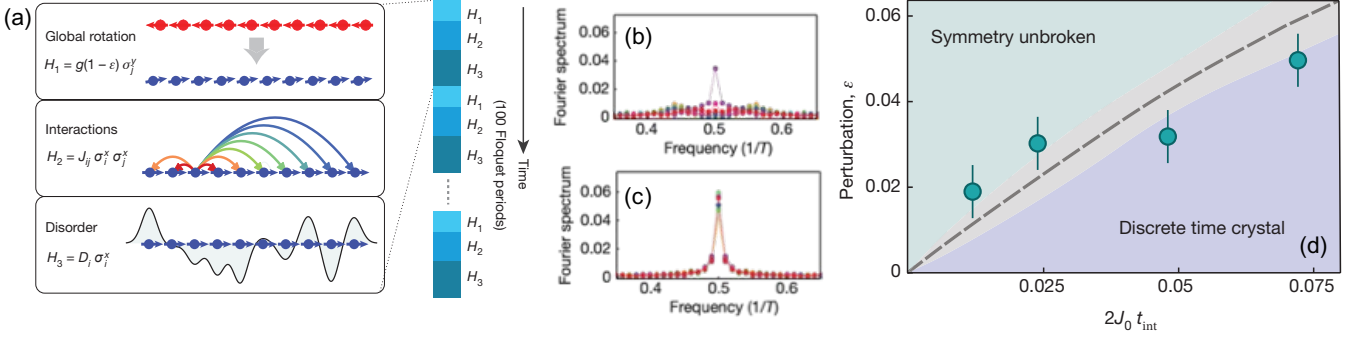


FIG. 27. Floquet quantum simulation of a DTC. (a) Schematic depiction of the Floquet evolution of a trapped ion spin chain. Three Hamiltonians are applied sequentially in time: a global spin rotation, long-range Ising interactions (generated as per the description in section II), and disorder. (b) The system evolves for ~ 100 Floquet periods during which the magnetization of each ion is tracked. Following this evolution, the Fourier spectrum of each ion’s evolution is computed. In the absence of interactions, small imperfections in the global rotation pulse lead to dynamics which do not exhibit any sub-harmonic features. (c) In the presence of interactions, a robust Fourier peak is observed at half the driving frequency, signaling the discrete breaking of time translation symmetry. (d) For stronger interactions, the DTC can tolerate larger imperfections to the global rotation pulse, leading to a qualitative phase diagram. Adapted from 240.

quantum simulation of Floquet systems [232, 233, 241]. In general, such time-periodic manipulations have long been used for controlling quantum systems including NMR qubits and atomic ensembles [242, 243]. However, recent explorations of Floquet systems have stumbled upon an intriguing question beyond the landscape of quantum control; in particular, can Floquet systems host intrinsically new phases of matter that do not have any equilibrium equivalent [244, 245]?

In the single-particle case, the question has been affirmatively answered with the discovery of a host of novel band structures that can only exist in the presence of periodic driving [246–250]. The many-body case is more subtle. On the one hand, one might naturally suspect that new phenomena can in principle arise when the driving frequency is of order the intrinsic energy scales of the system; indeed, this limit is far from the Suzuki-Trotter limit where to first order, the effective Hamiltonian describing the Floquet system is simply a sum of its stroboscopic components. On the other hand, one generically expects a driven many-body system to absorb energy from the driving field and ultimately to heat up to infinite temperature [232, 251]. Crucially, a number of recent theoretical advances have demonstrated that it is possible to avoid such an infinite temperature fate. One general scheme to prevent Floquet heating is to utilize many-body localization as discussed in section IV B. In principle, a Floquet MBL system [252, 253] can exhibit stable dynamical phases of matter for infinitely long times [254–256]. Interestingly, recent studies suggest an alternative disorder-free approach can also be used to combat Floquet heating, albeit not to infinitely late times. In particular, for large enough driving frequencies, the system can enter a regime of Floquet-prethermalization [233, 257], where exotic non-equilibrium phases can be observed for exponentially long time-scales [258–260]. The underlying essence of Floquet-prethermalization is analogous to the discussions of prethermalization in section IV C. The key difference is that here the lifetime of the quasi-stationary state in the Floquet context is controlled by the driving frequency.

We now turn to recent experiments which demonstrated a Floquet quantum simulation using a one dimensional trapped ion spin chain. In these experiments, a combination of high-precision spatial and temporal control allowed for the implementation of three distinct types of time evolution: 1) global spin rotations, 2) long-range Ising interactions, and 3) disordered on-site fields. The stroboscopic combination of these evolutions is the basis for realizing a discrete time crystal (DTC) [245, 254, 255, 261, 262], where a system exhibits a spontaneous breaking of the time-translation symmetry generated by the Floquet evolution. The characteristic signature of a DTC, which was observed in chains of up to $L = 14$ ions, is the robust synchronization of oscillations at sub-harmonic frequencies compared to that of the drive. Within the decoherence time-scale of the experiments, the observed signatures of DTC order are independent of the initial state. Crucially, the robustness of the sub-harmonic oscillations depends on the presence of strong interactions in the system; in the absence of interactions, small perturbation immediately destroy signatures of a time crystal.

In addition to implementations in trapped ion systems, a number of other experimental platforms have also observed signatures of time crystalline order [263, 264]. Here, we note a particular set of experiments performed using ensembles of nitrogen-vacancy (NV) color centers in diamonds [263]. We emphasize this particular platform because it shares a number of similar features with the trapped ion system (i.e. long range interactions and disorder), but also has a number of crucial differences (i.e. three dimensional system with time-dependent disorder). Interestingly, both platforms exhibit similar signatures of interaction stabilized time-translation symmetry breaking. To this end, such cross-platform verifications are especially valuable once controlled quantum simulators reach a regime where classical computers cannot calculate [265]. In this regard, comparing the results from analog quantum simulators to those from digital quantum computers would also be helpful in cross-checking

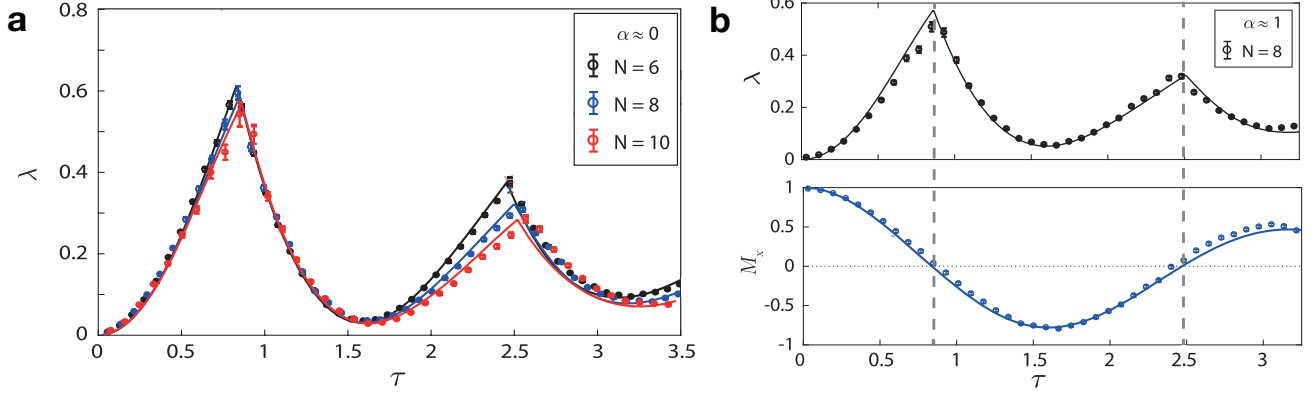


FIG. 28. Quantum simulation of DQPT based on nonanalytic response. **(a)** Measured rate function λ for three different system sizes at $B/J_0 \approx 2.38$, with $\tau = tB$ being the dimensionless time. The kinks in the evolution become sharper for larger N . In order to take into account the \mathbb{Z}_2 degeneracy of the ground state of H_0 , here the rate function is defined based on the return probability to the ground state manifold, namely $\lambda(t) = N^{-1} \log(P_{|\psi_0\rangle} + P_{|-\psi_0\rangle})$, where $|-\psi_0\rangle = |\uparrow\uparrow\uparrow \dots \uparrow\rangle_x$. **(b)** Comparison between rate function $\lambda(t)$ and magnetization evolution $M_x(t)$. The inversion of the magnetization sign corresponds to the nonanalyticity of the rate function $\lambda(t)$. Solid lines are exact numerical predictions based on experimental parameters ($B/J_0 = 2$). Adapted from 268.

and assessing validity [266].

E. Dynamical Phase Transitions

Having discussed the simulation of non-equilibrium phases in both disordered and periodically driven trapped ion experiments, we now turn to the question of understanding phase transitions in such out-of-equilibrium systems. Novel dynamical phases can emerge after a quantum quench, or unitary time-evolution in a spin system [267, 268]. Out-of-equilibrium systems do not necessarily behave thermodynamically, so it is a fundamental question how to properly establish analogies and differences among thermodynamic equilibrium phases and their dynamical counterparts [269, 270], in terms of order parameters [271, 272], scaling and universality [273], and discrete or continuous symmetry breaking [274–276]. Dynamical phases can be separated by dynamical quantum phase transitions (DQPT), characterized by non-analytic response of the physical system as a function of quench parameters. Two types of DQPT signatures have been defined for an interacting spin-1/2 chain [272] governed by the Hamiltonian:

$$H = \sum_{i,j} J_{i,j} \sigma_x^i \sigma_x^j + B \sum_i \sigma_z^i, \quad (31)$$

both of which have been experimentally observed in a trapped-ion quantum simulator. The first type of DQPT is based on the formal analogy between the non-analytic behaviour of the return probability to the initial state $|\psi_0\rangle$ after a quantum quench under the Hamiltonian H , defined as $\mathcal{G}(t) = \langle \psi_0 | e^{-iHt} | \psi_0 \rangle$, and the partition function of the corresponding equilibrium system $Z = \text{Tr}(e^{-H/k_B T})$ [277]. It is possible to define the complex counterpart of the thermodynamic free energy density $f = -N^{-1} k_B T \log(Z)$ using the rate function $\lambda(t) = -N^{-1} \log[\mathcal{G}(t)]$. This quantity, in the thermodynamic limit, exhibits dynamical real-time nonanalyticities that play an analogous role as the non-analytic behaviour of the free energy density of a thermodynamic system at equilibrium. It is possible to observe experimentally these nonanalyticities in an interacting spin chain after a quantum quench evolving under the long-range Transverse Field Ising Hamiltonian of Eq. (15).

This type of DQPT has been observed experimentally with a linear chain of trapped $^{40}\text{Ca}^+$ ion spins [268]. The spins are initialized in the ground state of the field part of the transverse Ising model, namely $|\psi_0\rangle = |\downarrow\downarrow\downarrow \dots \downarrow\rangle_x$, where $|\downarrow\rangle_z$ and $|\uparrow\rangle_z$ spin states are encoded in the $|S_{1/2}, m\rangle$ and $|D_{5/2}, m'\rangle$ atomic states respectively. Then the transverse field Hamiltonian (15) is suddenly switched on (quenched) with $B > J_0$, with J_0 being the average nearest-neighbour spin-spin coupling. As shown in Fig. 28a, in this regime the rate function λ exhibits pronounced nonanalyticities at the critical times t_c . This behaviour can be related to other observables, such as the global average magnetization $M_x = N^{-1} \sum_i \sigma_x^i$. Since the initial state breaks the \mathbb{Z}_2 symmetry of the Hamiltonian (15), the system restores this symmetry during the evolution at the times where the magnetization changes sign, which also corresponds to the critical times in the Loschmidt echo observable, as shown in Fig. 28b.

The second type of DQPT has an order parameter defined in terms of long time averaged observables, such as asymptotic

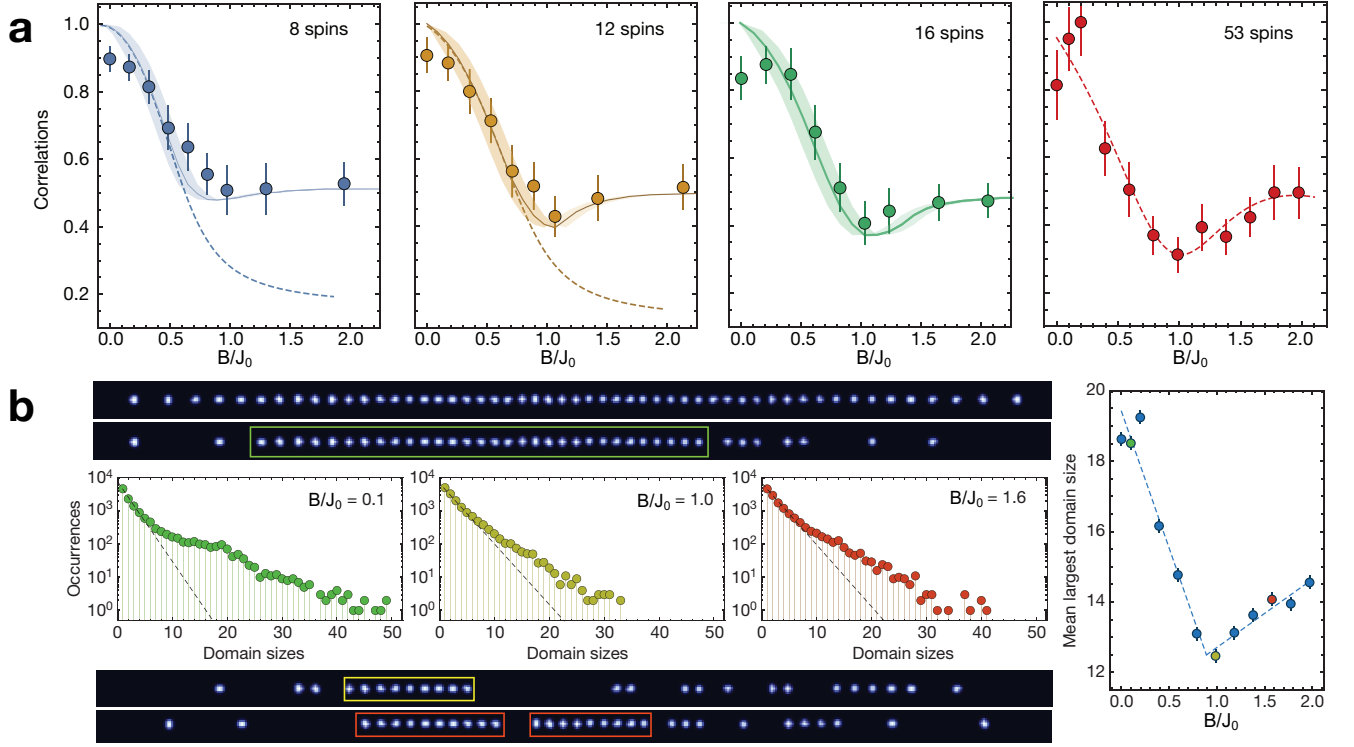


FIG. 29. Quantum simulation of a DQPT (a) Long-time averaged values of the two-body correlations C_2 , for different numbers of spins in the chain. Solid lines in (a)-(c) are exact numerical solutions to the Schrödinger equation, and the shaded regions take into account uncertainties from experimental Stark shift calibration errors. Dashed lines in (a) and (b) are calculations using a canonical (thermal) ensemble with an effective temperature corresponding to the initial energy density. (b) Domain statistics and reconstructed single shot images of 53 spins. (a) Top and bottom: reconstructed images based on binary detection of spin state. The top image shows a chain of 53 ions in bright spin states. The other three images show 53 ions in combinations of bright and dark spin states. Center: statistics of the sizes of domains for three different values of B/J_0 , plotted on a logarithmic scale. Dashed lines are fits to exponential functions, which could be expected for infinite-temperature thermal state. Long tails of deviations are clearly visible, and vary depending on B/J_0 . (b) Mean of the largest domain sizes in each single experimental shot. Dashed lines represent a piecewise linear fit, used to extract the transition point. The green, yellow, and red data points correspond to the transverse fields shown in the domain statistics data on the left. Adapted from 267.

late-time steady states of local observables:

$$\bar{A} = \lim_{T \rightarrow \infty} \frac{1}{T} \int_0^T A(t) dt, \quad (32)$$

where the operator A is the magnetization or higher order correlators between the spins. Here, the DQPT occurs as the ratio B/J_0 is varied and the order parameter changes abruptly from ferromagnetic ($B < J_0$) to paramagnetic order ($B > J_0$). The onset of this non-analytic behaviour can be observed by measuring the late time average values of the two-body correlator

$$C_2 = \sum_{ij} \langle \sigma_i^x \sigma_j^x \rangle / N^2, \quad (33)$$

after a quantum quench with Hamiltonian (31).

This type of DQPT measurement was observed in a linear chain of trapped $^{171}\text{Yb}^+$ ion spins [267]. Here, the measured late time correlator C_2 exhibits a dip at the critical point that sharpens scaling up the system size N up to 53 $^{171}\text{Yb}^+$ ions. Further evidence of the occurrence of the phase transition can be also observed in higher-order correlations, such as the domain size statistics, shown in Fig. 29b. The occurrence of the DQPT is observed in the decreased probabilities of observing long strings at the critical point. This is more clearly shown measuring the mean largest domain size as a function of the transverse field strength, for late times and repeated experimental shots, which exhibits a sharp transition across the critical point of the DQPT.

V. OUTLOOK

Quantum interacting spin models are among the simplest many-body quantum systems with nontrivial features that can elude classical computational solutions. Trapped atomic ion spins offer the ability to implement and control quantum spin models with some degree of tunability of the interaction form and range. Much of the research in this field has concentrated on studies of the long-range transverse Ising model, which can feature frustrated ground states with associated degeneracies and entanglement in the ground state. The many types of phase transitions and dynamical processes in this system form a fruitful testbed for studying quantum nonequilibrium processes, in many cases challenging classical computational power even for small numbers of spins. There are many extensions in this physical system to simulating more complex spin models with trapped ions such as Heisenberg couplings [278], higher-dimensional spin models, and interactions involving three or more spins. These future directions may allow the quantum simulation of more exotic spin phases such as spin liquids [105], or topological orders in spin systems such as the Haldane chain [127] or the Kitaev lattice [279].

There is a close relationship between spin simulations and quantum computations with qubits, and the underlying mechanism behind the Ising couplings in trapped ion spin simulations is exactly that used for discrete quantum gates between trapped ion qubits [54], which are sometimes called Ising gates. Quantum simulations in this sense can be considered as a special case of a quantum computation, and it should be expected that as trapped ion quantum computers scale in the future [6, 7], so will the reach of trapped ion quantum spin simulators.

VI. ACKNOWLEDGMENTS

We acknowledge key collaborations with Patrick Becker, Howard Carmichael, Ming-Shien Chang, Itzak Cohen, Emily Edwards, Michael Foss-Feig, James Freericks, Phillip Hauke, Markus Heyl, David Huse, Dvir Kafri, Harvey Kaplan, Antonis Kyprianidis, Simcha Korenblit, Aaron Lee, Guin-Dar Lin, Mohammad Maghrebi, Brian Neyenhuis, Changsuk Noh, Andrew Potter, Alex Retzker, Jacob Smith, Wen-Lin Tan, Ashvin Vishwanath, C.-C. Joseph Wang, and Jiehang Zhang. We thank R. Blatt, J. Bollinger, C. Roos, T. Schätz, and C. Wunderlich for permission to reprint their work. This work is supported by the ARO and AFOSR Atomic and Molecular Physics Programs, the AFOSR MURI on Quantum Measurement and Verification, the IARPA MUSIQC and LogiQ programs, the ARO MURI on Modular Quantum Systems, the ARL Center for Distributed Quantum Information, the NSF Quantum Information Science program, and the NSF Physics Frontier Center at JQI.

-
- [1] R. Feynman, *Int. J. Theor. Phys.* **21**, 467 (1982).
 - [2] A. Trabesinger, *Nature Physics* **8**, 264 (2012).
 - [3] M. A. Nielsen and I. L. Chuang, *Quantum Computation and Quantum Information* (Cambridge University Press, Cambridge, UK, 2000).
 - [4] T. D. Ladd, F. Jelezko, R. Laflamme, Y. Nakamura, C. Monroe, and J. L. O'Brien, *Nature* **464**, 45 (2010).
 - [5] D. Wineland and R. Blatt, *Nature* **453**, 1008 (2008).
 - [6] C. Monroe and J. Kim, *Science* **339**, 1164 (2013).
 - [7] K. R. Brown, J. Kim, and C. Monroe, *Nature Quant. Inf.* **2**, 16034 (2016).
 - [8] D. Porras and J. I. Cirac, *Phys. Rev. Lett.* **92**, 207901 (2004).
 - [9] X.-L. Deng, D. Porras, and J. I. Cirac, *Phys. Rev. A* **72**, 063407 (2005).
 - [10] J. M. Taylor and T. Calarco, *Phys. Rev. A* **78**, 062331 (2008).
 - [11] R. Blatt and C. F. Roos, *Nature Physics* **8**, 277 (2012).
 - [12] S. Bravyi and A. Kitaev, *Annals of Physics* **298**, 210 (2002).
 - [13] A. Aspuru-Guzik, A. D. Dutoi, P. J. Love, and M. Head-Gordon, *Science* **309**, 1704 (2005).
 - [14] N. M. Linke, S. Johri, C. Figgatt, K. A. Landsman, A. Y. Matsuura, and C. Monroe, *Phys. Rev. A* **98**, 052334 (2018).
 - [15] A. Peruzzo, J. McClean, P. Shadbolt, M.-H. Yung, X.-Q. Zhou, P. J. Love, A. Aspuru-Guzik, and J. L. O'Brien, *Nature Comm.* **5**, 4213 (2014).
 - [16] C. Hempel, C. Maier, J. Romero, J. McClean, T. Monz, H. Shen, P. Jurcevic, B. P. Lanyon, P. Love, R. Babbush, et al., *Phys. Rev. X* **8**, 031022 (2018).
 - [17] Y. Nam, J.-S. Chen, N. C. Panti, K. Wright, C. Delaney, D. Maslov, K. R. Brown, S. Allen, J. M. Amini, J. Apisdorf, et al., arXiv 1902.10171 (2019).
 - [18] E. Farhi, J. Goldstone, and S. Gutmann, arXiv 1411.4028 (2014).
 - [19] T. Byrnes and Y. Yamamoto, *Phys. Rev. A* **73**, 022328 (2006).
 - [20] S. P. Jordan, K. S. M. Lee, and J. Preskill, *Science* **336**, 1130 (2012).
 - [21] C. Muschik, M. Heyl, E. Martinez, T. Monz, P. Schindler, B. Vogell, M. Dalmonte, P. Hauke, R. Blatt, and P. Zoller, *New J. Phys.* **19**, 103020 (2017).

- [22] C. Kokail, C. Maier, R. van Bijnen, T. Brydges, M. K. Joshi, P. Jurcevic, C. A. Muschik, P. Silvi, R. Blatt, C. F. Roos, et al., *Nature* **569**, 355 (2019).
- [23] D. Yang, G. S. Giri, M. Johanning, C. Wunderlich, P. Zoller, and P. Hauke, *Phys. Rev. A* **94**, 052321 (2016).
- [24] P. Jordan and E. Wigner, *Zeitschrift für Physik* **47**, 631 (1928).
- [25] W. Happer, *Rev. Mod. Phys.* **44**, 169 (1972).
- [26] D. Leibfried, R. Blatt, C. Monroe, and D. Wineland, *Rev. Mod. Phys.* **75**, 281 (2003).
- [27] W. Nagourney, J. Sandberg, and H. Dehmelt, *Phys. Rev. Lett.* **56**, 2797 (1986).
- [28] T. Sauter, W. Neuhauser, R. Blatt, and P. E. Toschek, *Phys. Rev. Lett.* **57**, 1696 (1986).
- [29] J. C. Bergquist, R. G. Hulet, W. M. Itano, and D. J. Wineland, *Phys. Rev. Lett.* **57**, 1699 (1986).
- [30] M. Acton, K.-A. Brickman, P. C. Haljan, P. J. Lee, L. Deslauriers, and C. Monroe, *Quantum Inf. Comp.* **6**, 465 (2006).
- [31] D. B. Hume, T. Rosenband, and D. J. Wineland, *Phys. Rev. Lett.* **99**, 120502 (2007).
- [32] J. Benhelm, G. Kirchmair, C. F. Roos, and R. Blatt, *Nature Physics* **4**, 463 (2008).
- [33] A. H. Myerson, D. J. Szwer, S. C. Webster, D. T. C. Allcock, M. J. Curtis, G. Imreh, J. A. Sherman, D. N. Stacey, A. M. Steane, and D. M. Lucas, *Phys. Rev. Lett.* **100**, 200502 (2008).
- [34] R. Noek, G. Vrijsen, D. Gaultney, E. Mount, T. Kim, P. Maunz, and J. Kim, *Opt. Lett.* **38**, 4735 (2013).
- [35] M. Raizen, J. Gilligan, J. Bergquist, W. Itano, and D. Wineland, *J. Mod. Opt.* **39**, 233 (1992).
- [36] H. Dehmelt, *Adv. At. Mol. Phys.* **3**, 53 (1967).
- [37] W. Paul, *Rev. Mod. Phys.* **62**, 531 (1990).
- [38] D. F. V. James, *Appl. Phys. B* **66**, 181 (1998).
- [39] G.-D. Lin, S.-L. Zhu, R. Islam, K. Kim, M.-S. Chang, S. Korenblit, C. Monroe, and L.-M. Duan, *Europhys. Lett.* **86**, 60004 (2009).
- [40] L. S. Brown and G. Gabrielse, *Rev. Mod. Phys.* **58**, 233 (1986).
- [41] J. G. Bohnet, B. C. Sawyer, J. W. Britton, M. L. Wall, A. M. Rey, M. Foss-Feig, and J. J. Bollinger, *Science* **352**, 1297 (2016).
- [42] R. Islam, E. Edwards, K. Kim, S. Korenblit, C. Noh, H. Carmichael, G. Lin, L. Duan, C. J. Wang, J. Freericks, et al., *Nature Comm.* **2**, 377 (2011).
- [43] D. J. Wineland, C. Monroe, W. M. Itano, D. Leibfried, B. E. King, and D. M. Meekhof, *J. Res. Nat. Inst. Stand. Tech.* **103**, 259 (1998).
- [44] B. C. Sawyer, J. W. Britton, A. C. Keith, C.-C. J. Wang, J. K. Freericks, H. Uys, M. J. Biercuk, and J. J. Bollinger, *Phys. Rev. Lett.* **108**, 213003 (2012).
- [45] C. Marquet, F. Schmidt-Kaler, and D. James, *Applied Physics B* **76**, 199 (2003).
- [46] J. I. Cirac and P. Zoller, *Phys. Rev. Lett.* **74**, 4091 (1995).
- [47] A. Sørensen and K. Mølmer, *Phys. Rev. Lett.* **82**, 1971 (1999).
- [48] G. Milburn, S. Schneider, and D. James, *Fortschritte der Physik* **48**, 801 (2000).
- [49] E. Solano, R. L. de Matos Filho, and N. Zagury, *Phys. Rev. A* **59**, R2539 (1999).
- [50] H. Häffner, S. Gulde, M. Riebe, G. Lancaster, C. Becher, J. Eschner, F. Schmidt-Kaler, and R. Blatt, *Phys. Rev. Lett.* **90**, 143602 (2003).
- [51] A. C. Lee, J. Smith, P. Richerme, B. Neyenhuis, P. W. Hess, J. Zhang, and C. Monroe, *Phys. Rev. A* **94**, 042308 (2016).
- [52] S.-L. Zhu, C. Monroe, and L.-M. Duan, *Phys. Rev. Lett.* **97**, 050505 (2006).
- [53] P. J. Lee, K.-A. Brickman, L. Deslauriers, P. C. Haljan, L.-M. Duan, and C. Monroe, *Journal of Optics B: Quantum and Semiclassical Optics* **7**, S371 (2005).
- [54] A. Sørensen and K. Mølmer, *Phys. Rev. A* **62**, 022311 (2000).
- [55] P. Nevado and D. Porras, *Phys. Rev. A* **93**, 013625 (2016).
- [56] S. Korenblit, D. Kafri, W. C. Campbell, R. Islam, E. E. Edwards, Z.-X. Gong, G.-D. Lin, L.-M. Duan, J. Kim, K. Kim, et al., *New Journal of Physics* **14**, 095024 (2012).
- [57] G.-D. Lin, C. Monroe, and L.-M. Duan, *Phys. Rev. Lett.* **106**, 230402 (2011).
- [58] D. Hayes, S. T. Flammia, and M. J. Biercuk, *New Journal of Physics* **16**, 083027 (2014).
- [59] F. Rajabi, S. Motlakunta, C.-Y. Shih, N. Kotibhaskar, Q. Quraishi, A. Ajoy, and R. Islam, *npj Quantum Information* **5**, 32 (2019).
- [60] S. Sachdev, *Quantum phase transitions* (Cambridge university press, 2011).
- [61] J. I. Cirac and P. Zoller, *Nature Physics* **8**, 264 (2012).
- [62] D. Hangleiter, M. Kliesch, M. Schwarz, and J. Eisert, *Quantum Sci. Technol.* **2**, 015004 (2017).
- [63] J. Preskill, *Proc. R. Soc. Lond. A* **454**, 385 (1998).
- [64] D. Gottesman, *Phys. Rev. A* **57**, 127 (1998).
- [65] D. Leibfried, *Nature* **463**, 608 (2010).
- [66] S. Lloyd, *Science* **273**, 1073 (1996).
- [67] B. P. Lanyon, C. Hempel, D. Nigg, M. Müller, R. Gerritsma, F. Zähringer, P. Schindler, J. Barreiro, M. Rambach, G. Kirchmair, et al., *Science* **334**, 57 (2011).
- [68] B. M. Terhal, *Rev. Mod. Phys.* **87**, 307 (2015).
- [69] K. R. Brown, R. J. Clark, and I. L. Chuang, *Phys. Rev. Lett.* **97**, 050504 (2006).
- [70] C. R. Clark, T. S. Metodi, S. D. Gasster, and K. R. Brown, *Phys. Rev. A* **79**, 062314 (2009).
- [71] P. Hauke, F. M. Cucchietti, L. Tagliacozzo, I. Deutsch, and M. Lewenstein, *Rep. Prog. Phys.* **75**, 082401 (2012).
- [72] V. M. Kendon, K. Nemoto, and W. J. Munro, *Phil. Trans. R. Soc. A* **368**, 3609 (2010).
- [73] R. Islam, C. Senko, W. Campbell, S. Korenblit, J. Smith, A. Lee, E. Edwards, C.-C. Wang, J. Freericks, and C. Monroe, *Science* **340**, 583 (2013).
- [74] R. Ozeri, W. M. Itano, R. B. Blakestad, J. Britton, J. Chiaverini, J. D. Jost, C. Langer, D. Leibfried, R. Reichle, S. Seidelin, et al., *Phys. Rev. A* **75** (2007).
- [75] C. J. Wang and J. K. Freericks, *Phys. Rev. A* **86**, 032329 (2012).
- [76] M. L. Wall, A. Safavi-Naini, and A. M. Rey, *Phys. Rev. A* **95**, 013602 (2017).

- [77] J. Roland and N. J. Cerf, *Phys. Rev. A* **65**, 042308 (2002).
- [78] P. Richerme, C. Senko, J. Smith, A. Lee, and C. Monroe, *Phys. Rev. A* **88**, 012334 (2013).
- [79] C. Shen and L.-M. Duan, *New J. Phys.* **14**, 053053 (2012).
- [80] T. Ruster, C. T. Schmiegelow, H. Kaufmann, C. Warschburger, F. Schmidt-Kaler, and U. G. Poschinger, *Applied Physics B* **122**, 254 (2016).
- [81] K. Kim, S. Korenblit, R. Islam, E. Edwards, M. Chang, C. Noh, H. Carmichael, G. Lin, L. Duan, C. J. Wang, et al., *New J. of Phys.* **13**, 105003 (2011).
- [82] A. Khromova, C. Piltz, B. Scharfenberger, T. Gloger, M. Johanning, A. Varón, and C. Wunderlich, *Phys. Rev. Lett.* **108**, 220502 (2012).
- [83] C. Piltz, T. Sriarunothai, S. S. Ivanov, S. Wölk, and C. Wunderlich, *Science Advances* **2**, e1600093 (2016).
- [84] K. Kim, M.-S. Chang, R. Islam, S. Korenblit, L.-M. Duan, and C. Monroe, *Phys. Rev. Lett.* **103**, 120502 (2009).
- [85] P. Jurcevic, B. Lanyon, P. Hauke, C. Hempel, P. Zoller, R. Blatt, and C. Roos, *Nature* **511**, 202 (2014).
- [86] C. Senko, J. Smith, P. Richerme, A. Lee, W. Campbell, and C. Monroe, *Science* **345**, 430 (2014).
- [87] W. Kohn, *Rev. Mod. Phys.* **71**, 1253 (1999).
- [88] W. M. C. Foulkes, L. Mitas, R. J. Needs, and G. Rajagopal, *Rev. Mod. Phys.* **73**, 33 (2001).
- [89] U. Schollwöck, *Rev. Mod. Phys.* **77**, 259 (2005).
- [90] F. Jensen, *An Introduction to Computational Chemistry* (J Wiley and Sons Ltd, 1989).
- [91] M. L. Kolsgaard, G. Joner, C. Brunborg, S. A. Anderssen, S. Tonstad, and L. F. Andersen, *Science* **292**, 472 (2001).
- [92] S. Lloyd, *Science* **319**, 1209 (2008).
- [93] T. Albash and D. A. Lidar, *Rev. Mod. Phys.* **90**, 015002 (2018).
- [94] A. Friedenauer, H. Schmitz, J. T. Glueckert, D. Porras, and T. Schätz, *Nature Physics* **4**, 757 (2008).
- [95] K. Kim, M.-S. Chang, S. Korenblit, R. Islam, E. E. Edwards, J. K. Freericks, G.-D. Lin, L.-M. Duan, and C. Monroe, *Nature* **465**, 590 (2010).
- [96] E. E. Edwards, S. Korenblit, K. Kim, R. Islam, M.-S. Chang, J. K. Freericks, G.-D. Lin, L.-M. Duan, and C. Monroe, *Phys. Rev. B* **82**, 060412 (2010).
- [97] C. Schneider, D. Porras, and T. Schaetz, *Rep. Prog. Phys.* **75**, 024401 (2012).
- [98] P. Richerme, C. Senko, S. Korenblit, J. Smith, A. Lee, R. Islam, W. C. Campbell, and C. Monroe, *Phys. Rev. Lett.* **111**, 100506 (2013).
- [99] J. T. Barreiro, M. Müller, P. Schindler, D. Nigg, T. Monz, M. Chwalla, M. Hennrich, C. F. Roos, P. Zoller, and R. Blatt, *Nature* **470**, 486 (2011).
- [100] Y. Lin, J. Gaebler, F. Reiter, T. R. Tan, R. Bowler, A. Sørensen, D. Leibfried, and D. J. Wineland, *Nature* **504**, 415 (2013).
- [101] J. Baugh, O. Moussa, C. A. Ryan, A. Nayak, and R. Laflamme, *Nature* **438**, 470 (2005).
- [102] J.-S. Xu, M.-H. Yung, X.-Y. Xu, S. Boixo, Z.-W. Zhou, C.-F. Li, A. Aspuru-Guzik, and G.-C. Guo, *Nature Photonics* **8**, 113 (2014).
- [103] R. Moessner and A. P. Ramirez, *Phys. Today* **59**, 24 (2006).
- [104] K. Binder and A. P. Young, *Rev. Mod. Phys.* **58**, 801 (1986).
- [105] L. Balents, *Nature* **464**, 199 (2010).
- [106] E. Farhi, J. Goldstone, S. Gutmann, and M. Sipser, arXiv: 0001106 (2000).
- [107] A. W. Sandvik, *Phys. Rev. Lett.* **104**, 137204 (2010).
- [108] N. Khaneja, T. Reiss, C. Kehlet, T. Schulte-Herbrüggen, and S. J. Glaser, *J. Magn. Reson.* **172**, 296 (2005).
- [109] V. F. Krotov, *Global Methods in Optimal Control Theory* (Dekker, New York, 1996).
- [110] A. Safavi-Naini, R. J. Lewis-Swan, J. Bohnet, M. Gartner, K. Gilmore, E. Jordan, J. Cohn, J. K. Freericks, A. Rey, and J. Bollinger, arXiv p. 1711.07392 (2017).
- [111] A. Messiah, *Quantum Mechanics* (North-Holland, Amsterdam, 1962).
- [112] H. T. Quan and W. H. Zurek, *New J. Phys.* **12**, 093025 (2010).
- [113] C. Lanczos, *J. Res. Nat. Bur. Standards* **45**, 255 (1950).
- [114] L. Viola and S. Lloyd, *Phys. Rev. A* **58**, 2733 (1998).
- [115] S. Balasubramanian, S. Han, B. T. Yoshimura, and J. K. Freericks, *Phys. Rev. A* **97**, 022313 (2018).
- [116] W. W. Ho, C. Jonay, and T. H. Hsieh, *Phys. Rev. A* **99**, 052332 (2019).
- [117] A. Khromova, C. Piltz, B. Scharfenberger, T. F. Gloger, M. Johanning, A. F. Varón, and C. Wunderlich, *Phys. Rev. Lett.* **108**, 220502 (2012).
- [118] A. Acín, A. Andrianov, E. Jané, and R. Tarrach, *Journal of Physics A: Mathematical and General* **34**, 6725 (2001).
- [119] O. Gühne and G. Tóth, *Physics Reports* **474**, 1 (2009).
- [120] C. A. Sackett, D. Kielpinski, B. E. King, C. Langer, V. Meyer, C. J. Myatt, M. Rowe, Q. A. Turchette, W. M. Itano, and D. J. Wineland, *Nature* **404**, 256 (2000).
- [121] C. Zener, *Proc. R. Soc. A* **137**, 696 (1932).
- [122] B. Damski and W. H. Zurek, *Phys. Rev. A* **73**, 063405 (2006).
- [123] W. M. Itano, J. C. Bergquist, J. J. Bollinger, J. M. Gilligan, D. J. Heinzen, F. L. Moore, M. G. Raizen, and D. J. Wineland, *Phys. Rev. A* **47**, 3554 (1993).
- [124] E. Wigner, *Phys. Rev.* **46**, 1002 (1934).
- [125] K. Katayama and H. Narihisa, *Eur. J. of Oper. Res.* **134**, 103 (2001).
- [126] P. Bak and R. Bruinsma, *Phys. Rev. Lett.* **49**, 249 (1982).
- [127] F. D. M. Haldane, *Phys. Rev. Lett.* **50**, 1153 (1983).
- [128] M. den Nijs and K. Rommelse, *Phys. Rev. B* **40**, 4709 (1989).
- [129] T. Kennedy and H. Tasaki, *Phys. Rev. B* **45**, 304 (1992).
- [130] F. Pollmann, A. M. Turner, E. Berg, and M. Oshikawa, *Phys. Rev. B* **81**, 064439 (2010).
- [131] I. Cohen, P. Richerme, Z.-X. Gong, C. Monroe, and A. Retzker, *Phys. Rev. A* **92**, 012334 (2015).

- [132] Z.-X. Gong, M. F. Maghrebi, A. Hu, M. Foss-Feig, P. Richerme, C. Monroe, and A. V. Gorshkov, *Phys. Rev. B* **93**, 205115 (2016).
- [133] K. Mølmer and A. Sørensen, *Phys. Rev. Lett.* **82**, 1835 (1999).
- [134] C. Senko, P. Richerme, J. Smith, A. Lee, I. Cohen, A. Retzker, and C. Monroe, *Phys. Rev. X* **5**, 021026 (2015).
- [135] L. D'Alessio, Y. Kafri, A. Polkovnikov, and M. Rigol, *Adv. Phys.* **65**, 239 (2016).
- [136] E. H. Lieb and D. W. Robinson, *Comm. Math. Phys.* **28**, 251 (1972).
- [137] M. B. Hastings and T. Koma, *Comm. Math. Phys.* **265**, 781 (2006).
- [138] N. Lashkari, D. Stanford, M. Hastings, T. Osborne, and P. Hayden, *J. High Energy. Phys.* **2013**, 22 (2013).
- [139] Z.-X. Gong, M. Foss-Feig, S. Michalakis, and A. V. Gorshkov, *Phys. Rev. Lett.* **113**, 030602 (2014).
- [140] M. Foss-Feig, Z.-X. Gong, C. W. Clark, and A. V. Gorshkov, *Phys. Rev. Lett.* **114**, 157201 (2015).
- [141] D.-M. Storch, M. van den Worm, and M. Kastner, *New J. Phys.* **17**, 063021 (2015).
- [142] T. Matsuta, T. Koma, and S. Nakamura, *Ann. Henri Poincaré* **18**, 519 (2017).
- [143] M. C. Tran, A. Y. Guo, Y. Su, J. R. Garrison, Z. Eldredge, M. Foss-Feig, A. M. Childs, and A. V. Gorshkov, arXiv:1808.05225 (2018).
- [144] D. V. Else, F. Machado, C. Nayak, and N. Y. Yao, arXiv:1809.06369 (2018).
- [145] A. Y. Guo, M. C. Tran, A. M. Childs, A. V. Gorshkov, and Z.-X. Gong, arXiv:1906.02662 (2019).
- [146] R. Sweke, J. Eisert, and M. Kastner, *J. Phys. A* **52**, 424003 (2019).
- [147] M. C. Tran, A. Ehrenberg, A. Y. Guo, P. Titum, D. A. Abanin, and A. V. Gorshkov, arXiv:1908.02773 (2019).
- [148] C.-F. Chen and A. Lucas, arXiv:1907.07637 (2019).
- [149] T. Kuwahara and K. Saito, arXiv:1910.14477 (2019).
- [150] K. R. A. Hazzard, S. R. Manmana, M. Foss-Feig, and A. M. Rey, *Phys. Rev. Lett.* **110**, 075301 (2013).
- [151] P. Hauke and L. Tagliacozzo, *Phys. Rev. Lett.* **111**, 207202 (2013).
- [152] J. Schachenmayer, B. P. Lanyon, C. F. Roos, and A. J. Daley, *Phys. Rev. X* **3**, 031015 (2013).
- [153] M. Knap, A. Kantian, T. Giamarchi, I. Bloch, M. D. Lukin, and E. Demler, *Phys. Rev. Lett.* **111**, 147205 (2013).
- [154] J. Jünemann, A. Cadarso, D. Pérez-García, A. Bermudez, and J. J. García-Ripoll, *Phys. Rev. Lett.* **111**, 230404 (2013).
- [155] J. Eisert, M. van den Worm, S. R. Manmana, and M. Kastner, *Phys. Rev. Lett.* **111**, 260401 (2013).
- [156] K. R. A. Hazzard, B. Gadway, M. Foss-Feig, B. Yan, S. A. Moses, J. P. Covey, N. Y. Yao, M. D. Lukin, J. Ye, D. S. Jin, et al., *Phys. Rev. Lett.* **113**, 195302 (2014).
- [157] M. G. Nezhadhighi and M. A. Rajabpour, *Phys. Rev. B* **90**, 205438 (2014).
- [158] M. A. Rajabpour and S. Sotiriadis, *Phys. Rev. B* **91**, 045131 (2015).
- [159] Z. Eldredge, Z.-X. Gong, J. T. Young, A. H. Moosavian, M. Foss-Feig, and A. V. Gorshkov, *Phys. Rev. Lett.* **119**, 170503 (2017).
- [160] M. F. Maghrebi, Z.-X. Gong, M. Foss-Feig, and A. V. Gorshkov, *Phys. Rev. B* **93**, 125128 (2016).
- [161] D. J. Luitz and Y. Bar Lev, *Phys. Rev. A* **99**, 010105 (2019).
- [162] A. S. Buyskikh, M. Fagotti, J. Schachenmayer, F. Essler, and A. J. Daley, *Phys. Rev. A* **93**, 053620 (2016).
- [163] L. Cevolani, G. Carleo, and L. Sanchez-Palencia, *Phys. Rev. A* **92**, 041603 (2015).
- [164] L. Cevolani, G. Carleo, and L. Sanchez-Palencia, *New Journal of Physics* **18**, 093002 (2016).
- [165] M. Van Regemortel, D. Sels, and M. Wouters, *Phys. Rev. A* **93**, 032311 (2016).
- [166] L. Lepori, A. Trombettoni, and D. Vodola, *J. Stat. Mech.: Theory and Exper.* **2017**, 033102 (2017).
- [167] L. Cevolani, J. Despres, G. Carleo, L. Tagliacozzo, and L. Sanchez-Palencia, *Phys. Rev. B* **98**, 024302 (2018).
- [168] I. Frérot, P. Naldesi, and T. Roscilde, *Phys. Rev. Lett.* **120**, 050401 (2018).
- [169] X. Chen, T. Zhou, and C. Xu, *J. Stat. Mech.: Theory and Exper.* **2018**, 073101 (2018).
- [170] X. Chen and T. Zhou, arXiv:1808.09812 (2018).
- [171] M. Kastner, *Phys. Rev. Lett.* **106**, 130601 (2011).
- [172] R. Bachelard and M. Kastner, *Phys. Rev. Lett.* **110**, 170603 (2013).
- [173] M. v. d. Worm, B. C. Sawyer, J. J. Bollinger, and M. Kastner, *New J. Phys.* **15**, 083007 (2013).
- [174] B. Kloss and Y. Bar Lev, *Phys. Rev. A* **99**, 032114 (2019).
- [175] M. Cheneau, P. Barmettler, D. Poletti, M. Endres, P. Schausz, T. Fukuhara, C. Gross, I. Bloch, C. Kollath, and S. Kuhr, *Nature (London)* **481**, 484 (2012).
- [176] S. Bravyi, M. B. Hastings, and F. Verstraete, *Phys. Rev. Lett.* **97**, 050401 (2006).
- [177] Z.-X. Gong, M. Foss-Feig, S. Michalakis, and A. V. Gorshkov, arXiv:1401.6174v1 (2014).
- [178] P. Richerme, Z.-X. Gong, A. Lee, C. Senko, J. Smith, M. Foss-Feig, S. Michalakis, A. V. Gorshkov, and C. Monroe, *Nature* **511**, 198 (2014).
- [179] N. Friis, O. Marty, C. Maier, C. Hempel, M. Holzäpfel, P. Jurcevic, M. B. Plenio, M. Huber, C. Roos, R. Blatt, et al., *Phys. Rev. X* **8**, 021012 (2018).
- [180] B. Yan, S. A. Moses, B. Gadway, J. P. Covey, K. R. A. Hazzard, A. M. Rey, D. S. Jin, and J. Ye, *Nature (London)* **501**, 521 (2013).
- [181] J. Choi, S. Choi, G. Kuesko, P. C. Maurer, B. J. Shields, H. Sumiya, S. Onoda, J. Isoya, E. Demler, F. Jelezko, et al., *Phys. Rev. Lett.* **118**, 093601 (2017).
- [182] H. Bernien, S. Schwartz, A. Keesling, H. Levine, A. Omran, H. Pichler, S. Choi, A. S. Zibrov, M. Endres, M. Greiner, et al., *Nature* **551**, 579 (2017).
- [183] V. Lienhard, S. de Léséleuc, D. Barredo, T. Lahaye, A. Browaeys, M. Schuler, L.-P. Henry, and A. M. Läuchli, *Phys. Rev. X* **8**, 021070 (2018).
- [184] E. Guardado-Sanchez, P. T. Brown, D. Mitra, T. Devakul, D. A. Huse, P. Schauß, and W. S. Bakr, *Phys. Rev. X* **8**, 021069 (2018).
- [185] J. Zeiher, J.-y. Choi, A. Rubio-Abadal, T. Pohl, R. van Bijnen, I. Bloch, and C. Gross, *Phys. Rev. X* **7**, 041063 (2017).
- [186] S. de Léséleuc, V. Lienhard, P. Scholl, D. Barredo, S. Weber, N. Lang, H. P. Büchler, T. Lahaye, and A. Browaeys, arXiv:1810.13286 (2018).
- [187] V. Oganesyan and D. A. Huse, *Phys. Rev. B* **75**, 155111 (2007).

- [188] R. Nandkishore and D. A. Huse, *Annual Review of Condensed Matter Physics* **6**, 15 (2015).
- [189] D. A. Abanin, E. Altman, I. Bloch, and M. Serbyn, *Reviews of Modern Physics* **91**, 021001 (2019).
- [190] M. Schreiber, S. S. Hodgman, P. Bordia, H. P. Lüschen, M. H. Fischer, R. Vosk, E. Altman, U. Schneider, and I. Bloch, *Science* **349**, 842 (2015).
- [191] J.-y. Choi, S. Hild, J. Zeiher, P. Schauß, A. Rubio-Abadal, T. Yefsah, V. Khemani, D. A. Huse, I. Bloch, and C. Gross, *Science* **352**, 1547 (2016).
- [192] P. W. Anderson, *Phys. Rev.* **109**, 1492 (1958).
- [193] J. H. Bardarson, F. Pollmann, and J. E. Moore, *Phys. Rev. Lett.* **109**, 017202 (2012).
- [194] D. J. Luitz, N. Laflorencie, and F. Alet, *Phys. Rev. B* **91**, 081103 (2015).
- [195] M. Serbyn, M. Knap, S. Gopalakrishnan, Z. Papić, N. Y. Yao, C. Laumann, D. Abanin, M. D. Lukin, and E. A. Demler, *Phys. Rev. Lett.* **113**, 147204 (2014).
- [196] J. Smith, A. Lee, P. Richerme, B. Neyenhuis, P. Hess, P. Hauke, M. Heyl, D. Huse, and C. Monroe, *Nature Physics* **12**, 907 (2016).
- [197] T. Brydges, A. Elben, P. Jurcevic, B. Vermersch, C. Maier, B. P. Lanyon, P. Zoller, R. Blatt, and C. F. Roos, *Science (New York, N.Y.)* **364**, 260 (2019).
- [198] P. Hauke and M. Heyl, *Phys. Rev. B* **92**, 134204 (2015).
- [199] A. O. Maksymov, N. Rahman, E. Kapit, and A. L. Burin, *Phys. Rev. A* **96**, 057601 (2017).
- [200] A. L. Burin, *cond-mat/0611387* (2006).
- [201] N. Y. Yao, C. R. Laumann, S. Gopalakrishnan, M. Knap, M. Mueller, E. A. Demler, and M. D. Lukin, *Phys. Rev. Lett.* **113**, 243002 (2014).
- [202] A. L. Burin, *Phys. Rev. B* **92**, 104428 (2015).
- [203] R. M. Nandkishore and S. L. Sondhi, *Phys. Rev. X* **7**, 041021 (2017).
- [204] J. M. Deutsch, *Phys. Rev. A* **43**, 2046 (1991).
- [205] M. Srednicki, *Phys. Rev. E* **50**, 888 (1994).
- [206] M. Rigol, V. Dunjko, and M. Olshanii, *Nature* **452**, 854 (2008).
- [207] Y.-L. Wu and S. Das Sarma, *Phys. Rev. A* **93**, 022332 (2016).
- [208] C. Maier, T. Brydges, P. Jurcevic, N. Trautmann, C. Hempel, B. P. Lanyon, P. Hauke, R. Blatt, and C. F. Roos, *Phys. Rev. Lett.* **122** (2019).
- [209] M. Pino, *Phys. Rev. B* **90**, 174204 (2014).
- [210] H. P. Lüschen, P. Bordia, S. Scherg, F. Alet, E. Altman, U. Schneider, and I. Bloch, *Phys. Rev. Lett.* **119**, 260401 (2017).
- [211] T. Kohlert, S. Scherg, X. Li, H. P. Lüschen, S. Das Sarma, I. Bloch, and M. Aidelsburger, *Phys. Rev. Lett.* **122**, 170403 (2019).
- [212] A. Lukin, M. Rispoli, R. Schittko, M. E. Tai, A. M. Kaufman, S. Choi, V. Khemani, J. Léonard, and M. Greiner, *Science (New York, N.Y.)* **364**, 256 (2019).
- [213] P. Bordia, H. P. Lüschen, S. S. Hodgman, M. Schreiber, I. Bloch, and U. Schneider, *Phys. Rev. Lett.* **116**, 140401 (2016).
- [214] H. P. Lüschen, P. Bordia, S. S. Hodgman, M. Schreiber, S. Sarkar, A. J. Daley, M. H. Fischer, E. Altman, I. Bloch, and U. Schneider, *Phys. Rev. X* **7**, 011034 (2017).
- [215] S. S. Kondov, W. R. McGehee, W. Xu, and B. DeMarco, *Phys. Rev. Lett.* **114**, 083002 (2015).
- [216] P. Bordia, H. Lüschen, S. Scherg, S. Gopalakrishnan, M. Knap, U. Schneider, and I. Bloch, *Phys. Rev. X* **7**, 041047 (2017).
- [217] W. De Roeck and J. Z. Imbrie, *Phil. Trans. Royal Soc. London A: Math., Phys. and Eng. Sci.* **375** (2017).
- [218] P. Roushan, C. Neill, J. Tangpanitanon, V. M. Bastidas, A. Megrant, R. Barends, Y. Chen, Z. Chen, B. Chiaro, A. Dunsworth, et al., *Science* **358**, 1175 (2017).
- [219] K. X. Wei, C. Ramanathan, and P. Cappellaro, *Phys. Rev. Lett.* **120**, 070501 (2018).
- [220] K. Xu, J.-J. Chen, Y. Zeng, Y.-R. Zhang, C. Song, W. Liu, Q. Guo, P. Zhang, D. Xu, H. Deng, et al., *Phys. Rev. Lett.* **120**, 050507 (2018).
- [221] T. Kinoshita, T. Wenger, and D. S. Weiss, *Nature* **440**, 900 (2006).
- [222] M. Gring, M. Kuhnert, T. Langen, T. Kitagawa, B. Rauer, M. Schreitl, I. Mazets, D. A. Smith, E. Demler, and J. Schmiedmayer, *Science* **337**, 1318 (2012).
- [223] T. Langen, S. Erne, R. Geiger, B. Rauer, T. Schweigler, M. Kuhnert, W. Rohringer, I. E. Mazets, T. Gasenzer, and J. Schmiedmayer, *Science* **348**, 207 (2015).
- [224] M. Rigol, V. Dunjko, V. Yurovsky, and M. Olshanii, *Phys. Rev. Lett.* **98**, 050405 (2007).
- [225] J. Berges, S. Borsányi, and C. Wetterich, *Phys. Rev. Lett.* **93**, 142002 (2004).
- [226] A. Polkovnikov, K. Sengupta, A. Silva, and M. Vengalattore, *Rev. Mod. Phys.* **83**, 863 (2011).
- [227] S. R. Manmana, S. Wessel, R. M. Noack, and A. Muramatsu, *Phys. Rev. Lett.* **98**, 210405 (2007).
- [228] Z.-X. Gong and L.-M. Duan, *New J. Phys.* **15**, 113051 (2013).
- [229] B. Neyenhuis, J. Zhang, P. W. Hess, J. Smith, A. C. Lee, P. Richerme, Z.-X. Gong, A. V. Gorshkov, and C. Monroe, *Science Advances* **3** (2017).
- [230] M. Gärtner, J. G. Bohnet, A. Safavi-Naini, M. L. Wall, J. J. Bollinger, and A. M. Rey, *Nature Physics* **13**, 781 (2017).
- [231] G. Floquet, in *Annales scientifiques de l'École normale supérieure* (1883), vol. 12, pp. 47–88.
- [232] M. Bukov, L. D'Alessio, and A. Polkovnikov, *Advances in Physics* **64**, 139 (2015).
- [233] T. Kuwahara, T. Mori, and K. Saito, *Annals of Physics* **367**, 96 (2016).
- [234] I. Bloch, J. Dalibard, and W. Zwerger, *Reviews of modern physics* **80**, 885 (2008).
- [235] A. Larkin and Y. N. Ovchinnikov, *Sov. Phys. JETP* **28**, 1200 (1969).
- [236] J. Maldacena, S. H. Shenker, and D. Stanford, *Journal of High Energy Physics* **2016**, 106 (2016).
- [237] B. Swingle, G. Bentsen, M. Schleier-Smith, and P. Hayden, *Phys. Rev. A* **94**, 040302 (2016).
- [238] K. A. Landsman, C. Figgatt, T. Schuster, N. M. Linke, B. Yoshida, N. Y. Yao, and C. Monroe, *Nature* **567**, 61 (2019).

- [239] J. Li, R. Fan, H. Wang, B. Ye, B. Zeng, H. Zhai, X. Peng, and J. Du, *Phys. Rev. X* **7**, 031011 (2017).
- [240] J. Zhang, P. Hess, A. Kyprianidis, P. Becker, A. Lee, J. Smith, G. Pagano, I.-D. Potirniche, A. C. Potter, A. Vishwanath, et al., *Nature* **543**, 217 (2017).
- [241] C. Deng, J.-L. Orgiazzi, F. Shen, S. Ashhab, and A. Lupascu, *Phys. Rev. Lett.* **115**, 133601 (2015).
- [242] N. Goldman, G. Juzeliūnas, P. Öhberg, and I. B. Spielman, *Reports on Progress in Physics* **77**, 126401 (2014).
- [243] T. Oka and S. Kitamura, *Annual Review of Condensed Matter Physics* **10**, 387 (2019).
- [244] R. Moessner and S. L. Sondhi, *Nature Physics* **13**, 424 (2017).
- [245] D. V. Else, C. Monroe, C. Nayak, and N. Y. Yao, arXiv:1905.13232 (2019).
- [246] T. Kitagawa, E. Berg, M. Rudner, and E. Demler, *Phys. Rev. B* **82**, 235114 (2010).
- [247] N. H. Lindner, G. Refael, and V. Galitski, *Nature Physics* **7**, 490 (2011).
- [248] J. Cayssol, B. Dóra, F. Simon, and R. Moessner, *physica status solidi (RRL)–Rapid Research Lett.* **7**, 101 (2013).
- [249] P. Titum, E. Berg, M. S. Rudner, G. Refael, and N. H. Lindner, *Phys. Rev. X* **6**, 021013 (2016).
- [250] M. C. Rechtsman, J. M. Zeuner, Y. Plotnik, Y. Lumer, D. Podolsky, F. Dreisow, S. Nolte, M. Segev, and A. Szameit, *Nature* **496**, 196 (2013).
- [251] P. Ponte, A. Chandran, Z. Papić, and D. A. Abanin, *Annals of Physics* **353**, 196 (2015).
- [252] D. A. Abanin, W. De Roeck, and F. Huveneers, *Annals of Physics* **372**, 1 (2016).
- [253] P. Ponte, Z. Papić, F. Huveneers, and D. A. Abanin, *Phys. Rev. Lett.* **114**, 140401 (2015).
- [254] V. Khemani, A. Lazarides, R. Moessner, and S. L. Sondhi, *Phys. Rev. Lett.* **116**, 250401 (2016).
- [255] D. V. Else, B. Bauer, and C. Nayak, *Phys. Rev. Lett.* **117**, 090402 (2016).
- [256] I.-D. Potirniche, A. C. Potter, M. Schleier-Smith, A. Vishwanath, and N. Y. Yao, *Phys. Rev. Lett.* **119**, 123601 (2017).
- [257] T. Mori, T. Kuwahara, and K. Saito, *Phys. Rev. Lett.* **116**, 120401 (2016).
- [258] D. V. Else, B. Bauer, and C. Nayak, *Phys. Rev. X* **7**, 011026 (2017).
- [259] F. Machado, G. D. Meyer, D. V. Else, C. Nayak, and N. Y. Yao, arXiv:1708.01620 (2017).
- [260] F. Machado, D. V. Else, G. D. Kahanamoku-Meyer, C. Nayak, and N. Y. Yao, arXiv:1908.07530 (2019).
- [261] C. W. von Keyserlingk, V. Khemani, and S. L. Sondhi, *Phys. Rev. B* **94**, 085112 (2016).
- [262] N. Y. Yao, A. C. Potter, I.-D. Potirniche, and A. Vishwanath, *Phys. Rev. Lett.* **118**, 030401 (2017).
- [263] S. Choi, J. Choi, R. Landig, G. Kucsko, H. Zhou, J. Isoya, F. Jelezko, S. Onoda, H. Sumiya, V. Khemani, et al., *Nature* **543**, 221 (2017).
- [264] J. Rovny, R. L. Blum, and S. E. Barrett, *Phys. Rev. Lett.* **120**, 180603 (2018).
- [265] T. Calarco, R. Fazio, and P. Mataloni, *Quantum Simulators*, vol. 198 (IOS Press, 2018).
- [266] U. Mahadev, in *2018 IEEE 59th Annual Symposium on Foundations of Computer Science (FOCS)* (IEEE, 2018), pp. 259–267.
- [267] J. Zhang, G. Pagano, P. W. Hess, A. Kyprianidis, P. Becker, H. Kaplan, A. V. Gorshkov, Z. X. Gong, and C. Monroe, *Nature* **551**, 601 (2017).
- [268] P. Jurcevic, H. Shen, P. Hauke, C. Maier, T. Brydges, C. Hempel, B. P. Lanyon, M. Heyl, R. Blatt, and C. F. Roos, *Phys. Rev. Lett.* **119**, 080501 (2017).
- [269] M. Heyl, *Reports on Progress in Physics* **81**, 054001 (2018).
- [270] P. Titum, J. T. Iosue, J. R. Garrison, A. V. Gorshkov, and Z.-X. Gong, *Phys. Rev. Lett.* **123**, 115701 (2019).
- [271] S. Ajisaka, F. Barra, and B. Žunkovič, *New Journal of Physics* **16**, 033028 (2014).
- [272] B. Žunkovič, M. Heyl, M. Knap, and A. Silva, *Phys. Rev. Lett.* **120**, 130601 (2018).
- [273] M. Heyl, *Phys. Rev. Lett.* **115**, 140602 (2015).
- [274] B. Žunkovič, A. Silva, and M. Fabrizio, *Phil. Trans. Royal Soc. A: Math., Phys. and Eng. Sci.* **374**, 20150160 (2016).
- [275] S. A. Weidinger, M. Heyl, A. Silva, and M. Knap, *Phys. Rev. B* **96**, 134313 (2017).
- [276] Y.-P. Huang, D. Banerjee, and M. Heyl, *Phys. Rev. Lett.* **122**, 250401 (2019).
- [277] M. Heyl, A. Polkovnikov, and S. Kehrein, *Phys. Rev. Lett.* **110**, 135704 (2013).
- [278] T. Graß and M. Lewenstein, *EPJ Quantum Technology* **1**, 8 (2014).
- [279] A. Kitaev, *Annals of Physics* **321**, 2 (2006).